Inaugural dissertation

for

obtaining the doctoral degree

of the

Combined Faculty of Mathematics,

Engineering and Natural Sciences

of the

Ruprecht - Karls - University

Heidelberg

Presented by

M.Sc. Anjun Zheng

born in: Henan, China

Oral examination: October 15th, 2024

Structural and bio-functional analysis revealed the mechanism of γ-tubulin ring complex formation in *C. albicans*

Referees: Prof. Dr. Elmar Schiebel

Dr. Stefan Pfeffer

Summary

Cytokinesis is an important biological process for cell proliferation. Microtubule (MT) as a member of the cytoskeleton is indispensable for cell migration, cell division, and cell polarity formation. Thus, investigating the MT nucleation mechanism, meaning the mechanism of how cells assemble MTs, is essential. γ-TuRC, consisting of two molecules of γ-tubulin, one Spc97, and one Spc98, has been recognized to be the MT nucleation template for both centrosomal MTOCs (microtubule organizing centers) and ncMTOCs (non-centrosomal MTOCs)[1]. Here, I mainly focus on the ncMTOC in *C. albicans* (known as SPB (the spindle pole body)) and try to understand this biological event.

In this study, I have successfully obtained two cryo-EM structures of the MT nucleation unit from *C. albicans* in collaboration with Dr. Stefan Pfeffer's group. This provided new insight into understanding the MT nucleation mechanism in *C. albicans*. The 3.6 Å γ-TuSC complex is a monomer and forms a Y-shaped structure (γ-tubulin-Spc97 one arm and γ-tubulin-Spc98 the other arm of the Y), which was resolved in collaboration with Dr. Erik Zupa. With the structural analysis and the mutation experiments, we found an insertion loop on Spc98 interacting with Spc97 stabilizing the γ-TuSC. In addition, the varied γ-tubulin positions in *C. albicans* and *Xenopus* implied the conformational changes required for the activation of the γ-tubulin ring complex in *C. albicans*[2, 3].

The other cryo-EM structure is the 3.6 Å γ-TuRC at the cytoplasmic side, which was obtained by co-expression of γ-TuSC with the γ-TuRC receptor Spc72 and the microtubule polymerase Stu2. This project part was done in collaboration with Bram Vermeulen (PhD student from Dr. Stefan Pfeffer's group). From this study, we surprisingly found that the $Spc72^{CM1}$ was bound to Spc97 in a dimeric way and the dimerised CM1 (a short motif of the N-terminus of Spc72) was essential for the oligomerisation of γ-TuSC and cell viability. Except for this, I also found the N-terminal region of the CM1 motif interacting with the neighboring Spc98, which is also important for promoting the oligomerisation of the γ-TuSC. In addition, we have successfully confirmed the C-terminal region of $Spc72^{291-599}$ was essential for the interaction with the C-terminal helix of $Stu2^{894-924}$. Based on the monomeric and oligomeric structures of γ-TuSC, I confirmed the crucial

role that the dimeric CM1 motif plays in the γ-TuSC oligomer formation. Moreover, the direct binding between Spc72 and Stu2 in *C. albicans* also provided more evidence of Spc72 recruiting Stu2 and its bound α/β-tubulin dimers to γ-TuRC at the cytoplasmic side. In the future, how Stu2 binds to the γ-TuRC on the structural level needs to be worked out to better understand the function of Stu2 in the MT nucleation process together with γ-TuRC, and the MT nucleation mechanism at the nuclear side of the SPB is as important to be investigated.

Zusammenfassung

Die Zytokinese ist ein wichtiger biologischer Prozess für die Zellproliferation. Die Mikrotubuli (MT) als Zytoskelettmitglied ist für die Zellmigration, Zellteilung und Zellpolaritätsbildung unverzichtbar. Daher ist die Untersuchung des MT-Nukleationsmechanismus unerlässlich. γ-TuRC ist sowohl für centrosomalen MTOCs (centrosomalen Microtubule Organizing Centers) als auch bei ncMTOCs (non-centrosomalen Microtubule Organizing Centers) die MT-Nukleationsvorlage in Zellen. In dieser Arbeit konzentriere ich mich hauptsächlich auf das ncMTOC-System in *C. albicans* (SPB (Spindelpolkörper)) und versuchen diesen biologischen Mechanismus zu verstehen.

In dieser Studie ist es mir gelungen, in Zusammenarbeit mit der Gruppe von Dr. Stefan Pfeffer, zwei Kryo-EM-Strukturen der MT-Kernbildungseinheit in *C. albicans* zu erhalten, die neue Einblicke in das Verständnis der MT-Ausbildung in *C. albicans* lieferten. Der 3.6 Å γ-TuSC-Komplex ist ein Monomer und bildet eine Y-förmige Struktur aus, die in Zusammenarbeit mit Dr. Erik Zupa aufgeklärt wurde. Mit der Strukturanalyse und den Mutationsexperimenten fand ich eine Insertionsschleife in Spc98, die mit Spc97 interagiert und den γ-TuSC stabilisiert. Darüber hinaus implizierten die Untersuchungen unterschiedlichen γ-Tubulin-Positionen in *C. albicans* und *Xenopus* die für die Aktivierung des γ-Tubulin-Ringkomplexes in *C. albicans* erforderlich sind[2, 3].

Die andere Kryo-EM-Struktur ist der 3.6 Å γ-TuRC auf der zytoplasmatischen Seite des SPBs, der durch die Co-expression von γ-TuSC mit Spc72 und Stu2 erhalten wurde. Dieser Teil wurde in Zusammenarbeit mit Bram Vermeulen (Doktorand aus der Gruppe von Dr. Stefan Pfeffer) durchgeführt. Mit Hilfe dieser Studie fanden wir überraschenderweise heraus, dass das $Spc72^{CM1}$ als Dimer an Spc97 bindet und die dimerisierten CM1-Motive für die Oligomerisierung von γ-TuSC und die Zellviabilität entscheidend waren. Darüber hinaus fand ich auch die N-terminale Region des CM1-Motivs, die mit dem benachbarten Spc98 interagiert, was ebenfalls wichtig für die Förderung der Oligomerisierung von γ-TuSC ist. Darüber hinaus habe ich erfolgreich bestätigt, dass die C-terminale Region von $Spc72^{291-599}$ für die Interaktion mit der C-

terminalen Helix von Stu2$^{894-924}$ essentiell ist. Basierend auf den monomeren und oligomeren Strukturen von γ-TuSC bestätigten wir die entscheidende Rolle dimerer CM1-Motive bei der γ-TuSC-Oligomerisierung. Darüber hinaus lieferte die direkte Bindung zwischen Spc72 und Stu2 in *C. albicans* auch weitere Hinweise darauf, dass Stu2 über seine gebundenen α/β-Tubulin-Dimere auf der zytoplasmatischen Seite die Mikrotubulinukleationsaktivität von an γ-TuRC stimuliert. In Zukunft muss untersucht werden, wie Stu2 auf struktureller Ebene an das γ-TuRC bindet, um die Funktion von Stu2 im MT-Ausbildungsprozess zusammen mit γ-TuRC besser zu verstehen. Der MT-Ausbildungsmechanismus auf der Kernseite ist ebenso wichtig zu untersuchen.

Table of Contents

Abbreviations

MT/MTs: Microtubule/Microtubules

MTOCs: Microtubule organizing centers

ncMTOCs: Non-centrosomal MTOCs

SPB: Spindle pole body, microtubule nucleation center in yeast

AMR: Actomyosin-based contractile ring

GTPase: A family of Rho-like GTPases with inactive (GDP-bound) and active (GTP-bound) states

Midzone: Antiparallel non-kinetochore interdigitating microtubules

PRC1: A cytokinesis regulator protein 1, which crosslinks antiparallel microtubules at the spindle midzone (the central spindles)

SPD-1: Microtubule-bundling protein in *C. elegans*

C. elegans: *Caenorhabditis elegans*

CDK: Cyclin-dependent kinase

APC/C: Anaphase-promoting complex/cyclosome

MKLP1: A kinesin-like protein

CYK4: The Rho family GTPase-activating protein (GAP)

Plk1: Polo-like kinase 4

GEFs: Rho GTPase GDP/GTP exchange factors

Myo1: Myosin protein 1

S. cerevisiae: *Saccharomyces cerevisiae*

Bni5: A septin-binding protein before cytokinesis

IQGAP Iqg1: The conserved actin regulating proteins contain multiple domains including an N-terminal calponin homology domain (CHD), IQ motifs, and a C-terminal GTPase-activating-protein (GAP)-related domain (GRD). Iqg1 is the IQGAP homologue in yeast

GEFs: Rho GTPase GDP/GTP exchange factors

RhoGEF Tus1: a member of Rho GTPase GDP/GTP exchange factors

Cdc5: a polo kinase ortholog

CAR: Contractile actin ring

Bni1/Bnr1: Homologues of Formins in budding yeast

Formins: A highly conserved family of proteins necessary for actin filament assembly characterized by the FH2 domain

Cdc42: A Rho GTPase, a regulator of cell polarity in various cell types

α/β-tubulins: α-tubulin and β-tubulin heterodimers

PF: Protofilament

E-hook: Acidic carboxy-terminal region of tubulin

MTBPs: Microtubule-binding proteins

CSPP1: The centrosome/spindle pole associated protein 1

MAP2/Tau family: Microtubule-associated proteins which include the proteins of MAP2, MAP4, and Tau and homologs in other animals

MAPs: Microtubule-associated proteins

Tau: Microtubule-associated protein encoded by gene on chromosome 17q21

XMAP215: *Xenopus* microtubule-associated protein 215

Stu2: Suppressor of tubulin 2

TOG: Tumor overexpressed gene

CLASP: CLIP-associating protein

γ-TuSC: γ-Tubulin small complex

γ-TuRC: γ-Tubulin ring complex

-TIPs: Minus-end-targeting proteins

CAMSAPs: Calmodulin-regulated spectrin-associated proteins

PCM: Pericentriolar material

DAs: Distal appendages

SDAs: Subdistal appendages

aMTOC: Acentrosomal microtubule nucleation center

RanGTP: GTP-bound, Ras-related nuclear protein

CPC: Chromosomal passenger complex

K-fiber: Kinetochore fiber

AKAP450: The A-kinase anchor protein 450

GM130: The *cis*-Golgi matrix component

CDK5RAP2: Cyclin-dependent kinase 5 regulatory associated protein 2

aPKC: Atypical Protein Kinase C

PAR3 and PAR6: PDZ domain-containing proteins

Nesprin 1: Isoform of nuclear envelope protein

AKAP6: A component of the nuclear envelope MTOC

RCC1: Regulator of chromosome condensation 1

Aur. B: Aurora B

KMN complex: KNL1, Mis12, and Ndc80 complex

MCAK: Mitotic centromere-associated kinesin (KIF2C)

OP18: Oncoprotein 18 (stathmin 1, STMN1)

Ran: Ras-related nuclear protein

RanGDP/GTP: Complex of Ran with GDP/GTP

Ska complex: Spindle and kinetochore-associated complex

TPX2: Targeting protein for Xklp2

S. pombe: *Schizosaccharomyces pombe*

Cnm67: Chaotic nuclear migration protein 67

Nud1: Mitotic exit network (MEN) scaffold protein

Sid4: Septation initiation protein sid4

Cdc11: Cell division control protein 11

Cmd1: Calmodulin 1

Spc42: Spindle pole body component 42

Spc29: Spindle pole body component 29

Cam1: Calcium and Membrane-binding protein

Sfi1: SFI1 centrin binding protein

Kar1: Karyogamy protein 9

Cdc31: Cell division control protein 31

Spc110: Spindle pole body component 110

Spc72: Spindle pole body component 72

cMTs: Cytoplasmic MTs

nMTs: Nuclear MTs

TUB4: yeast γ-tubulin

A. nidulans: *Aspergillus nidulans*

NEED1: GCP-WD protein, Neural precursor cell expressed developmentally down-regulated protein 1

NME7: Nucleotide diphosphate kinase 7

MOZART1/2: Mitotic Spindle Organizing Protein 1/2

X. laevis: *Xenopus laevis*

CM1: Centrosomin motif 1

C. albicans: *Candida albicans*

GRIP: Gamma Ring Protein

XL-MS: Crosslinking mass spectrometry

Caγ-TuSC: *C. albicans* γ-TuSC

CaSpc97/CaSpc98/CaTub4: *C. albicans* Spc97/Spc98/Tub4

CaMzt1: *C. albicans* Mzt1

MST: Microscale thermophoresis

CaSpc110/CaSpc72: *C. albicans* Spc110/Spc72

ch-TOG: Colonic-hepatic tumor-overexpressed gene

TACC: Transforming acidic coiled-coil protein

Cryo-EM: Single-particle electron cryo-microscopy

AF2: AlphaFold 2

PDB: Protein Data Bank

EMDB: Electron Microscopy Data Bank

CTF: Contrast transfer function

1 Introduction

1.1 Cytokinesis in metazoa and fungi

1.1.1 Cytokinesis in metazoa

Cytokinesis, cell division, is a significant biological process with a large-scale rearrangement of the plasma membrane and needs to be coordinated with nuclear division. The process of cytokinesis is quite complicated and numerous proteins and cell signaling pathways are involved to ensure cells are separated at the right size and with an equal number of chromosomes. In metazoa and fungi, the AMR (actomyosin-based contractile ring) is the main driving force for cytokinesis, and MTs direct the right division plane (the equator) positioning and lead to normal abscission[4].

Cytokinesis is regulated by the cell cycle machinery and cytokinesis is an anaphase event in metazoan cells, which is activated during the metaphase-to-anaphase transition[4]. The cytokinetic cells are distinguishable from other cells with the feature of a cleavage furrow formation and the cell shape transition (Fig. 1a). The activated small GTPase RhoA in animal cells directly participates in the division plane or equator assembly during cytokinesis which is in favor of myosin activation and actin polymerization and these processes are the prerequisites for the contractile ring formation[4]. The midzone (antiparallel non-kinetochore interdigitating microtubules) between the separating chromosomes is important for maintaining the spindle structure, elongation, and positioning of the cleavage furrow during the metaphase-to-anaphase transition (Fig. 1a)[5, 6].

PRC1 is a CDK substrate and can form oligomers to bind MTs and promote the bundling of MTs. Inhibition of PRC1 ortholog SPD-1 in *C. elegans* (*Caenorhabditis elegans*) can prevent the midzone formation and cause two disarrayed half spindles[7-9]. PRC1 is also an indispensable regulator in midzone formation in human cells with its dephosphorylated form to create the bundling antiparallel, non-kinetochore, and interdigitating MTs[10]. The inactivation of cyclin B and Cdk1 triggered by the activation of the APC/C (anaphase-promoting complex/cyclosome) can activate the cytokinetic regulators such as centralspindlin (comprised of two proteins, a kinesin-like protein, MKLP1, and a Rho GTPase activating protein, CYK-4), which is a hetero-tetramer oligomerized by Aurora B

kinase and is assembled from CYK4 (the Rho family GTPase-activating protein) and MKLP1 (a kinesin-like protein)[11, 12]. CYK4 as the subunit of centralspindlin will be phosphorylated by Plk1 and then the phospho-CYK4 can bind to the GEF (Rho GDP-GTP exchange factor) Ect2, which activates RhoA GTPase. Activated RhoA promotes the formation of the contractile ring (Fig. 1b)[13, 14].

1.1.2 Cytokinesis in fungi

In contrast to the commencement of cytokinesis until the metaphase-to-anaphase in metazoan cells, the division plane positioning starts immediately after the last division in yeasts. The AMR consists of actin filaments and myosin II, which as mentioned above, is the main force for cytokinesis. Myo1 is a 2-headed myosin II protein in *S. cerevisiae* (*Saccharomyces cerevisiae*) and its localization to the division site is dependent on Bni5, a septin-binding protein, before cytokinesis, and its localization to the division site is then dependent on IQGAP Iqg1 during cytokinesis[15]. Cdc5, a polo kinase ortholog, phosphorylates Rho 1 GEFs and activates Rho 1 in anaphase, and promotes the assembly of contractile actin ring (CAR or AMR). The failure of Rho 1 activation leads to the mislocalization of formin Bni1 and results in CAR assembly failure and cytokinesis defect because actin filaments are assembled by Fromins[16, 17].

The bud neck in budding yeast fulfills the same function as the cleavage furrow in metazoa. Both of them require the activation of Rho-family GTPases and Cdc42 in budding yeast. In the G1 phase, Cdc42 localizes at a cortical site to promote the formation of a septin ring at the bud neck site, and then septin filaments further make a template for the assembly of AMR as mentioned above (Fig. 1c)[18].

1.1.3 Cytokinesis and microtubules

Cell cytokinesis as mentioned above is a complicated biological process. Before and during cytokinesis, cells need to go through cell shape changes, nuclear separation (yeast), and chromosome separation, meaning depending only on the AMR (mammalian cells) and CAR (yeast cells), cells cannot separate normally. The successful cell abscission also relies on the formation of the midzone featured with an array of bundled microtubules during anaphase and to facilitate the division-plane positioning.

Centralspindlin complex as a main microtubule regulator can promote the central microtubule bundling at the beginning of early anaphase and these bundles will be compacted and develop into the cell midbody in the end. Another prominent protein in midzone formation is the nonmotor microtubule-associated protein PRC1[7, 8] (Ase1 in yeast[19]), which can bind and facilitate antiparallel microtubule bundling[20, 21]. Thus, the understanding of how microtubules assemble, polymerize, and then dominate the abscission process from the cellular and molecular level has no doubt been an important aspect of understanding the mechanism of cytokinesis.

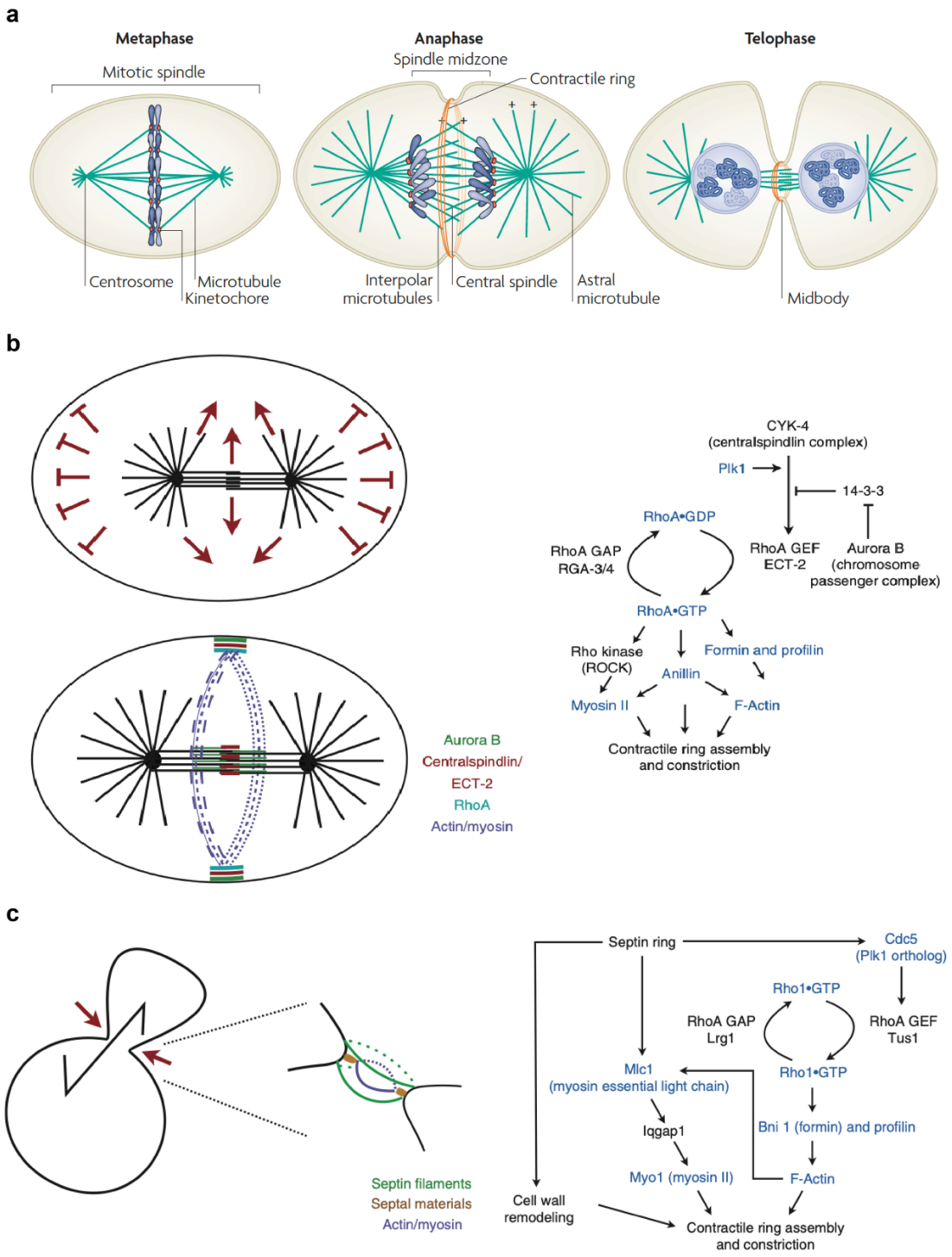

Figure 1: Cytokinesis in metazoa and fungi

(a) Cartoon diagrams of cell division from metaphase to telophase. The components and structure changes involved in cytokinesis are marked: centrosome, spindle midzone, contractile ring, interpolar microtubules, central spindle, astral microtubule, and midbody. The panel is from Glotzer 2009[11].

(b) The mechanism of how division plane and cleavage furrow form in metazoan cells. The physical force produced by the spindle, and central/astral microtubules guides the furrow position. The contractile ring components and the assembly are depicted. The panel is from Glotzer 2017[4].
(c) The mechanism of how the division plane forms in budding yeast. The septin filaments, actin, myosin, and the contractile ring assembly pathway are depicted. The panel is from Glotzer 2017[4].

1.2 Microtubule

1.2.1 Microtubule structure

Microtubules are polymers composed of heterodimers of α/β-tubulins (α- and β-tubulins) which assemble into a hollow and cylindrical structure with a diameter of approximately 25 nm and a length that varies from <1 μm to >100 μm. It contains two polarized ends of a more stable minus-end and a less stable plus-end (Fig. 2a)[22]. Microtubules are normally composed of 13-juxtaposed PFs (protofilaments) oriented parallel to the tube axis[23]. However, 14 and 15 PF microtubules were also found in biological specimens but are skewed, in addition, 12 to 16 protofilaments were also observed both in cellular material and in MTs assembled *in vitro*[24, 25]. A co-existence of a variety number of protofilaments in the cell provides a postulation for the cells' tolerance to the deformed and curved-bending structure of MTs without breaking *in vivo*[26]. MTs with 13-PFs are the dominant type in cells. The rotation feature of 13-PF MTs has been recognized as two types: B lattice in which an α-tubulin is next to another α-tubulin (α–α) and β-tubulin next to β-tubulin (β–β). This lattice structure adopts an 'A lattice' mode at the seam where an α-tubulin is next to another β-tubulin (α–β) and results in an offset of 1.5 dimers. However, in 12 PFs or 15 PFs, even at the seam, they still form into a 'B lattice' structure (Fig. 2b)[22]. How the different lattice structures at the seam influence the stability of the entire MT is still uncertain, however, the longitudinal interactions between subunits of α/β-tubulins seem to exert more extensive impact in different PF types compared to the lateral binding of the subunits (Fig. 2c)[22, 27].
The other aspect of the MT structure is the MT surface charge. MTs are long, regular, overlapped, dynamic, and large oligomers composed of α/β-tubulin heterodimers, and the

E-hooks (carboxy-terminal region) of these heterodimers are composed of glutamate-rich amino acids, which contribute to the negatively charged MT surfaces. Importantly, it is also because of this feature, that many MTBPs (microtubule-binding proteins) can use their positively charged domains to bind to MTs[28]. Interestingly, microtubule holes on the wall were found and function as channels connecting the inner lumen and outside of MTs, which has been found to allow diffusion of water and some smaller molecules[29]. α-tubulin K40 acetylation modification is an example to explain the bio-function of MT holes: K40 amino acid extrudes from the lumen to the outside through MT holes to be acetylated at the cytoplasmic side[30]. The lumen of MTs is not a completely hollow space: some unrecognized densities were visualized by cryo-ET and cryoelectronic microscopy[31]. The protein CSPP1 as an MT stabilizer was recently found to be localized in the MT lumen (Fig. 2d) and has a high binding efficiency to the severed or damaged MTs to prevent MT depolymerization and facilitate repair[32].

1.2.2 Microtubule dynamics

The rigidity of MTs is important for maintaining the normal cell shape and their straightness makes the long-distance transport of cargo-carrying motor proteins more efficient. Moreover, the rigid cytoskeletal structure of MTs with the attached actin and myosin helps to create the force during cell motility[33].

MTs as mentioned above are assembled by α/β-tubulins and both α/β-tubulins can bind GTP, whereas only the β-tubulin can hydrolyze GTP during the MT polymerization[34-36]. The growth of MTs is dependent on GTP-capped β-tubulins at the plus-end side, and the hydrolyzed, GDP capped β-tubulins are more prone to catastrophe from MTs, thus, MTs are always keeping dynamic with different states of ‘grow’, ‘catastrophe’, and ‘rescue’, which is termed as ‘dynamic instability’ (Fig. 2e)[33, 37]. With such feature of MTs, cells can flexibly transform into new shapes during the mitotic phase and force the separation of chromosomes[38].

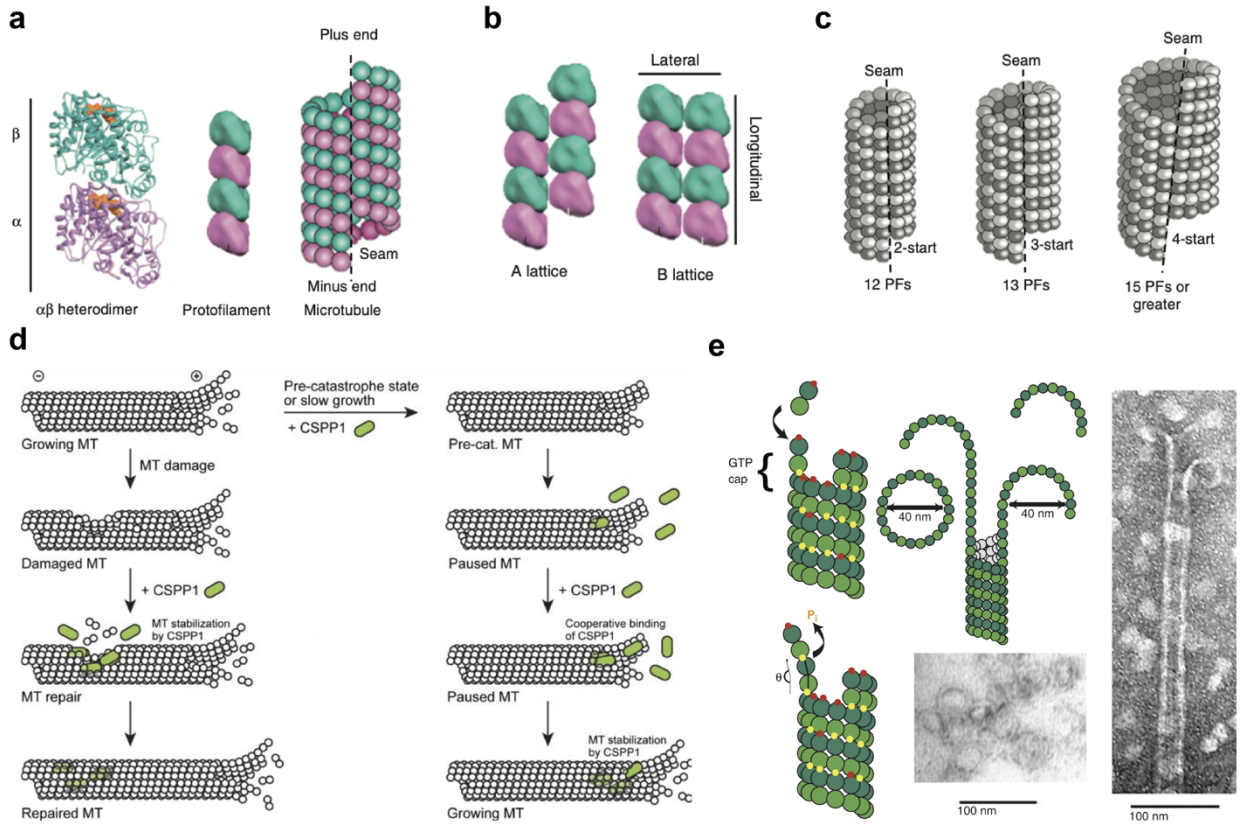

Figure 2: Microtubule structure

(a) The microtubule is composed of α/β-tubulins. The panel is from V. Goodson and M. Jonasson 2018[22].

(b) The two types of lattice structures are based on the lateral interaction of α and β-tubulins. The panel is taken from V. Goodson and M. Jonasson 2018[22].

(c) The relations between the protofilament number and the structure. The panel is taken from V. Goodson and M. Jonasson 2018[22].

(d) Model for microtubule lumen protein of CSPP1 and its proposed function. The panel is taken from C. M. van den Berg *et al*., 2023[32].

(e) Microtubule GTP cap and the structure of dynamic of plus-end. The panel is taken from T. Hawkins *et al*., 2010[33].

1.2.3 Microtubule-associated proteins

The complexity of the 'dynamic stability' of MTs is supported by several different types of MTBPs which are classified into mainly 4 groups: MT *stabilizers*, *destabilizers*, *capping*

proteins, and *bundlers/cross-linkers* (Fig. 3a). MT stabilizers can promote polymerization or delay depolymerization with unambiguously distinguished features or functional activities because they both lead to the growth of MTs[22].

MAP2/Tau family (MAPs, microtubule-associated protein) contains MAP2, MAP4, and Tau homologs in animal species with conserved MT-binding repeats at the carboxy-terminal region. Among these three proteins, MAP2/Tau are present in neurons and MAP4 is found in other tissues but not in neurons. MAP2 was proposed to be involved in neuro-morphogenic processes of neurite initiation, whereas Tau has been known to be related to Alzheimer's disease. In conclusion, these proteins are known for stabilizing MTs[39].

The other stabilizer family is the XMAP215/Dis1/Stu2/CLASP family, which exists in a broad range of organisms with the conserved TOG (tumor overexpressed gene) domains to recruit soluble α/β-tubulin dimers (not the incorporated α/β-tubulins in MTs) to the MT plus end to exert MT polymerization (XMAP215/Dis1/Stu2) or to MT lattices to prevent MT catastrophes and to promote MT rescues (CLASP)[40-43] (see Fig. 3b).

The scheme structure analysis of TOG family proteins shows that vertebrate XMAP215/Dis1 and CLASP proteins contain more TOG domains compared to the yeast homologs and the reason behind this is that in vertebrates, TOG proteins are monomers and in yeast, they can assemble into homodimers (Fig. 3c)[40, 41]. XMAP215/Stu2 as MT plus-end polymerases bind GTP-bound α/β-tubulins with high affinity and recruit them to the curved, tapered GTP-tubulin capped plus end and to promote the growth of MTs, however, GTP-tubulins were hydrolyzed into GDP-subunits alongside the MT body and once the GTP-bound β-tubulins at the plus end were hydrolyzed, MTs will depolymerize[44]. In addition, the structure of Stu2 TOG1 bound to α/β-tubulins was obtained, which showed the preferential binding of the 'curved' conformation of αβ-tubulin for the TOG1 domain. However, TOG2 was supposed to recognize the straighter α/β-tubulin conformation at the MT body together with the C-terminal basic domain of *S. cerevisiae* Stu2. This together provides a mechanism of how the 'curved' αβ-tubulins from TOG1 are delivered to the MT plus-end[45]. Farmer et al. have studied the polymerase of XMAP215 by using GFP-tagged EB1 as a GTP-cap maker and the addition of XMAP215 to tubulins purified from the bovine brain resulted in a faster growth rate and the instantaneous catastrophe rate

at the plus-end comet[46]. Whether EB1 and XMAP215 function at the plus end of MTs in a synergistic way or conversely is debatable and how these two or even more MAPs function at the plus end of MTs *in vivo* is still an enigma.

Opposite to MT stabilizers, destabilizers are MT depolymerizers and promote the disassembly of the dynamic MTs and transform them into free α/β-tubulins. Sequestering proteins such as stathmin protein in animals can bind two dimers at once in a curved conformation thus preventing the incorporation into MTs[47]. MT severing proteins such as AAA ATPases, katanin, and spastin can cut MTs into pieces directly and quickly due to the direct interaction with MTs[48]. Tip destabilizers such as kinesins can also directly work on unstable MT tips. They use ATP hydrolysis to remove tubulin subunits and trigger MT depolymerization[49].

MT capping proteins refer to proteins capped at the minus or plus end of MT. The well-studied minus-end capping proteins are the γ-Tubulin small complex (γ-TuSC) in fungi and the γ-Tubulin ring complex (γ-TuRC) in higher eukaryotes, which have also been recognized as the nucleators for MTs[50-52]. CAMSAP/Patroin/Nezha family is classified as '-TIPs' (minus-end-targeting proteins) and was found to be located at MT minus ends across different species such as human and Drosophila (insects, vertebrates, ?)[53-55]. CAMSAPs (calmodulin-regulated spectrin-associated proteins) contain three homologs of CAMSAP1, CAMSAP2 (KIAA1078/CAMSAP1L1), and CAMSAP3 (KIAA1543/Nezha) in mammalian cells with CAMSAP1 transiently interacts with and then tracks the growing minus end, whereas CAMSAP2/3 can stably bind to the MT lattice (Fig. 3d)[56, 57]. In mammals, CAMSAP2 and CAMSAP3 strongly suppress minus-end growth without affecting plus-end growth whereas CAMSAP1 has a minor impact on the polymerization rate of the minus-end growth[57]. Thus, these three types of CAMSAP proteins regulate minus-end dynamics in different ways. Concerning the different interacting modes with MT minus ends of CAMSAPs and γ-TuRC complex, the γ-TuRC complex is more stably localized at the minus end of MTs due to its function as an MT nucleator. γ-TuRC complex can promote MT nucleation at MTOCs and ncMTOCs[58], however, CAMSAPs are more involved in ncMTOC microtubules such as the Golgi-associated MTs. They impact cell migration by influencing the MT density in the cytoplasm. In addition, in neurons and

epithelial cells, CAMSAPs and γ-TuRC were found to sequentially nucleate and stabilize MTs and the mechanism behind such phenomena needs to be further confirmed[59, 60].

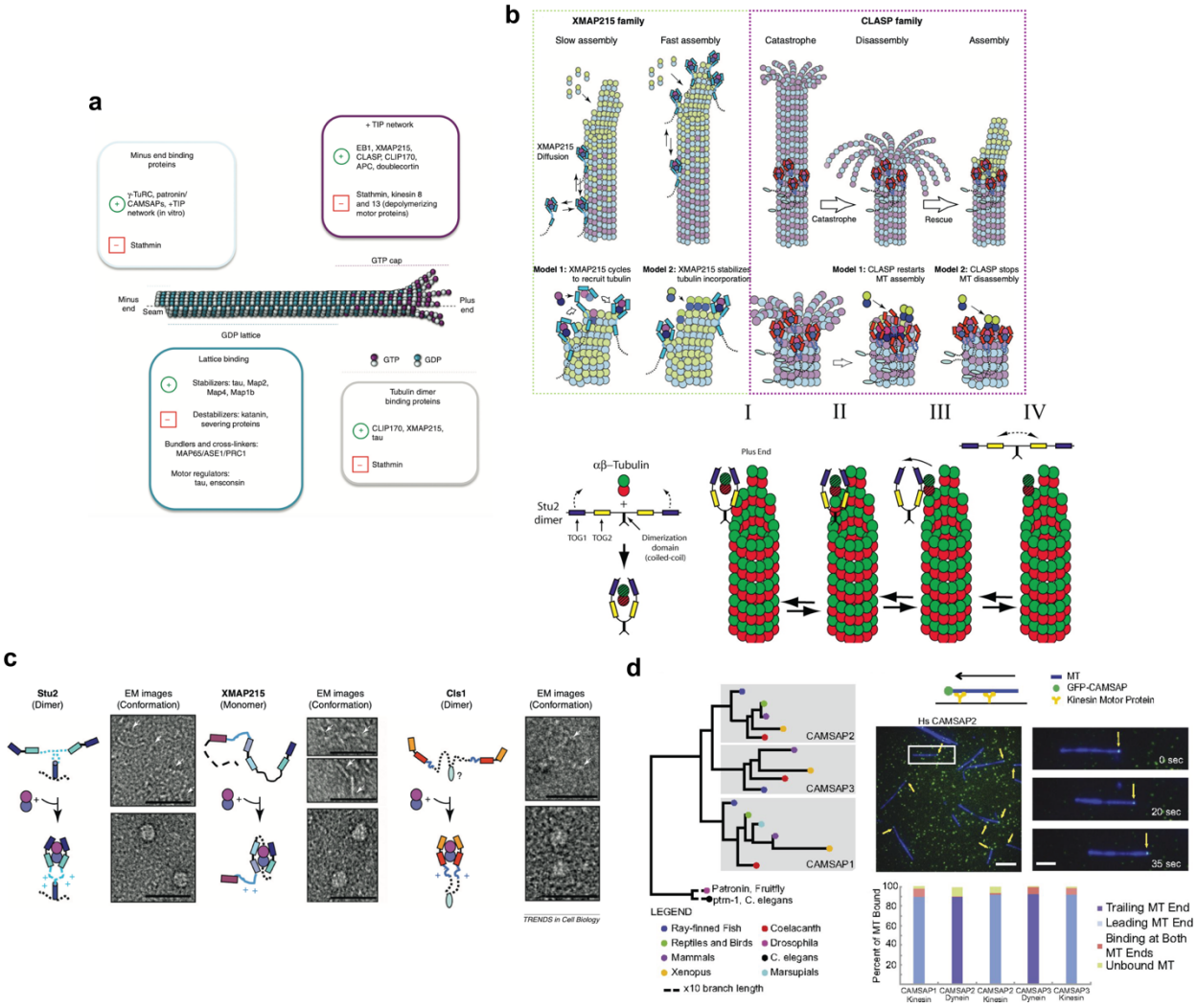

Figure 3: Microtubule-associated proteins

(a) Microtubule-binding proteins. The major microtubule-binding proteins were specified according to their localization and functions. The green plus symbol (+) represents positive regulation and the red minus symbol (-) represents negative regulation. The panel is from V. Goodson and M. Jonasson, 2018[22].

(b) Model for XMAP215, CLASP and Stu2 mechanisms. XMAP215 and Stu2 recruit α/β-tubulins to the plus end or along the microtubule (XMAP215), whereas CLASP restarts the MT assembly or stops the MT disassembly. The panel is from Jawdat Al-Bassam and Fred Chang, 2011[43].

(c) Stu2 functions as a dimer. Compared with the monomeric XMAP215, Stu2 functions as a dimer. The panel is from Jawdat Al-Bassam *et al*., 2006[40].
(d) CAMSAPs have a conserved function of binding MT minus-ends across different species. The panel is from Melissa C. Hendershott and Ronald D. Vale, 2014[57].

1.3 Microtubule nucleation

1.3.1 Microtubule nucleation from the centrosome

Centrosomes since their discovery by Flemming and named by Bovery in the 19th century[61] are known to be involved in cell locomotion, development, and cell division[62]. Following up with the disassembly of astral microtubules in interphase, centrosomes in turn function as MTOCs for bipolar spindles in mitosis. As such they transform from the astral microtubule organizing center in interphase to the bipolar spindle organizing center in mitosis. Centrosomes are important during cytokinesis[63-66].

Centrosome as a non-membranous organelle exists in the somatic cell as a pair and has self-replication capability[67]. One Centrosome is composed of two centrioles and the centriole unit is a cylindrical organelle with a length of ~500 nm and a diameter of 250 nm in vertebrate cells and the centriole itself is a nine-fold copy of triplets of microtubules (Fig. 4a)[68-70]. The two centrioles are connected by a proteinaceous centrosome linker and only one centriole (the centrosome that was formed in the previous cell cycle) is mature (mother centriole) while the other one is named of daughter centriole; during G1 phase, the newborn centriole is starting to be elongated from PCM (pericentriolar material), and PCM is localized at the proximal end of the centriole[70, 71]. During the G2 phase, the daughter centriole becomes a mother centriole which is characterized by the gain of accessory structures of DAs (distal appendages) and SDAs (subdistal appendages)[70], and the cartoon structure of the centrosome is shown in Fig. 4a.

Centrosomes as an MTOC in animal cells determine the mitotic spindle orientation and genome stability[72, 73]. As shown in Fig. 4a, the MTs formed from centrosomes are indeed nucleated from the γ-TuRC bound to the PCM[74, 75, 70].

1.3.2 Acentrosomal MT nucleation in higher eukaryotes

It has been discovered that bipolar spindles can form in the absence of centrosomes in plant cells and vertebrate oocytes. Moreover, acentrosomal MTs can also be found in higher vertebrate somatic cells[63]. Conclusively, here are several different acentrosomal MT formation pathways in mitosis: **(a)** the RanGTP-dependent MT nucleation around the chromosomes; **(b)** CPC-dependent MT stabilization around kinetochores; **(c)** the Augmin-dependent branching-MT amplification on pre-existing MTs, and **(d)** the formation of K-fibers (Fig. 4b).

With the development of light and electron microscopy and protein expression manipulating methods in recent years, insights into the non-centrosomal microtubule networks have been received. For cells that can change their shape or migrate, Golgi membrane-dependent or endosome-dependent MTOCs are the centers for emanating the polarized and dynamic microtubules and are important for cell migration during development. The Golgi organelle is the main MTOC in the differentiated cells and is involved in cell polarization, dynein-driven self-assembly of the Golgi ribbon, and secretory trafficking[76]. AKAP450 as a scaffolding protein binds GM130 (the *cis*-Golgi matrix component) to recruit γ-TuRC through CDK5RAP2 and myomegalin, which is a central player in microtubule nucleation at the Golgi[77]. The endosome MTOC was found in fly neurons, where γ-TuRC is localized to Rab5-positive endosomes [78]. The cortex MTs in polarized epithelial cells featured minus ends localized at the apical cortex or cell-cell junctions and the plus ends faced towards the basal side, the organization of the apical MTs is regulated mainly by aPKC (atypical Protein Kinase C), PAR3, and PAR6 (PDZ domain-containing proteins)[77, 79-81]. The nuclear envelope can also function as MTOC in skeletal muscle cells and osteoclasts. Nesprin 1 (an isoform of nuclear envelope protein) together with AKAP6 (a spectrin repeat-containing adaptor protein) recruit AKAP450 and pericentrin and then the Golgi γ-TuRC can be recruited at the nuclear envelope[82, 83]. Except for the different types of MTOCs mentioned above, mitochondria in *D. melanogaster* spermatids can also function as MTOCs with the feature of γ-TuRC bound to mitochondria via the recruitment of centrosomin (the orthologue of CDK5RAP2)[84]. MTs formed from mitochondria support the elongation of sperm cells[77, 84]. The main different MTOCs are shown in Fig. 4c.

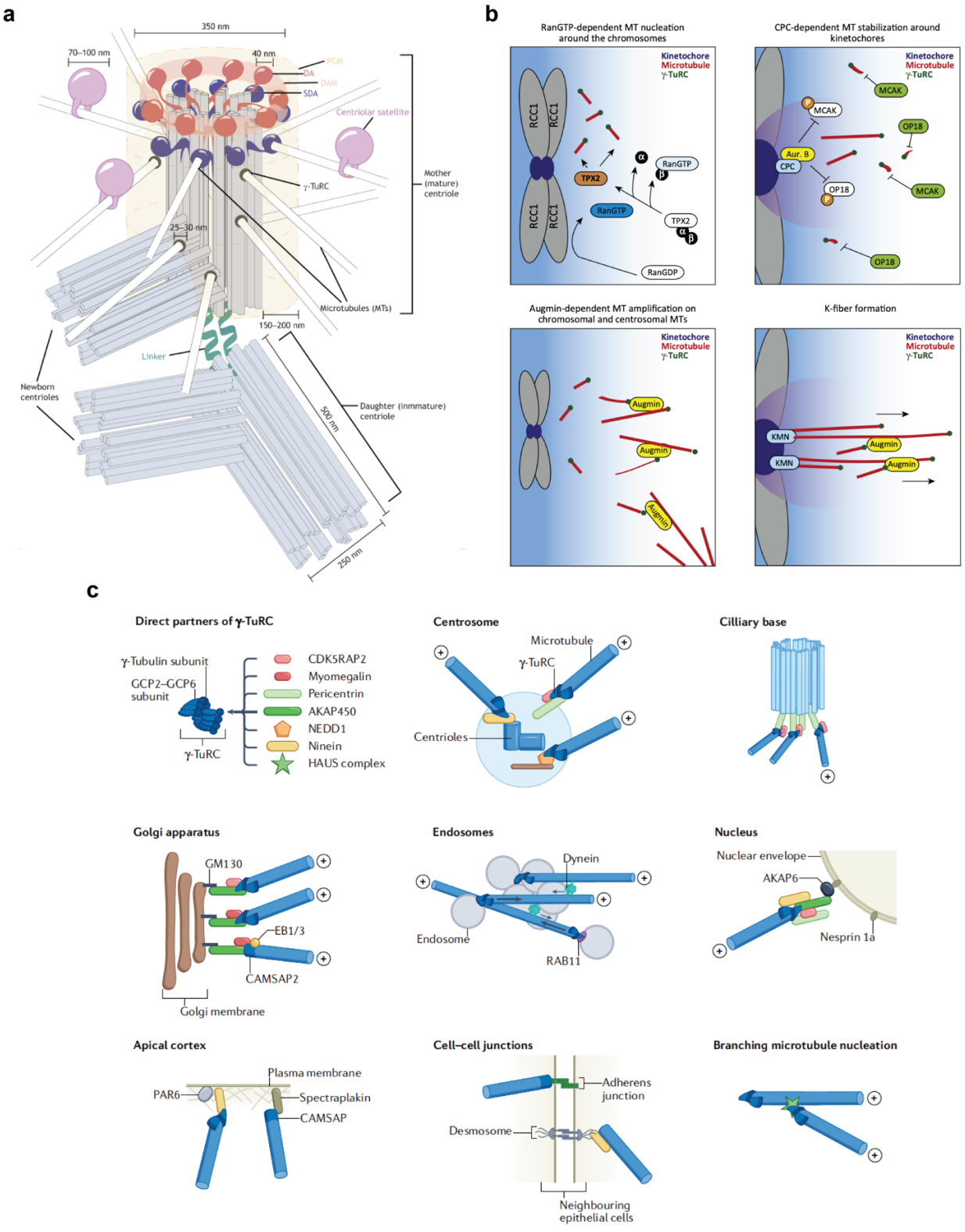

Figure 4: Microtubule nucleation in higher eukaryotes

(a) The reconstructed structure of the mature centrosome in G2 phase cells. Different components such as centriole triplets from mother and daughter centrioles, SDA, DA, DAM, PCM, centrosome linker, centriolar satellite, microtubule, and γ-TuRC are depicted. The panel is taken from Jose Blanco-Ameijeiras et al., 2022[70].
(b) Model of acentrosomal MT formation. Four different pathways are shown. Abbreviations: **RCC1**, regulator of chromosome condensation 1; **Aur. B**, aurora B; **KMN complex**, KNL1, Mis12, and Ndc80 complex; **MCAK**, mitotic centromere-associated kinesin (KIF2C); **OP18**, oncoprotein 18 (stathmin 1, STMN1); **P**, phosphorylation; **Ran**: Ras-related nuclear protein; **RanGDP/GTP**, complex of Ran with GDP/GTP; **Ska complex**, spindle and kinetochore-associated complex; **TPX2**, targeting protein for Xklp2. The panel is taken from Sylvain Meunier and Isabelle Vernos, 2016[63].
(c) MTOCs found in differentiated animal cells. Microtubules originated from centrosomes, Golgi apparatus, endosomes, nucleus, apical cortex, the neighboring epithelial cells, and the microtubules were depicted. The panel is taken from Anna Akhmanova and Lukas C. Kapitein, 2022[77].

1.3.3 Acentrosomal MT nucleation in yeast

S. cerevisiae and *S. pombe* (*Schizosaccharomyces pombe)* as two representative fungi species have been studied extensively in the aspect of cell mitosis. Unlike most mammalian cells containing centrosomes in vertebrates, yeast cells are devoid of centrosomes while the multi-layered SPB functions as a MTOC. The SPB is a nuclear membrane-embedded structure that contains inner and outer plaques facing toward the nuclear and cytoplasmic sides, respectively. In between the inner and outer plaques is the central plaque which is embedded in the nuclear membrane and another structure named the ‘Half-bridge’ is attached to the cytoplasmic side of the SPB and is important for SPB duplication (Fig. 5a)[85].
The components of SPB among different species vary and are listed in a table to better illustrate SPB information (Fig. 5b)[86]. In *S. cerevisiae*, ScCnm67, and ScNud1 are the outer plaque components and their orthologues in *S. pombe* are SpSid4 and SpCdc11; ScCmd1 (Cmd1, calmodulin), ScSpc42, and ScSpc29 are central plaque components and SpCam1 is the only orthologue which can be found in *S. pombe*. ScSfi1, ScCdc31,

and ScKar1 are the components of half-bridge appendages with their orthologues of SpSfi1 and SpCdc31 in *S. pombe*. Among those components, Spc42 is an essential central plaque protein with its N-terminus associating with Spc110 (an inner plaque receptor protein). Spc29 binds to both C-Spc110/Cmd1 and Spc42 which functions as a linker between the central and inner plaques. Spc110 as a receptor protein interacts with the γ-TuSC at the nuclear side of the SPB. In addition, the C-terminus of Spc42 binds to the C-terminus of Cnm67 and the N-terminus of Cnm67 binds to Nud1, an outer plaque protein required for mitosis exit. Additionally, the receptor protein Spc72 at the cytoplasmic side of SPB binds via its C-terminus to Nud1. Spc72 interacts with the γ-TuSC at the cytoplasmic side[87]. Kar1 as a component of the half-bridge is important for SPB reorganization during the G1 phase and the re-localization of Spc72 from the outer plaque to the half-bridge in G1. However, cytoplasmic MTs organized from the half-bridge are not vital for normal mitotic progress but are necessary for cell karyogamy[88, 89].

MT nucleation function in budding yeast is provided by Spc97/Spc98/γ-Tubulin which are localized at both cytoplasmic and nuclear sides to nucleate cytoplasmic MTs (cMTs) and the nuclear MTs (nMTs), respectively. cMTs are important for the proper position of mitotic spindles in the nucleus before cell division occurs due to the nuclear envelope remaining intact during cytokinesis in yeast. Combined with the SPB components above, a cartoon scheme is shown to better illustrate the whole structure of the SPB (Fig. 5c)[87].

a

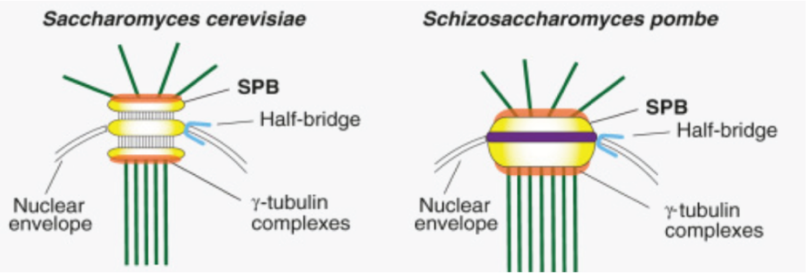

b

	S. cerevisiae	A. gossypii	C. albicans	S. pombe
γ-TuC/microtubule nucleation	ScTub4	AgTub4	CaTub4	SpGtb1
	ScSpc97	AgSpc97	CaSpc97	SpAlp4
	ScSpc98	AgSpc98	CaSpc98	SpAlp6
	--	--	--	SpGfh1
	--	--	--	SpMod21
	--	--	--	SpAlp16
	--	--	CaMzt1	SpMzt1
	ScStu2#	AgStu2	CaStu2	SpAlp14
receptors	ScSpc110	AgSpc110	CaSpc110	SpPcp1
	ScSpc72	AgSpc72	CaSpc72	SpMto1
	--	--	--	SpMto2
core/central plaque	ScCmd1	AgCmd1	CaCmd1	SpCam1
	ScSpc42	AgSpc42	--	--
	--	--	--	SpPcp89*
	ScSpc29	AgSpc29	--	--
outer plaque	ScCnm67	AgCnm67	C7_03620C_A	SpSid4
	ScNud1	AgNud1	CaNud1	SpCdc11
half-bridge	ScSfi1	AgSfi1	CaSfi1	SpSfi1
	ScCdc31	AgCdc31	CaCdc31	SpCdc31
	ScKar1	AgKar1	--	--
	ScMps3	AgMps3	--	SpSad1
SPIN/SPB insertion	ScMps2	AgMps2	--	SpKms2
	ScNdc1	AgNdc1	CaNdc1	SpCut11
	ScBbp1	AgBbp1	--	--
	ScNbp1	AgNbp1	--	--
	--	--	--	SpCut12

c

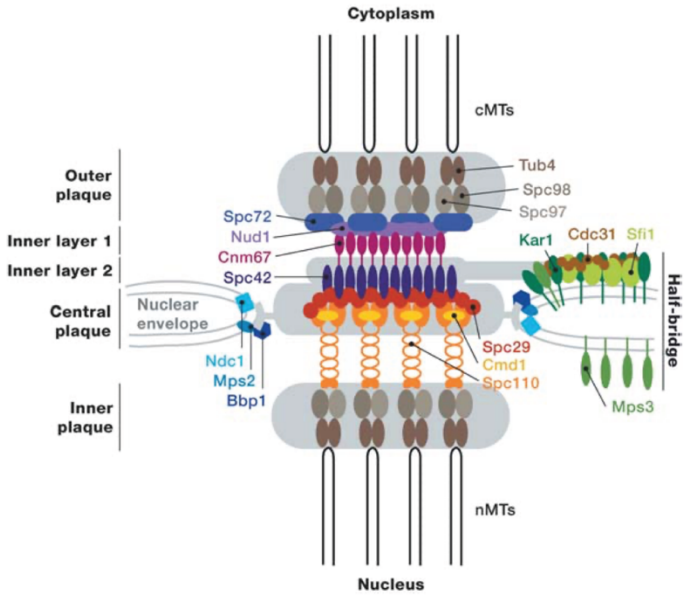

Figure 5: Microtubule nucleation in yeast

(a) The overall architectures of the SPB in yeast. The panel is from Catarina Nabais et al., 2020[85].

(b) Table of fugal SPB components. The SPB proteins belonging to *S. cerevisiae* and *S. pombe* are encircles by red boxes. The panel is taken from Sue L Jaspersen, 2021[86].

(c) The structure of SPB components. The panel is taken from Sue L. Jaspersen and Mark Winey, 2004[87].

1.4 γ-tubulin ring complex

1.4.1 γ-tubulin

MTs are not only nucleated from centrosomes but also from other organelles and cellular structures such as chromatin. In mice oocytes, *Xenopus* oocytes, plants, and all acentrosomal cells, MTs are nucleated in the absence of centrosomes[90-93]. Besides, in centrosome-depleted cells, spindles can still form and the centriole-lacking mutant flies can develop into morphologically normal flies but with defects in cilia formation [94, 95]. This indicates the indispensable role of centrosome plays in cilia formation. The centrosome as mentioned above is composed of two centrioles with a '9-fold pinwheel' structure[96]. The '9-fold pinwheel' centrioles were identified as arrays of triplet MTs to function as basal bodies of a primary cilium or beating cilia in specialized cells. Defects of cilia have been increasingly recognized to be related to several genetic diseases named collectively ciliopathies[97, 98]. Thus, the centrosome might be more important for cilia formation than for MT nucleation.

Back to the topic of the MTs – MTs were found to be surrounding the centrosome and nucleated from the centrosome. The osmiophilic material around the centrioles, termed 'pericentriolar matrix' (PCM), was the functional part for MT nucleation[99]. γ-tubulin, a conserved protein of the PCM, was first found in the acentrosomal filamentous fungus *Aspergillus nidulans* (*A. nidulans*), then, γ-tubulin was also found in acentrosomal MTOCs such as the nuclear envelope MT nucleating center and the cell cortex MT nucleating center in plants. Importantly, depletion of γ-tubulin resulted in cell lethality[100-103].

In multi-ciliated epithelial cells, γ-tubulin was also found at the apical membrane where basal bodies of cilia are located, which indicates that γ-tubulin might also play an important role in cilia formation[104]. In differentiated myotubes, proteins associated with microtubule nucleation were found to be relocated from the centrosome to the nuclear envelope[105]. In mitotic animal cells, γ-tubulin was not only found at the centrosomes but also along spindle MTs or even between the separated chromosome masses[106], and MTs/γ-tubulin can also be found at the cytoplasmic face of the Golgi complex[107]. With blocking experiments using antibodies against γ-tubulin, MT formation was impaired[108]. Additionally, the γ-tubulin localization in different compartments of cells also overlapped with most of the acentrosomal MT organizing center sites, which further indicates the

general importance of γ-tubulin for MT nucleation. In yeast, γ-tubulin is encoded by *TUB4* and is one of the γ-TuSC components that is required for MT nucleation[109-111].

1.4.2 γ-tubulin ring complex in higher eukaryotes

Microtubule nucleation is not strictly dependent on the centrosome since the finding of PCM protein of γ-tubulin being anchored at the centrosome and non-centrosome MTOCs. Since the discovery of γ-tubulin in *A. nidulans*[100], interacting proteins of γ-tubulin were searched for in different organisms. The concept of the 'γ-tubulin ring complex (γ-TuRC)' was introduced after the purification of the γ-tubulin complex containing at least 7 components from *Xenopus*[52]. The human γ-TuRC components GCP2/3/4/5/6/γ-tubulin were continuously identified[112-114]. NEED1 (GCP-WD protein) was later identified to be another γ-TuRC component and depletion of NEDD1 in human cells resulted in the detachment of the γ-TuRC from centrosomes and strongly reduced MT nucleation at centrosomes[115].

Having noticed the importance of γ-tubulin in forming the γ-TuRC in different species, the first X-ray structure of human γ-tubulin bound to GTPγS (a non-hydrolyzable GTP analog) was solved with a 'curved' conformation which is similar to that observed for GDP-bound, unpolymerized α/β tubulins[116, 117]. The human γ-tubulin bound to GTPγS adopts a 'curved' conformation which is similar to that observed in the unpolymerized αβ-tubulins[116]. In addition, the binding affinities for γ-tubulin and β-tubulin to GTP are the same and both of them prefer to bind GTP in the presence of GDP, thus, this similarity between γ-tubulin and β-tubulin might indicate the same regulation function of γ-tubulin and β-tubulin, meaning the association with αβ-tubulins might trigger the conformational changes of γ-tubulin (from a 'curved' structure to a 'straight' structure)[117]. Too long, too complicated - rephrase! Moreover, a mutation in γ-tubulin that impairs GTP-binding affects α/β-tubulin recruitment to γ-tubulin. Thus, GTP binding to γ-tubulin is important for the association with αβ-tubulins and MT nucleation[118]. To better understand this point, more structural information from the whole level of γ-TuRC and the γ-TuRC bound MT will be required. Fortunately, with the development of cryo-EM technology and its more common use in the biological field, the structures of γ-TuRCs from various species have been obtained in recent years. In common, they all have a cone-shaped structure and form an

asymmetric ring complex (14-spoke complex) with a molecular weight of ~ 2.2-megadalton. In *Xenopus* γ-TuRC, 5 units of GCP2/3, 1 unit of GCP4/6, and 1 unit of GCP5/6 form into a 14-spoke ring capped with 14 units of γ-tubulins which functions as a MT template, additionally, the density from the lumen bridge of the Actin was verified by immunoblotting, however, there were still densities remained unassigned. Besides, the structure seemed to lack densities of NEDD1/NME7 and MZT1 (MOZART1) identified in mass spectrometry (Fig. 6a)[2].

Human γ-TuRC is also composed of 14 spokes presented by its cryo-EM structure[119]. In addition, combined with the MZT1-GCP6-NHD structure resolved by X-ray crystallization and the structural prediction, several low-resolution densities were matched to MZT1 and MZT2, and the density bound to the 13th spoke was proposed to be the two helixes of γ-TuNA (γ-TuRC receptor protein) (Fig. 6b)[119, 120]. With the recombinant expression system, the successfully reconstituted human γ-TuRC was obtained when additionally co-expressed with AAA+ ATPase RUVBL1/RUVBL2. The overall structure contains several MZT1-like densities bound to the N-termini of GCP3 and GCP5 and these densities were confirmed to be MZT1b y docking the solved human MZT1 structure published in the year 2020 into the reconstituted human γ-TuRC (Fig. 6c)[120, 121].

NEDD1 as a subunit of human γ-TuRC is involved in the localization of γ-TuRC to the centrosomes in interphase, and the phosphorylated NEDD1 is associated with the spindle γ-tubulin and promotes the spindle nucleation in the mitotic phase[115]. The Nucleotide diphosphate kinase NME7, as an identified subunit of human γ-TuRC, is involved in regulating MT nucleation, however, its depletion had no impact on γ-TuRC assembly[122]. Unfortunately, no cryo-EM structures of γ-TuRC containing NEDD1 or NME7 have been obtained yet. MZT1 as a subunit of human γ-TuRC is involved in anchoring γ-TuRC to MTOCs with the interaction of NEDD1 and its knockdown causes no impact on γ-TuRC assembly, however, human MZT1 in the reconstituted γ-TuRC system was found localized at the luminal bridge which might be important for the intact γ-TuRC assembly[121, 123, 124]. MZT2/GCP8 as another subunit of human γ-TuRC is involved in γ-TuRC recruitment and MT nucleation at interphase but not important for the γ-TuRC assembly and the mitotic spindle formation[125]. Fortunately, the various species of γ-TuRCs'

structures have been resolved and it helps us to better understand the γ-TuRC assembly and the initiation of MT nucleation with γ-TuRC as a template.

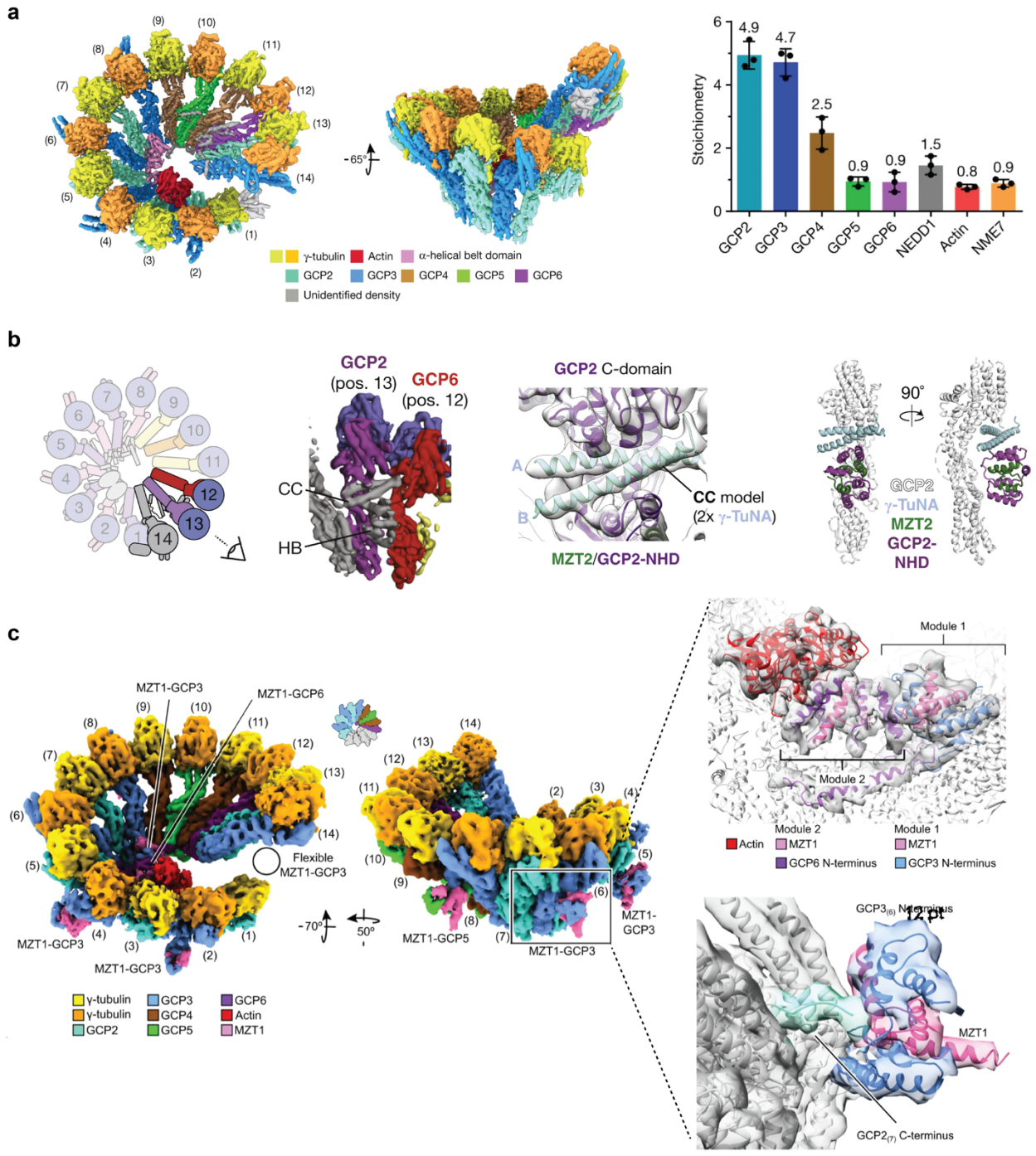

Figure 6: The structures of γ-TuRCs in higher eukaryotes

(a) The cryo-EM structure of γ-TuRC from *X. laevis* (*Xenopus laevis*). 14-spoke ring-like

structure with the identified and unassigned densities. NEDD1 and NME7 are not seen on the structure. The panel is taken from Peng Liu et al., 2020[2].

(b) The structure of γ-TuRC from *homo sapiens*. Combined with the crystal structure of MZT1-GCP6, the proposed MZT1/MZT2, CM1 (CDK5RAP2)-bound γ-TuRC positions were depicted. The panel is from Michal Wieczorek et al., 2020[120].

(c) The cryo-EM structure of reconstituted γ-TuRC from *homo sapiens*. The densities proposed to be MZT1/2 are shown. The panel is from Martin Würtz and Erik Zupa et al., 2022[121].

1.4.3 γ-tubulin ring complex in fungi

1.4.3.1 γ-tubulin ring complex in *S. cerevisiae*

In most eukaryotes, several copies of γ-TuSC subunits combined with at least three other accessory proteins assemble into a ~2-MDa γ-TuRC[52, 126]. In *S. pombe*, all five human GCPs can be found (alp4+: GCP2, alp6+: GCP3, gfh1+: GCP4, mod21+: GCP5 and alp16+: GCP6)[127-130], in *A. nidulans*, all five human GCP homologs of GCPB (GCP2), GCPC (GCP3), GCPD (GCP4), GCPE (GCP5) and GCPF (GCP6) together with γ-tubulin constitute the core components of *A. nidulans* γ-TuRC (γ-tubulin was first identified in *A. nidulans*)[100, 131]. However, in *S. cerevisiae* and *C. albicans, the core* γ-TuRC components contain only Spc97 (GCP2), Spc98 (GCP3) and Tub4 (γ-tubulin)[51, 132, 133]. Moreover, MZT1, another human MOZART protein also exists in *S. pombe*, *A. nidulans*, and *C. albicans* (*Candida albicans*) but not in *S. cerevisiae*[133-135]. Thus, uncovering how γ-TuRCs are assembled and function as the MT templates across different species is important for the understanding of the cell cytokinesis mechanisms at the molecular level. As the MT nucleation template, γ-TuRC can form a cap-like structure at the minus end of MTs and constrain thirteen filament geometry in cells[136, 137]. This year, the capped minus-end structures from *Xenopus* and humans have been resolved which provides the direct evidence for γ-TuRC as an MT template[138, 139].

As a unicellular eukaryote, *S. cerevisiae* γ-TuSC, a 300-kDa gamma-tubulin small complex, is the basic unit and component of the MT nucleation complex which is composed of one unit of Spc97/Spc98 and two copies of Tub4p (γ-Tubulin in yeast) as mentioned above[50]. *In vivo*, MTs from SPB mediated by γ-TuRC could also be observed

in *S. cerevisiae* which indicates a conserved mechanism of utilizing γ-TuRC as a MT nucleation template between yeast and higher eukaryotes even lacking extra accessory proteins in some yeast species[140, 141]. To better understand how γ-TuRC is assembled from γ-TuSC in yeast, the cryo-EM structure of the *S. cerevisiae* γ-TuSC at 25-Å resolution was solved in the year 2008, which presented as a Y-shaped structure with two Tub4 proteins localized at the C-terminal ends of the arms formed by Spc97 and Spc98[142]. Interestingly, they also found different subpopulations of γ-TuSCs with the variable orientations of the Tub4 molecules, thus, the flexible orientation of Tub4 might be important for the whole structural conformational changes when the ring complex forms (Fig. 7a)[142].

BRB80 can also promote the spontaneous assembly of purified *S. cerevisiae* γ-TuSC into oligomers *in vitro*. However, the addition of $Spc110^{1-220}$ allowed γ-TuSC oligomer formation even under higher salt conditions (Fig. 7b)[141]. Briefly, the SPB γ-TuSC receptor proteins are classified into two types: the cytoplasmic side one of Spc72 (*S. pombe* Mto1 and *A. nidulans* ApsB) and the nuclear side one of Spc110 (*S. pombe* Pcp1 and *A. nidulans* PcpA)[132, 143-148]. With the addition of $Spc110^{1-220}$, the cryo-EM structure of the reconstructed γ-TuSC oligomer at a resolution of 8 Å was solved in *S. cerevisiae*[141]. Correspondingly, with the higher resolution, the GRIP1 and GRIP2 (GRIP: Gamma Ring Protein) domains of Spc97p/Spc98p and their interaction interfaces at the N-terminal ends were distinguished. This verifies Spc110 as a stabilizer for the γ-TuSC oligomerization (Fig. 7b). Additionally, the rearrangement of γ-tubulin molecules was observed in γ-TuSC oligomer, indicating the importance of γ-tubulin positions for the formation of γ-TuSC oligomers. Moreover, this conformational change could be further induced by the binding of α/β-tubulins to γ-tubulins[141].

To further explore how the MTs are growing from the oligomerized γ-TuSC *in vivo*, cryo-tomography was used for analyzing the capped minus-ends and MTs from the isolated spindle pole bodies in *S. cerevisiae*. In contrast to an open ring formed by the reconstituted γ-TuSC/$Spc110^{1-220}$ complex, the MT minus-end capped γ-TuRC adopted a closed architecture (Fig. 7c)[137]. Based on previous work, the disulfide crosslinked mutated γ-TuSC (S58C/G288C on γ-tubulin) in complex with GST-tagged $Spc110^{1-220}$ (γ-$TuSC^{CC}$ oligomer) was designed and used for cryo-EM analysis to achieve a resolution

of 6.9 Å. It turned out that the γ-TuSC^{CC} oligomer was in a closed state[137]. Moreover, the MT nucleation assay further verified that γ-TuSC^{CC} oligomer had higher MT nucleation activity. Besides, the MT nucleation assay provided the information to use α/β-tubulins from the same species to better reflect the real MT nucleation efficiency[137].

With the higher-resolution structure of 6.9 Å for γ-TuSC^{CC} oligomers, 7 units of Spc110$^{1-220}$ bound to the 7 units of γ-TuSC^{CC} were observed, and the better-resolved structure showed additional detailed binding information about how Spc110$^{1-220}$ interacts with both of Spc97p and Spc98p via their GRIP1 domains: a modeled two-stranded and 44-amino acids coiled coils of Spc110$^{1-220}$ are located between residues 77-97 of GCP2 and further up with residues 119-126 of GCP3 (Fig. 7d). The higher-resolution γ-TuSC^{CC} structure proposed a binding mode of Spc110$^{1-220}$ with γ-TuSC: Spc110$^{1-220}$ runs along the center of filament formed by the continuum of γ-TuSC oligomers. However, such filaments were not observed in the complex of γ-TuSC and Spc110$^{1-401}$ (Fig. 7c), which might be due to the additional C-terminal amino acids stopping the helical packing at the filament center position[137].

Even though a higher-resolution structure of the γ-TuSC^{CC} oligomer was obtained, the resolution was still not high enough to see the exact amino acids of Spc110 bound to the complex of γ-TuSC^{CC} oligomer. With the combination of X-ray crystallography, cryo-EM structure analysis, and XL-MS (crosslinking mass spectrometry), the two-stranded coiled coils (44 amino acids) of Spc110$^{1-220}$ on γ-TuSC^{CC} oligomer structure could be identified as the region of 164-208 of Spc110[149]. Furthermore, with the XL-MS technology and cryo-EM analysis of the γTuSC^{SS} (disulfide trapped 'closed' γTuRC^{SS})[137, 141], the Spc110^{CM1} helix of 117-141 and its connecting region of Spc110$^{164-208}$ was fitted into the corresponding densities (Fig. 7e), which provided more information of how Spc110 contacts the γ-TuRC and promotes the conformational change to fit into MT geometry[149]. However, using the mutated γ-tubulin (γ-TuSC^{SS}) for the reconstructed structure analysis may not convincingly reflect the conformational changes that γ-TuRC undergoes *in vivo*, transitioning from an open to a closed state.

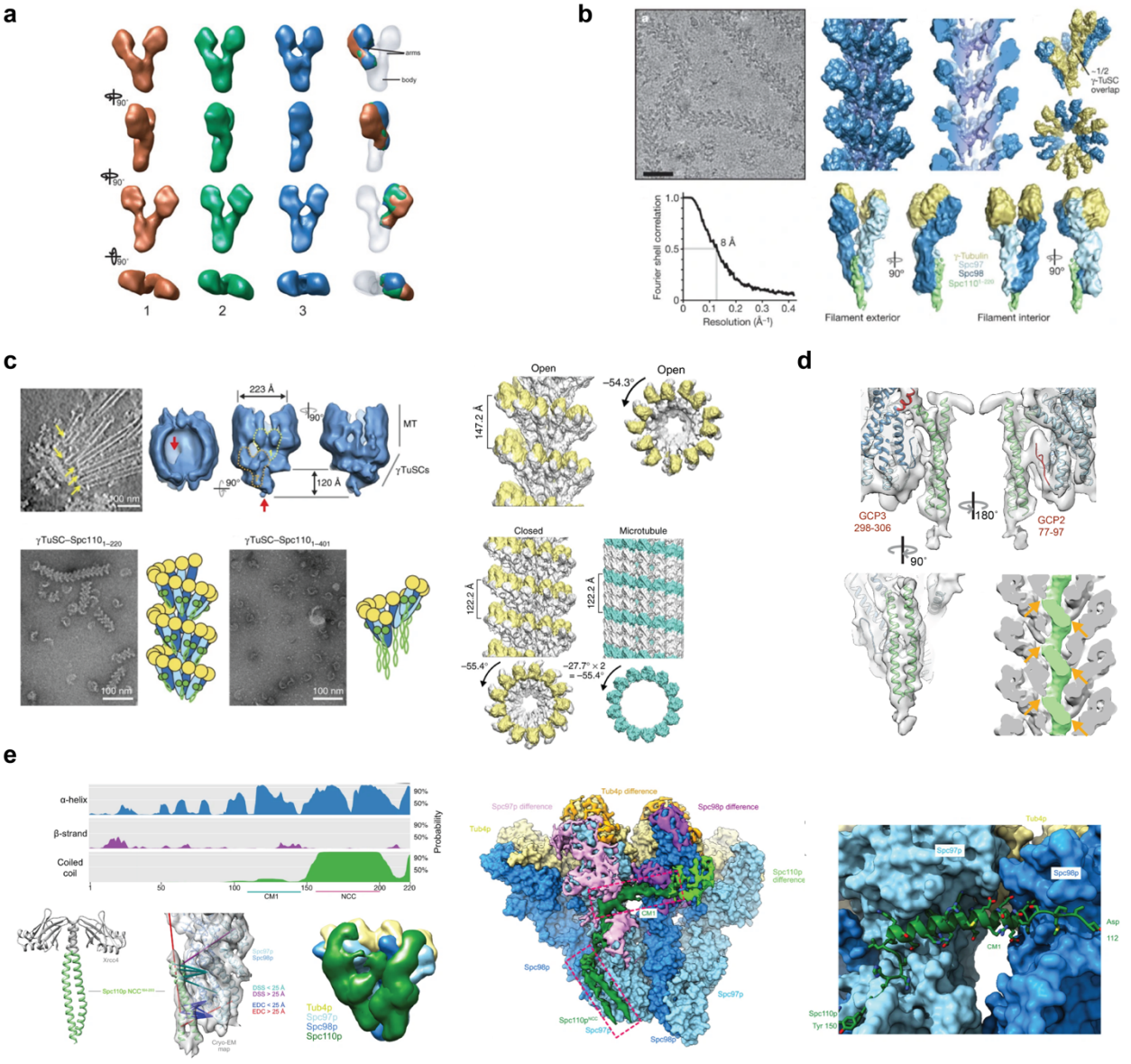

Figure 7: γ-tubulin ring complex formation in *S. cerevisiae*

(a) Three-dimensional reconstructions of γ-TuSC in different views. The 3 different subpopulations of γ-TuSCs are shown in brown (1), green (2), and blue (3) colors, respectively. The panel is from Justin M. Kollman et al., 2008[142].

(b) Cryo-electron reconstructed structure of γ-TuSC oligomer combined with Spc110$^{1-220}$. With the addition of Spc110$^{1-220}$, and the γ-TuSC filament was formed under a higher salt buffer of HB100 (40 mM Hepes pH 7.6, 100 mM KCl, 1 mM EGTA, 1 mM $MgCl_2$). The panel is taken from Justin M. Kollman et al., 2010[141].

(c) The native yeast γ-TuRC from isolated SPB, the reconstituted γ-TuRCs from

co-purified complexes of γ-TuSC/Spc110$^{1-220}$ and γ-TuSC/Spc110$^{1-401}$. The panel is taken from Justin M. Kollman et al., 2015[137].

(d) The additional density was modeled to be Spc110 on the reconstituted γ-TuRC structure. The closest contacts with Spc110 are between residues 77-97 of GCP2 and further up the structure with residues 119-126 of GCP3. The panel is taken from Justin M. Kollman et al., 2015[137].

(e) The bound Spc110 on the reconstituted γ-TuRC structure was the region of 112-203 of Spc110. Region 112-150 of Spc110^{CM1} is bound to Spc97 and the neighboring Spc98, whereas 164-203 (the N-terminal side of Spc110^{CM1}) of Spc110 is bound to Spc97. The panel is taken from Axel F Brilot et al., 2021[149].

1.4.3.2 γ-tubulin ring complex formation in *C. albicans*

C. albicans is a commonly encountered and polymorphic fungal pathogen mainly found in mucosal surfaces and is a common constituent in ~50% of the human microflora population[150]. It can be life-threatening and cause mortality with a lethal rate of 40% in immunocompromised patients[151]. The morphology of *C. albicans* can be classified into three different forms: a) the normal unicellular one, b) cells with pseudohyphae, and c) cells with hyphae. In brief, the normal unicellular form is most of the time harmlessly colonizing with host cells, whereas the other two forms of *C. albicans* are infectious[150, 152-154]. The pathogenicity of *C. albicans* invoked interest in studying this organism to better understand the mechanism of the MT nucleation and the hyphae formation.

The MT nucleation unit in *C. albicans* is the Caγ-TuSC containing CaSpc97/CaSpc98/CaTub4 which is conserved in *S. cerevisiae,* additionally, the protein of CaMzt1 found in *C. albicans* is absent in *S. cerevisiae.* CaMzt1 can bind to Caγ-TuSC and the negative stain EM presented a 'Y-shape' structure formed by the Caγ-TuSC/CaMzt1 complex (Fig. 8a)[133]. To investigate the function of CaMzt1 in *C. albicans*, the GFP-tagged *CaMzt1* was used and expressed in cells. These *in vivo* experiments showed that CaMzt1 was required for the localization of γ-TuSC to the SPB and MT formation (Fig. 8b)[133]. MST (Microscale thermophoresis) experiments verified that the N-terminal domain of CaSpc98 was important for the interaction with CaMzt1, and CaMzt1 can promote the big aggregate formation of γ-TuSC oligomers under specific buffer

conditions (BRB80, 150 mM KCl) when CaMzt1 was incubated with γ-TuSC (Fig. 8c). In addition, when co-purifying the complexes of Caγ-TuSC/GST-CaSpc110-N with and without CaMzt1 expressed in insect cells, the gel filtration experiment showed a higher oligomerization ratio formed in the presence of CaMzt1. Furthermore, the peak samples from Caγ-TuSC/GST-CaSpc110-N with and without CaMzt1 gel filtration fractions checked by negative stain EM also verified the addition of CaMzt1 was helpful for a more regular oligomer formation of Caγ-TuSC. However, such a positive effect was not so obvious in the condition of co-incubation of Caγ-TuSC, CaSpc72-N, and CaMzt1 when tested by MST (Fig. 8d). Conclusively, the different combinations of Caγ-TuSC, CaSpc110-N, CaSpc72-N, and CaMzt1 confirmed the positive impact of the receptor proteins (CaSpc110-N, CaSpc72-N) for the oligomerisation of Caγ-TuSC *in vitro*[133]*.* Additionally, it seems that the combination of CaSpc110-N and CaMzt1 had a stronger impact on the γ-TuSC oligomer formation based on the MST binding affinity measurement, however, even combining all the purified components (Caγ-TuSC/GST-CaSpc110-N/CaMzt1), regular ring-like structures were not obtained in the end (Fig. 8d, bottom)[133]. Considering the high degree of heterogeneity of the Caγ-TuSC/GST-CaSpc110-N/CaMzt1 complex formed by GST-Spc110-N, there might be other factors involved in the formation of the MT nucleation unit on the nuclear side of the SPB. Surprisingly, there was no difference in the binding affinity between CaSpc72-N and Caγ-TuSC/CaMzt1 or Caγ-TuSC alone, which indicates a different mechanism of CaMzt1 involved in the oligomerisation of Caγ-TuSC at the cytoplasmic side[133].

In the previous study, the cryo-EM structure of *C. albicans* γ-TuSC was solved as a Y-shape structure which is similar to *S. cerevisiae* γ-TuSC (Fig. 8e)[3, 141, 142]. Unfortunately, higher oligomers were not found in Caγ-TuSC which is reasonable considering that the oligomeric-associated factors of CaSpc72/CaSpc110 and CaMz1[141] were not included in this analysis[3, 133, 141].

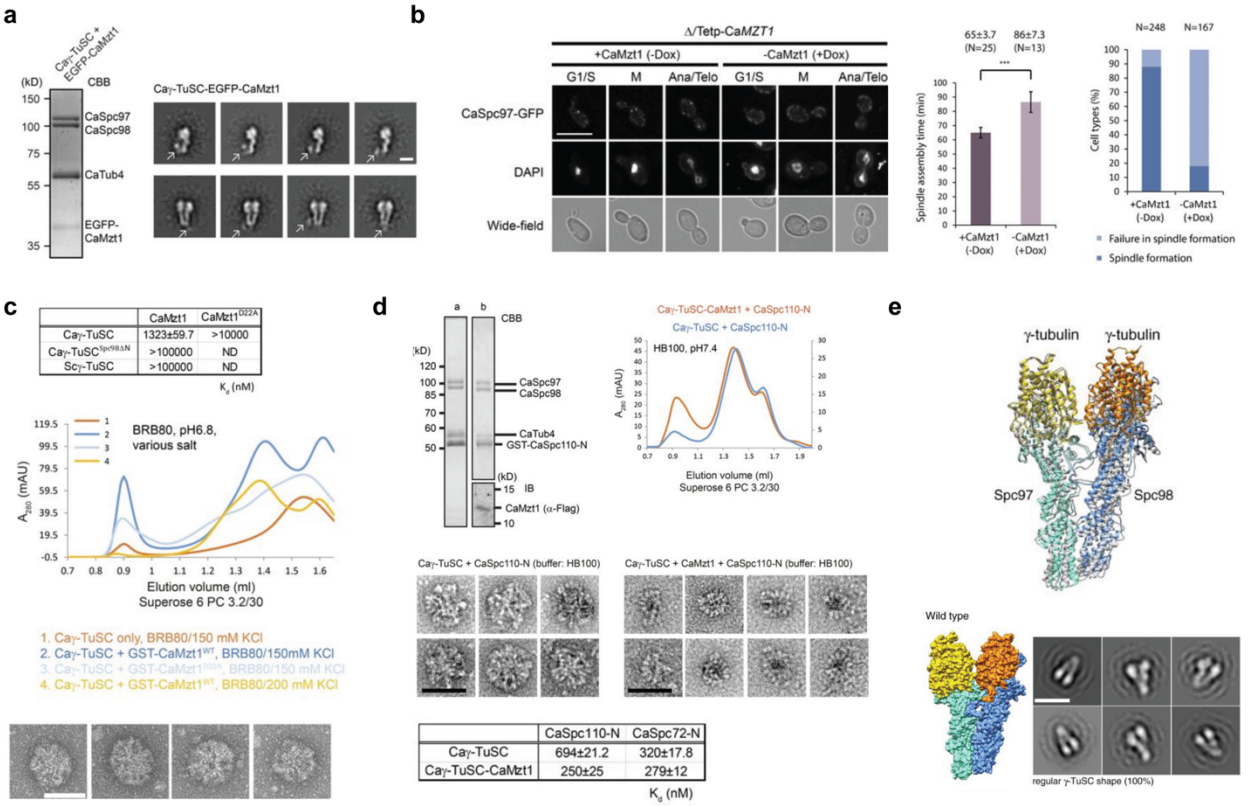

Figure 8: γ-tubulin ring complex formation in *C. albicans*

(a) The complex of Caγ-TuSC/CaMzt1. The negative stain EM showed a 'Y-shape' structure formed by Caγ-TuSC/CaMzt1. The panel is taken from Tien-chen Lin et al., 2016[133].

(b) Depletion of CaMZT1 delocalizes Caγ-TuSC from SPBs and disrupts MT organization. The quantifications of spindle assembly time and cell type ratio with normal spindle formation and failure in spindle formation were shown. The panel is taken from Tien-chen Lin et al., 2016[133].

(c) CaMzt1 binds to the N-terminal domain of CaSpc98. The Caγ-TuSC/CaMzt1 complex was formed into big aggregates under the buffer of BRB80/150 mM KCl. The panel is taken from Tien-chen Lin et al., 2016[133].

(d) CaSpc110-N and CaMzt1 are both required for the Caγ-TuSC oligomer formation. CaSpc72-N showed the same binding affinity to Caγ-TuSC and Caγ-TuSC/CaMzt1, whereas CaSpc110-N showed approximately 2.5 times higher binding affinity of Caγ-TuSC/CaMzt1 compared with Caγ-TuSC. The panel is taken from Tien-chen Lin et al., 2016[133].

(e) The cryo-EM structure of Caγ-TuSC. The negative stain EM after 2D class averaging analysis was shown. The panel is taken from Erik Zupa et al., 2020[3].

1.4.4 γ-tubulin ring complex associated proteins

The XMAP215 family of proteins spans *X. laevis* XMAP215, ch-TOG (colonic-hepatic tumor-overexpressed gene) in mammalian cells, Msps (mini-spindles) in *Drosophila*, Dis1 and Alp14 in *S. pombe*, Stu2 in *S. cerevisiae* and CaStu2 in *C. albicans*, these are conserved MT-binding and MT-polymerizing promoting proteins[40, 41, 43, 155]. XMAP215 family proteins have been found to regulate MT stability in different ways. XMAP215 has been proposed to stabilize MT plus ends and functions as an MT-destabilizing factor. Msps in *Drosophila* was found to be localized to centrosomes and stabilize centrosomal MTs via the interaction with D-TACC (homolog of human TACC, the transforming acidic coiled-coil protein)[156-159]. Recently, XMAP215 was verified to be a bona-fide MT nucleation factor in *Xenopus* egg extracts, which cooperates with γ-TuRC synergistically to nucleate MTs in the cytoplasm *in vitro*. Furthermore, a direct interaction between human γ-tubulin and the C-terminus of XMAP215 was confined *in vitro* (Fig. 9a)[160]. However, the mechanism of such a model shown in Fig. 9a proposed by Petry group waits to be verified *in vivo* and on the molecular or structural level. Moreover, whether such a function of XMAP215 in *Xenopus* is shared in other higher eukaryotic species such as in human cells is also waiting to be tested. Last but not least, what is worth to be mentioned is that budding yeast Stu2 was found to be an MT plus-end destabilizer, more interestingly, Stu2 was also found to be localized to SPBs, nuclear/astral MTs and kinetochores, and depletion of Stu2 leads to cell cycle arrest, failure of mitotic spindle elongation and a decreased number of astral MTs[161-166]. In *S. cerevisiae*, the in vivo/vitro experiments conducted by Judith Gunzelmann et al have provided more clues in the understanding of how Stu2 recruits α/β-tubulin dimers to the cytoplasmic side of SPB via the interaction with the receptor protein of Spc72 and the loss of the interaction of Stu2 with Spc72 results in the detached asters (Fig. 9b)[164, 167]. However, whether Stu2 functions as the recruitment factor of the first layer of α/β-tubulin dimer to the MT template of γ-TuRC or not, and how Spc72 interacts with γ-TuSC and Stu2 remains unclear both from the molecular and structural level.

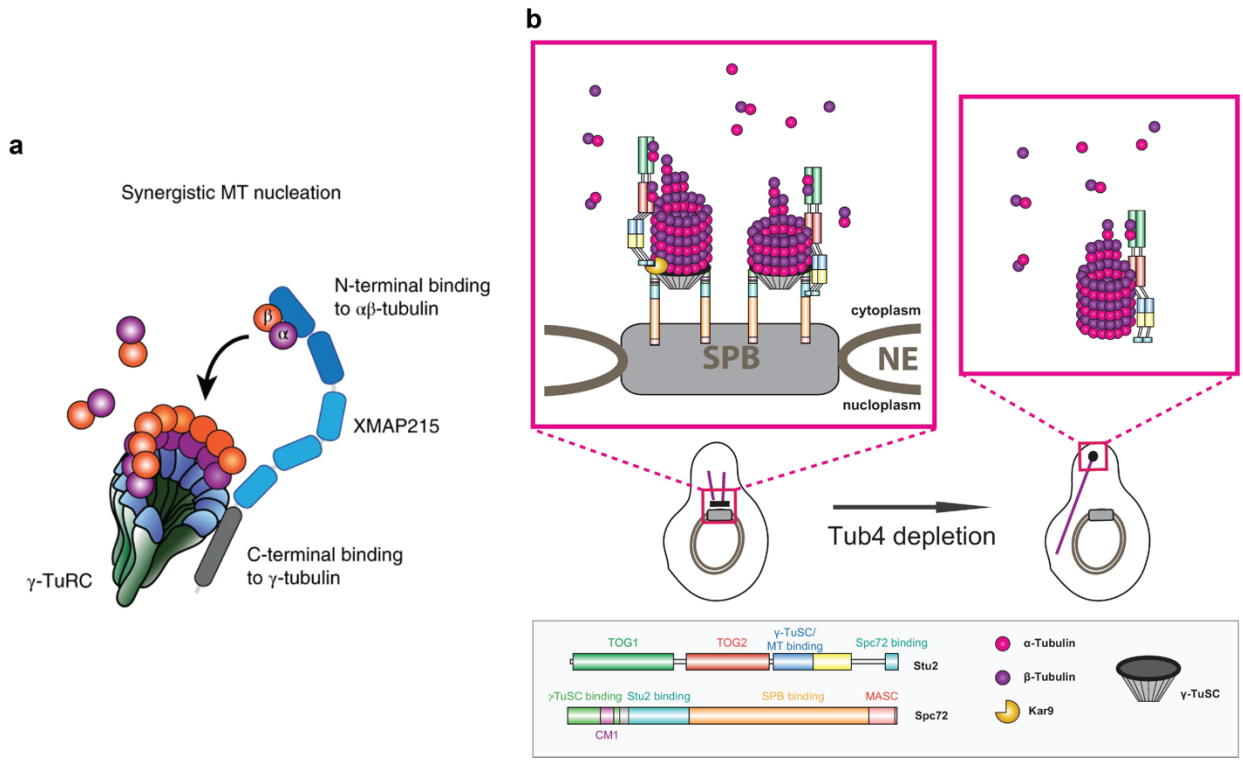

Figure 9: TOG proteins and the proposed models in different organisms

(a) The proposed model of XMAP215 participating in microtubule nucleation with the template of γ-TuRC in *Xenopus*. The panel is taken from Akanksha Thawani et al., 2018[160].

(b) The proposed model of Stu2 participating in microtubule nucleation with the template of γ-TuSC oligomers in budding yeast. The panel is taken from Judith Gunzelmann et al., 2018[167].

1.5 Cryo-EM technology and Alphafold 2 predictions used for the analysis of macromolecular complexes

Using cryo-EM analysis, an increased number of high-resolution structures of macromolecular complexes were reported (https://www.ebi.ac.uk/pdbe/emdb/statistics_main.html). With the improvement of cryo-EM technology, the development of a user-friendly image processing interface, and the increased computation power, the PDB and EMDB deposited structures were greatly expanded in recent years. However, the higher resolution of the structures to satisfy the direct visualization of the atomic position of amino acids in proteins (better than 1.5 Å) is

still difficult to achieve in most cases. In other words, resolutions from majorities of the solved protein ranged from 3-4 Å were just sufficient for the atomic model building[168]. However, there are a growing number of structures with resolutions in the 2-3 Å range that enable cryo-EM technology to be used in the biological and medical fields[169]. The cryo-EM technology that was developed for the observation of frozen-hydrated specimens can be traced to the 1980s[170]. Electrons are used for imaging the vitreous sample with a high resolution due to the short wavelength in cryo-EM technology. The high energy provided by electrons (1 to 20 electron/Å^2) used for biological samples is much overloaded compared to the normal tolerating range of 100–500 e–/Å^2 for the biological specimens. Thus, the sample will experience some degree of radiation damage. The electron source is emitted and passes through the aperture, a condenser lens and scatters on the object, the remaining electrons continue to pass through the objective lens, a second aperture, and a projector lens and finally form into the raw image data (Fig. 10c)[171-173]. After data collection, data needs to be analyzed to obtain the 3D structure, the microscope phase contrast transfer function (CTF) correction and the Fourier transformation are used to determine the 3D density distribution for the object[173].

Negative staining EM is the common tool for judging the sample quality. Negative staining EM requires a low amount of sample. A heavy metal salt solution is used as the sample embedding reagent (normally uranyl acetate), which brings the highest contrast under transmission electron microscopy conditions (Fig. 10a)[174, 175]. In contrast to negative staining EM, cryo-EM requires 10 times more samples to compensate for the sample loss when samples are blotted onto the grids. Grids containing the sample were rapidly frozen in liquid ethane or propane (−182 °C) cooled by liquid nitrogen for long-time storage until the imaging acquirement (Fig. 10b)[176, 177].

As one of the most powerful tools for macromolecular complex structure analysis, the cryo-EM technology also has limitations such as the requirement for samples, which need to be well-purified with enough particle number and nice homogeneity[178]. Thus, until now, less than 0.1% of the protein universe has a published structure deposited in the PDB database (https://www.rcsb.org/).

AlphaFold 2 (AF2) is a machine-learning protein structure prediction tool, which has predicted more than 200 million protein structures in 2 years since it was published[179, 180].

Three principals were used in protein structure prediction: **(1) Homology modeling**: Homology modeling is based on the hypothesis that similar amino acid sequences bring out similar 3D structures, thus, the input protein sequence will first be matched to its homologous sequences from the structural database and based on the solved 3D structures, the model is produced and evaluated. **(2) De novo modeling**: De novo modeling is used for the proteins without aligned structures in the database and predicts the structure based on the amino acid sequence and the established laws of physics (quantum mechanics), which is dependent on calculating the free energy of the atomic coordination of amino acids and searching for the low energy state of the conformational structure. Once these 2 factors are satisfied, the de novo modeling is completed. To calculate the accurate free energy of a protein requires solving Schrödinger's equation[181], however, until now, completing such a huge amount of calculation is still out of humans' capability, thus, empirical formulae were used to calculate the free energy and this leads to the limitation of this theory to apply only to small proteins (10-80 amino acid length)[182]. **(3) ML-based modeling**: ML-based modeling utilizes ML algorithms to solve protein structures and to predict unknown structures, and the logic of deep learning (DL) is used in ML algorithms. DL has developed fast in recent years benefiting from the growing data volume, the improvement of computing power, and algorithm optimization. AF2 is the best example of DL application in the protein structure prediction field. Several steps of AF2 are required for obtaining the predicted structures from the amino acid sequences: (1) module input and conduct MSA by aligning the input sequence with its homolog sequences. (2) Evoformer module, a deep learning module. (3) The third one is the structure module to translate the most representatively predicted protein structure to a 3D-atom model to be visualized (Fig. 10d)[182].

The application of AF2 has been widely used in biology fields such as structural biology, protein design, protein function prediction, protein-protein interaction, and drug discovery (Fig. 10e)[182]. In the case of protein-protein interaction predictions, the extended AF2 named AlphaFold-Multimer published by Evans et al. was used for the heteromeric interface interaction prediction and has reached 23% accuracy[183]. The recently released updated version of AlphaFold 3 has improved the predicted accuracy for protein-ligand

interactions such as the protein-nuclei acid interactions and antibody-antigen interactions[184].

In conclusion, the combined use of cryo-EM technology and AlphaFold series (AF2, AF3, and so on) in the future will be the strategy for obtaining higher-resolution macromolecular structures in the biological field and the protein-ligand complex structures in the field of medicine, which can speed up fundamental research and the application into products.

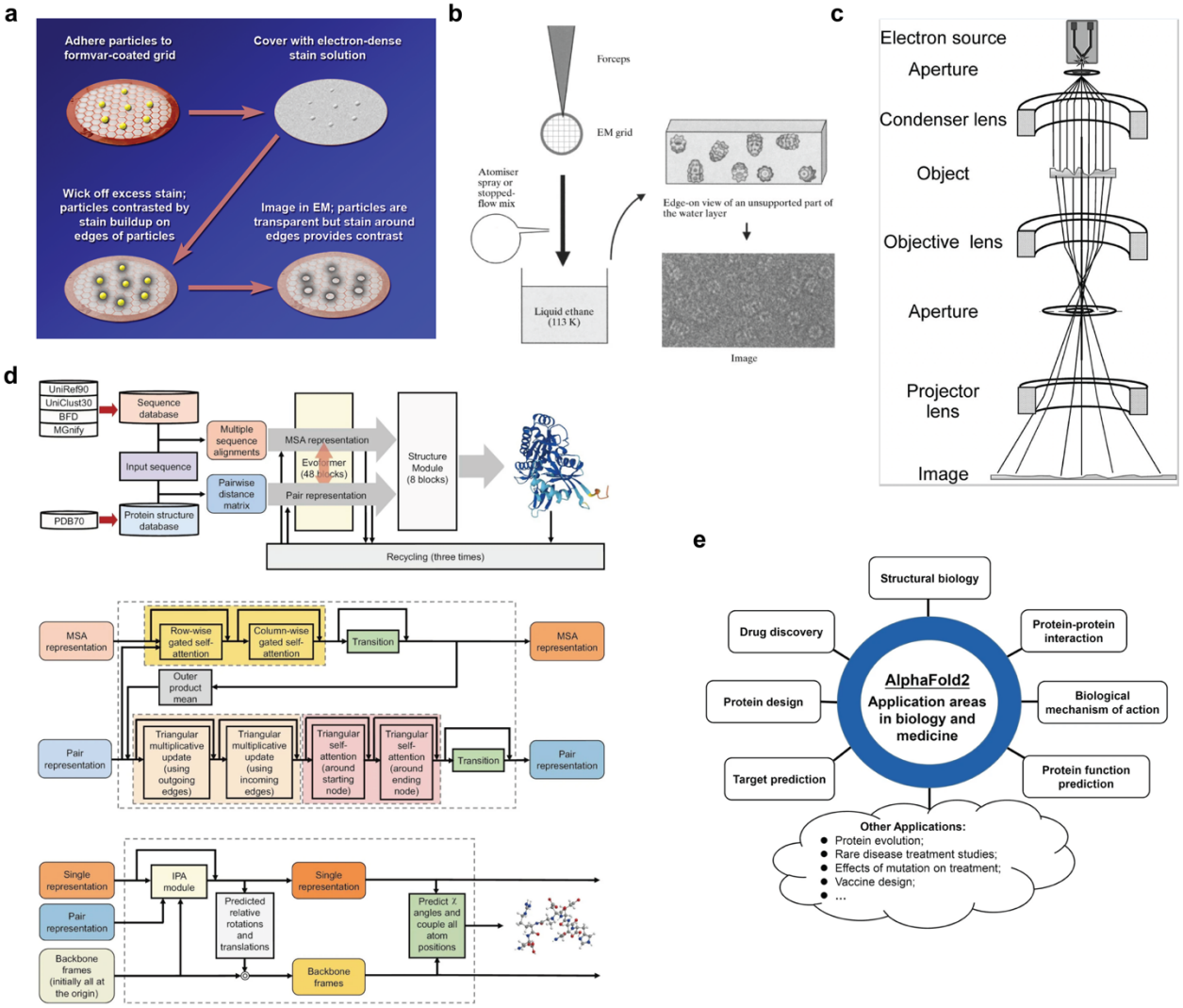

Figure 10: Cryo-EM flowchart and the AlphaFold2 prediction

(a) The flowchart of negative stain sample preparation. The panel is taken from Rachel Hart, 2020[175].

(b) The flowchart of cryo-EM sample preparation. The panel is taken from H. R. Saibil, 2000[177].

(c) The introduction of cryo-EM and image collection. The panel is taken from E. Orlova and H.R. Saibil, 2011[173].

(d) The schematic work principle and flowchart of AF2. The panel is taken from Zhenyu Yang et al., 2023[182].

(e) The applications of AF2 in the fields of biology and medicine. The panel is taken from Zhenyu Yang et al., 2023[182].

2 Aims of the thesis

γ-Tubulin ring complex as the MT nucleation template has been verified in various species, especially in higher eukaryotes such as *Drosophila*, *Xenopus*, and *Homo sapiens*. Here in this study, I would like to investigate the MT nucleation mechanism in yeast of *C. albicans* because it is unicellular and encodes only for Spc97/98 compared to GCP2-6 in higher eukaryotes or other yeast species such as *S. pombe*. Aiming to expand our knowledge of the MT nucleation mechanisms among different organisms promoted me to study the structural insights of γ-tubulin small and ring complexes in *C. albicans*. The Bac-to-Bac system and the MultiBac system are chosen to be used for testing the γ-tubulin small/ring complex expression in insect cells. Different purification methods such as His purification and FLAG purification will be used for the complex purification.

Cryo-EM analysis will be done in collaboration with Dr. Pfeffer's lab, which is important for pursuing high-resolution structures after obtaining good samples. After the structures are obtained, the corresponding bio-functional experiments for verification of the structural information are planned. *S. cerevisiae* will be chosen for performing the in vivo experiments due to the limited higher-level Biosafety in our laboratory. The structural and bio-functional results without any doubt will provide us with meaningful information towards the understanding of the MT nucleation mechanism in *C. albicans* and to compare the conservation and variation of MT nucleation mechanism among different organisms along the evolutionary timeline.

3 Results

All experiments and analyses in this part were performed by me if it is not stated or specified otherwise.

3.1 Structural insights into the core microtubule nucleation unit of γ-TuSC in *C. albicans*

This part work was published in Nature Communications in 2020 with me as a joint co-first author[3].

3.1.1 *C. albicans* γ-TuSC purification and its overall cryo-EM structure

A sample of *C. albicans* γ-TuSC was purified after expression of *TUB4*, *SPC97,* and *SPC98* in insect cells. The tetrameric γ-TuSC was purified by His purification (His tags at Spc97 and Spc98) and by anion-exchange chromatography (MonoQ). The purified γ-TuSC was used for cryo-EM analysis. Consistent with a previous study of purified *C. albicans*, the γ-TuSC forms a Y-shaped monomer after negative stain analysis. The cryo-EM data collection and analysis, and the 3D density model building were performed by Dr. Erik Zupa.

From the MonoQ chromatography and the SDS-Page gel staining, the peak fraction contained the γ-TuSC components (Fig. 11a). By analyzing the γ-TuSC structure by computational particle sorting, particle classification, and refinement, a global resolution of 3.6 Å was reached (Fig. 11b-d). The corresponding cryo-EM parameters of the γ-TuSC are summarized in Table 1.

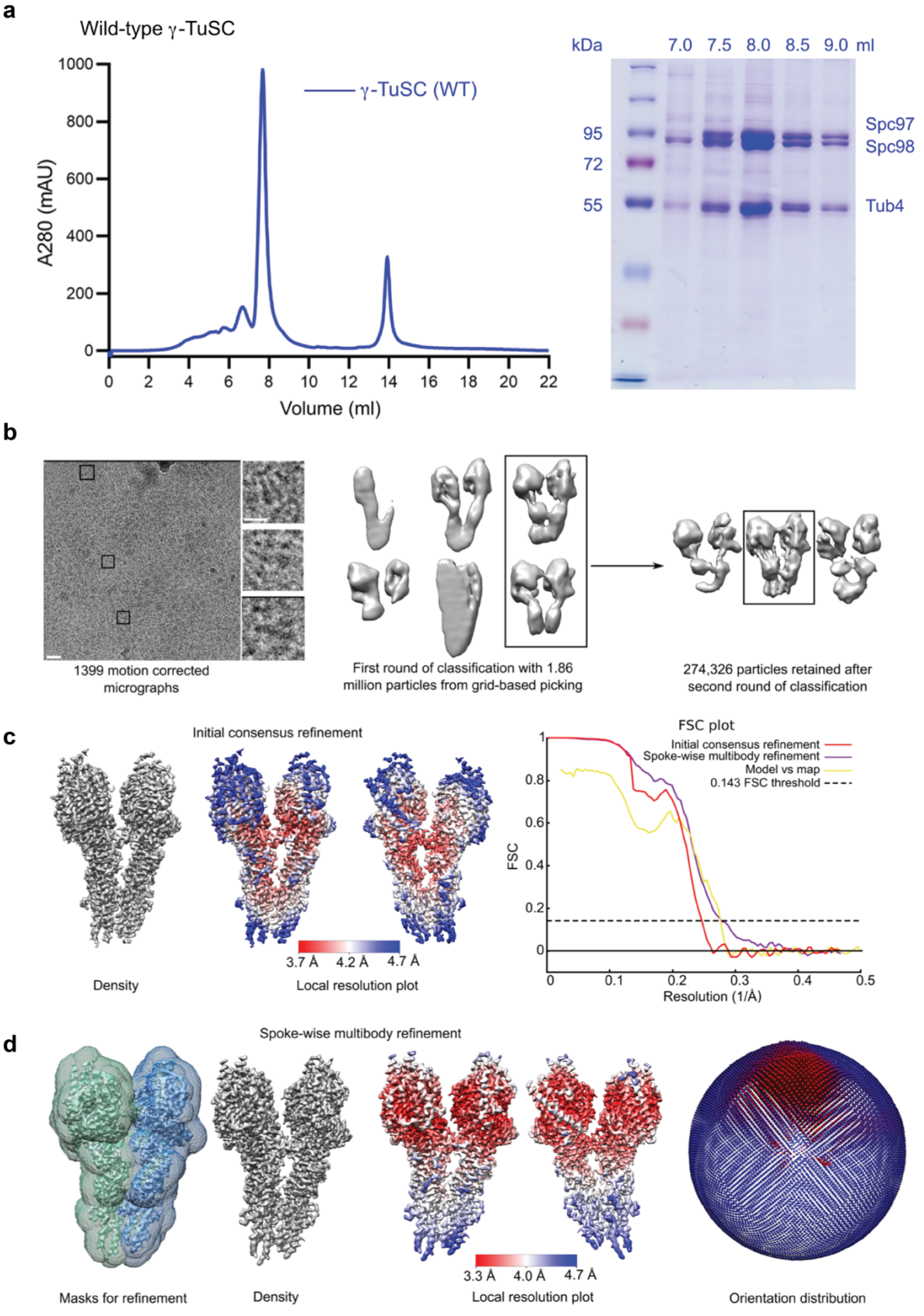
a
Wild-type γ-TuSC
γ-TuSC (WT)
A280 (mAU)
Volume (ml)
kDa
7.0 7.5 8.0 8.5 9.0 ml
95
72
55
Spc97
Spc98
Tub4
b
1399 motion corrected micrographs
First round of classification with 1.86 million particles from grid-based picking
274,326 particles retained after second round of classification
c
Initial consensus refinement
Density
3.7 Å 4.2 Å 4.7 Å
Local resolution plot
FSC plot
Initial consensus refinement
Spoke-wise multibody refinement
Model vs map
0.143 FSC threshold
FSC
Resolution (1/Å)
d
Spoke-wise multibody refinement
Masks for refinement
Density
3.3 Å 4.0 Å 4.7 Å
Local resolution plot
Orientation distribution

Figure 11: Cryo-EM flowchart of *C. albicans* γ-TuSC

(a) The Anion-exchange chromatography profile of wild-type γ-TuSC after Ni-NTA purification (Left); the Coomassie blue staining of the wild-type γ-TuSC peak fractions.

(b) The representative cryo-EM micrograph of γ-TuSC. 1,399 micrographs were used for analysis acquired in two imaging sessions on two different cryo-EM grids. Scale bar, 30 nm. Three selected particles are shown at higher magnification. Scale bar, 10 nm (Left). 1.86 million particles were extracted from the micrographs based on a regular grid with 10 nm spacing and computationally sorted via several consecutive steps of 3D classification. The initial round of 3D classification was performed on four subsets in parallel with the classes retained for further processing highlighted in a black box. In total, 274,326 particles were left after the second round of classification with the best one highlighted in a black box (Right).

(c) The initial refinement of the γ-TuSC particles produced a cryo-EM density (grey) at 4.1 Å global resolution. The local resolution plot (ranging from 3.7 to ~ 5 Å) illustrated that the best resolution was achieved between the two spokes. The local resolution plot is color-coded as indicated (Left). Mask-corrected Fourier shell correlation of the two independently refined reconstructions before (red) and after multibody refinement (purple). Fourier shell correlation of γ-TuSC between the full reconstruction and the atomic model. The FSC = 0.143 threshold is indicated by a dashed line (Right). Data points for all plotted FSC curves are included in the Source Data.

(d) The depicted masks comprising two spokes were used for the multibody refinement of γ-TuSC. The output density segments were combined into one composite density at 3.6 Å global resolution (Left). Local resolution is color-coded as indicated. The orientation distribution of particle views is shown (Right).

Data in panel (**a**) were produced by Anjun Zheng.

Data in panels (**b-d**) were produced by Dr. Erik Zupa. Figures were modified from Erik et al., 2020[3].

Table 1 Cryo-EM data collection, refinement, and validation statistics

***Candida albicans* γ-TuSC (EMD-11835) (PDB-7ANZ)**			
Data collection and processing	Dataset 1		Dataset 2
Magnification	81,000		81,000
Voltage (kV)	300		300
Electron exposure (e–/Å^2)	40		40
Defocus range (μm)	−2 to −3		−2 to −3
Pixel size (Å)	1.07		1.07
Initial particle images (no.)	309,744		1,502,064
Final particle images (no.)	45,351		228,975
Merged set of particles	274,326		–
Map resolution (Å)	3.6		–
FSC threshold	0.143		–
Model resolution range (Å)	3.3-4.7		–
Refinement			
Initial model used (PDB code)	Homology models derived from human GCP4 (3RIP) and γ-tubulin (1Z5W)		–
Model resolution (Å)	3.6	4.2	–
FSC threshold	0.143	0.5	–
Model resolution range (Å)	3.5-4.3		–
Map sharpening *B* factor (Å^2)	−60.0		–
Model composition			–
Non-hydrogen atoms	16,759		–
Protein residues	2041		–

***Candida albicans* γ-TuSC (EMD-11835) (PDB-7ANZ)**		
Ligands	0	–
B factors (Å^2)		–
Protein	5.71/82.31/35.50	–
Ligand	−/−/−	–
R.m.s. deviations		–
Bond lengths (Å)	0.003	–
Bond angles (°)	0.786	–
Validation		–
MolProbity score	1.66	–
Clashscore	4.57	–
Poor rotamers (%)	0.31	–
Ramachandran plot		–
Favored (%)	93.36	–
Allowed (%)	6.49	–
Disallowed (%)	0.15	–

The table was from Erik et al., 2020[3].

The monomeric structure of γ-TuSC is composed of Spc97/Spc87/γ-tubulin three components in a ratio of 1:1:2 with a height of 180 Å and length of 100 Å (Fig. 12a). The N-terminal GRIP1 domains from Spc97/98 subunits interact with each other by adopting a canonical interaction with α-helices arranged into bundles stabilized by the hydrophobic interactions (Fig. 12b), while the C-terminal GRIP2 domains of Spc97/98 subunits bind γ-tubulins. However, the N-terminal regions of 1-91 aa of Spc97 and 1-149 aa of Spc98 were unresolved due to loss in the cryo-EM density.

The overall conformation of *C. albicans* γ-tubulins in the cryo-EM density was confirmed by comparison to the curved and straight αβ-tubulin dimers (PDB 4FFB, PDB 5W3F) in focusing on the arrangement of α-helices α6 and α7 in β-tubulin, which can mostly reflect the variation of the curved or the straight conformations (Fig. 12c). With the inspection of the overlapped deviations among 'curved' β-tubulin (magenta), 'straight' β-tubulin (green), γ-tubulin associated with the cryo-EM density of Spc97 (Fig. 12c), and the cross-correlation parameters between density segments and R.M.S.D (root mean square deviation) of the backbone atoms in the atomic models (Table 2), the conformation of two γ-tubulins in our cryo-EM structure fit into a 'straight' conformation (Fig. 12c). In addition, the X-ray structure of GTP-binding β-tubulin (PDB 4FFB) was used for the two γ-tubulin density segments in our cryo-EM reconstruction, which revealed a GDP-bound γ-tubulin in our cryo-EM density (Fig. 12d).

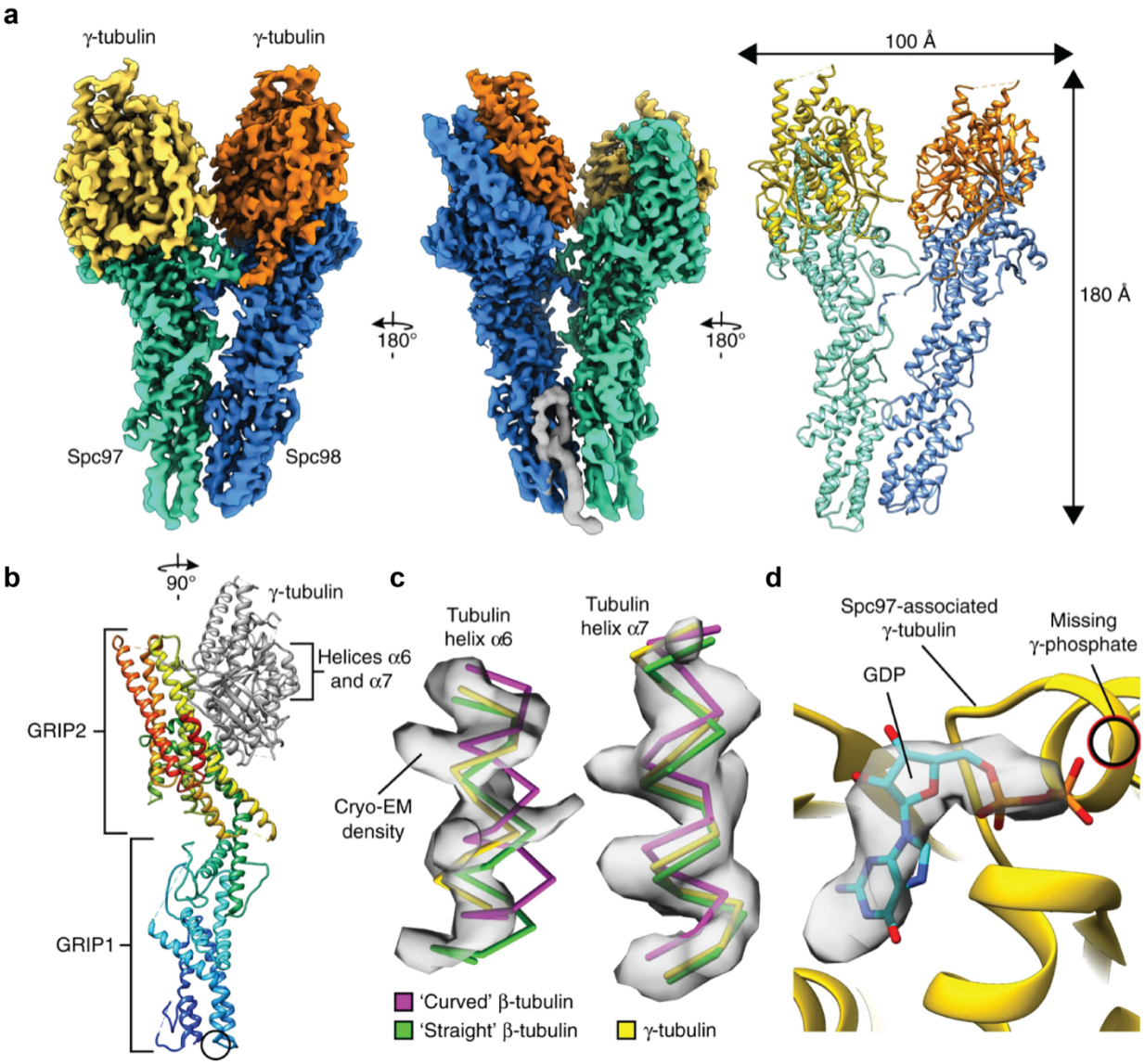

Figure 12: Cryo-EM structure of *C. albicans* γ-TuSC

(a) The Cryo-EM reconstructed γ-TuSC density from *C. albicans*. Segmented cryo-EM densities for Spc97 (green), Spc98 (blue), and γ-tubulins (yellow, orange) are shown. Unassigned density is depicted in gray (Left). The γ-TuSC atomic model. Dimensions of the complex are shown (Right).

(b) The Spc97-γ-tubulin heterodimer atomic model. The Spc97 model is colored blue (N-terminus) to red (C-terminus). The missing Spc97 N-terminus part is indicated in a black circle. The γ-tubulin model is shown in gray and α-helices α6 and α7 are annotated.

(c) Helices α6 and α7 of γ-tubulin (yellow), 'straight' β-tubulin (green), and 'curved' β-tubulin (magenta) superposed to the cryo-EM density of Spc97-associated γ-tubulin.

(d) Atomic model for GDP (cyan) superposed to cryo-EM density (gray) in the nucleotide-binding pocket of Spc97-associated γ-tubulin (yellow). The density does not indicate the presence of a γ-phosphate group. Missing γ-phosphate position as indicated by the circle (red/black).

Data in panels (**a-d**) were produced by Dr. Erik Zupa. Figures were modified from Zupa et al., 2020[3].

Table 2 Structural comparison between γ-tubulin and β-tubulin in two different conformations

	R.M.S.D. of C_α backbone atoms		Cross-correlation between density segments	
	β-tubulin curved	**β-tubulin straight**	**β-tubulin curved**	**β-tubulin straight**
γ-tubulin (Spc97) (Å)	2.128	1.302	0.7876	0.8309
γ-tubulin (Spc98) (Å)	1.635	1.167	0.7950	0.8349

The table was from Zupa et al., 2020[3].

3.1.2 Two heterodimeric spokes are formed by Spc97-γ-tubulin and the Spc98-γ-tubulin

Viewing the overall structure of *C. albicans* γ-TuSC, the structure can be illustrated as a heterodimer which is composed of two spokes of Spc97-γ-tubulin and the Spc98-γ-tubulin. The interfaces between γ-tubulins and Spc97/Spc98 are more tightly bound because the interactions in between are mainly contributed by electrostatic interactions (Fig. 13a). Additionally, the Spc97-Spc98 interaction interfaces are also important and are formed by two clusters. One cluster is the interaction interfaces between GRIP1 domains of Spc97 and Spc98 where the hydrophobic interactions are dominant, whereas the interfaces of GRIP1 domains of GCP2 and GCP3 are mainly electrostatic in humans even though they share similar interacting positions (Fig. 13b-d).

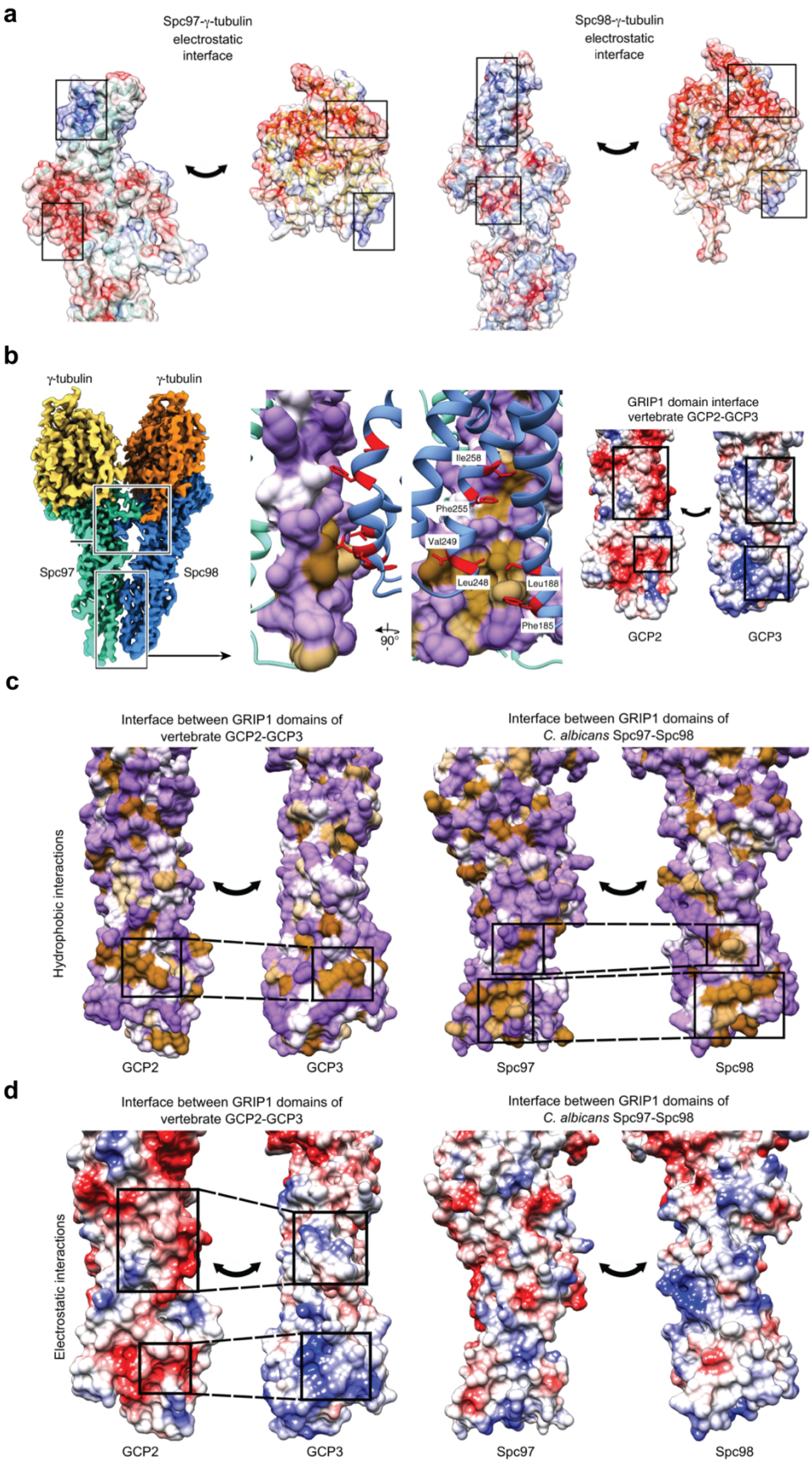
a
Spc97-γ-tubulin electrostatic interface
Spc98-γ-tubulin electrostatic interface
b
γ-tubulin
γ-tubulin
Spc97
Spc98
Ile258
Phe255
Val249
Leu248
Leu188
Phe185
90°
GRIP1 domain interface vertebrate GCP2-GCP3
GCP2
GCP3
c
Interface between GRIP1 domains of vertebrate GCP2-GCP3
Interface between GRIP1 domains of C. albicans Spc97-Spc98
Hydrophobic interactions
GCP2
GCP3
Spc97
Spc98
d
Interface between GRIP1 domains of vertebrate GCP2-GCP3
Interface between GRIP1 domains of C. albicans Spc97-Spc98
Electrostatic interactions
GCP2
GCP3
Spc97
Spc98

Figure 13: Molecular interactions among Spc97, Spc98, and γ-tubulin proteins
(a) The electrostatic interactions within the γ-TuSC between Spc97 and γ-tubulin (Left) and the Spc98 and γ-tubulin (Right), respectively. Surface representation of the atomic model, colored according to charges (red: negative, blue: positive, white: no charge).
(b) The interactions between the GRIP1 domains of Spc97 and Spc98. The Spc97 interface is represented as a surface, color-coded according to hydrophobicity (brown: hydrophobic; purple: hydrophilic). Spc98 is represented as a ribbon. Amino acid side chains mediating hydrophobic interactions are shown and depicted in red.
(c) The hydrophobic interactions of human GCP2-GCP3 GRIP1 domains (Left), and Spc97-Spc98 GRIP1 domains from *C. albicans* (Right). The models are shown in surface representation and color-coded according to hydrophobicity (brown: hydrophobic; purple: hydrophilic). Interacting hydrophobic patches are indicated in black boxes.
(d) The electrostatic interactions of human GCP2-GCP3 GRIP1 domains (Left), and Spc97-Spc98 GRIP1 domains from *C. albicans* (Right). The models are shown in surface representation and color-coded according to charges (red: negative, blue: positive, white: no charge). Interacting electrostatic patches are indicated in black boxes.
Data in panels (**a-d**) were produced by Dr. Erik Zupa. Figures were modified from Zupa et al., 2020[3].

The second cluster of Spc97/Spc98 interaction interfaces was not conserved in human GCP2/GCP3. Several short insertions in *C. albicans* Spc97 (Thr232-Asp272, Glu495-Pro502, Asn539-Ser566, and Ala686-Ile737) and Spc98 (Asn626-Leu656) are partially visible in our structure, moreover, the insertion loops between Spc97 and Spc98 found in *C. albicans* which are not conserved in human GCP2 and GCP3 (Fig. 14a,b). Among the solved segments, the long insertion loop (Asn626-Leu656) in the Spc98 GRIP2 domain exerts an important role in bridging the GRIP2 domains between Spc98 and Spc97, additionally, the insertion loop of Spc98 is stabilized by Spc97 GRIP2 domain (Val498-Tyr505) and γ-tubulin N-terminal region (Thr38-Tyr72) (Fig. 14a,b).

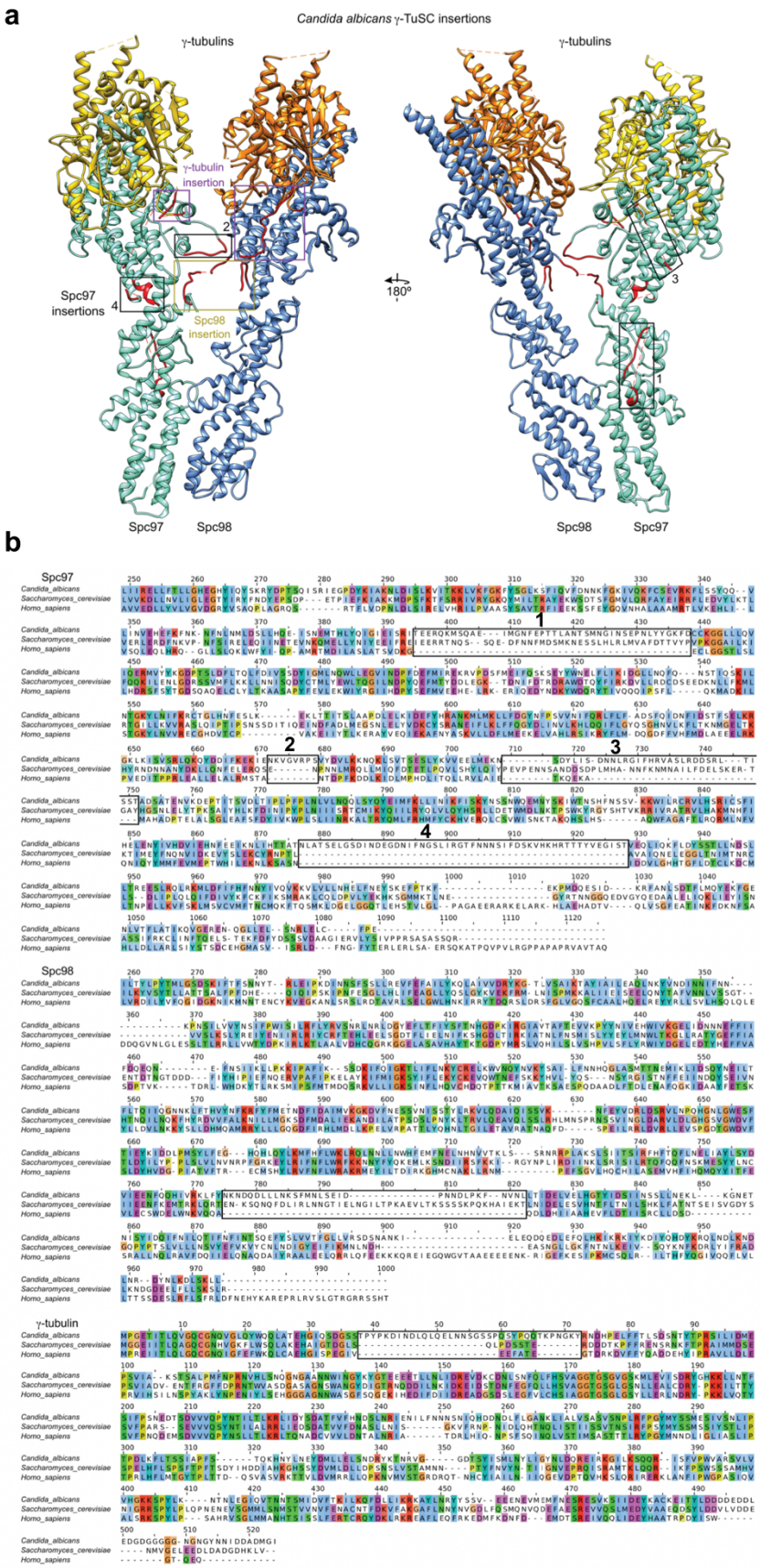
a
Candida albicans γ-TuSC insertions
γ-tubulins
γ-tubulins
γ-tubulin insertion
Spc97 insertions
Spc98 insertion
180°
Spc97
Spc98
Spc98
Spc97
b
Spc97
Spc98
γ-tubulin
Candida_albicans
Saccharomyces_cerevisiae
Homo_sapiens

Figure 14: The fungi-specific insertions modelled in *C. albicans* γ-TuSC subunits.
(a) The fungi-specific insertion loops (red) of Spc97 (black boxes with numbers), Spc98 (yellow-green box) and γ-tubulins (purple boxes) are shown in the full model. The insertion loops of Spc97 are numbered from N- to C-terminus.
(**b**) The sequence alignments corresponding to the insertion loops in *C. albicans* γ-TuSC are shown. In the Spc97 sequence alignment, the black boxes with numbers corresponded to the numbers 1-4 in (**a**). In the Spc98 sequence alignment, the insertion loop of *C. albicans* Spc98$^{Asn626\text{-}Leu656}$ is highlighted by a black box. In the γ-tubulin sequence alignment, the insertion of *C. albicans* γ-tubulin is highlighted by a black box.
Data in panels (**a and b**) were produced by Dr. Erik Zupa. Figures were modified from Zupa et al., 2020[3].

3.1.3 Spc98 insertion loop of Asn626-Leu656 is vital for the intact γ-TuSC structure and its function

To further investigate the function of the extended interfaces of γ-TuSC in *C. albicans*, the corresponding mutants of Spc98 (Spc98$^{\Delta D627\text{-}K650}$) and γ-tubulin (Tub4$^{\Delta T38\text{-}K71}$) and the other two wild-type γ-TuSC components (Spc97/γ-tubulin or Spc97/Spc98) were recombinantly co-expressed in insect cells. To better compare the overall structures of the mutated and wild-type γ-TuSCs, the isolation method of these two γ-TuSC mutants was the same as that used for the wild-type complex (His purification, MonoQ) (Fig. 15a). The peak fraction samples from the MonoQ chromatograms were freshly used for the negative staining EM analysis (Dr. Annett Neuner). With the negative stain EM data and 2D averaging analysis of these two mutants, these two mutants of Spc98$^{\Delta D627\text{-}K650}$ and Tub4$^{\Delta T38\text{-}K71}$ complexes showed the phenotype of wider (straddled) Y-shape structures with percentages of 28% for Tub4$^{\Delta T38\text{-}K71}$ mutant complex and 51% for Spc98$^{\Delta D627\text{-}K650}$ mutant complex (Fig. 15b). These data suggest that the extended interface formed by the Spc98 insertion loop is more central for stabilizing the overall structure of *C. albicans* γ-TuSC by providing a large interaction interface area with Spc97 GRIP2 domain and γ-tubulins, which may also contribute to the activation of the oligomeric γ-TuSC *in vivo*.

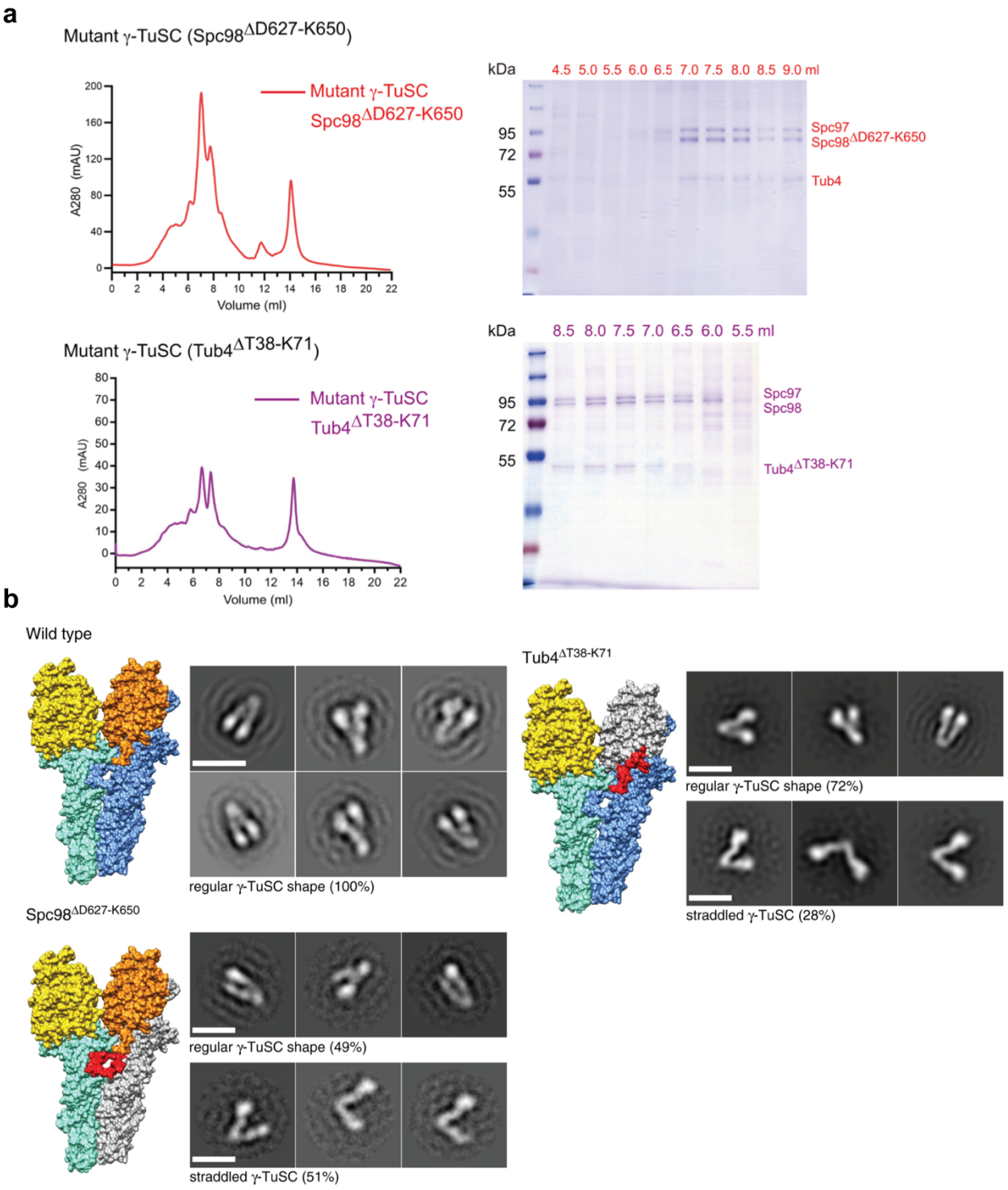

Figure 15: Purification of *C. albicans* γ-TuSC mutants with deleted insertions on Spc98 and γ-tubulin

(a) The Anion-exchange chromatography profiles of Spc98$^{D627\text{-}K650}$ or Tub4$^{T38\text{-}K71}$

contained γ-TuSC mutants after Ni-NTA purification (Left); the Coomassie blue staining of the peak fractions from two γ-TuSC mutants (Right).
(b) The negative stain analysis of the wild-type γ-TuSC, Spc98$^{\Delta D627\text{-}K650}$, and Tub4$^{\Delta T38\text{-}K71}$ contained mutant γ-TuSCs. Representative 2D classes from different particle subsets are shown in percentages. 11,901 particles were used for the Spc98$^{\Delta D627\text{-}K650}$ γ-TuSC mutant analysis and 15450 particles were used for the Tub4$^{\Delta T38\text{-}K71}$ γ-TuSC mutant analysis. Scale bars, 20 nm. The deleted mutants and the corresponding regions of D627-K650 on Spc98 and T38-K71 on γ-tubulin were marked in red colors.
Data in panel (**a**) were produced by Anjun Zheng.
Data in panel (**b**) were produced by Dr. Erik Zupa. Figures were modified from Zupa et al., 2020[3].

To test the hypothesis that Spc98$^{D627\text{-}K650}$ and Tub4$^{T38\text{-}K71}$ are important *in vivo*, amino acid sequences of *C. albicans* Spc98 and γ-tubulin were aligned with the amino acid sequences of *S. cerevisiae* Spc98 and γ-tubulin Tub4. It turned out that only the Spc98$^{D627\text{-}K650}$, which is the insertion domain in Spc98, has a homologous sequence in *S. cerevisiae* Spc98 (Fig. 14b), which could also be reflected by the cryo-EM structure of the *S. cerevisiae* γ-TuSC[185]. Thus, to verify the function of the insertion loop of *S. cerevisiae* Spc98 *in vivo*, the plasmid of pRS315-*spc98*$^{\Delta K674\text{-}H713}$ was transformed into *S. cerevisiae* (*spc98*Δ pRS316-*SPC98*) cells and tested on 5-FOA plates under temperatures of 23°C, 30°C and 37°C. Cells were comparably less fit at 37°C, indicating a conditional lethal growth defect (Fig. 16a). Then, *S. cerevisiae spc98*$^{\Delta K674\text{-}H713}$ cells expressing yeGFP-fused α-tubulin (*TUB1-yeGFP*; MT marker) and mCherry-fused Spc42 (*SPC42-mCherry*; a SPB marker) showed defective mitotic spindles after 3 h incubation at 37°C by tracing and analyzing the fluorescence signals from *TUB1-yeGFP* and *SPC42-mCherry*.
spc98$^{\Delta K674\text{-}H713}$ cells showed defective mitosis featuring monopolar, multi-polar, or defective bipolar spindles. In addition, extended long cytoplasmic MTs compared to *SPC98* control cells were observed (Fig. 16b).

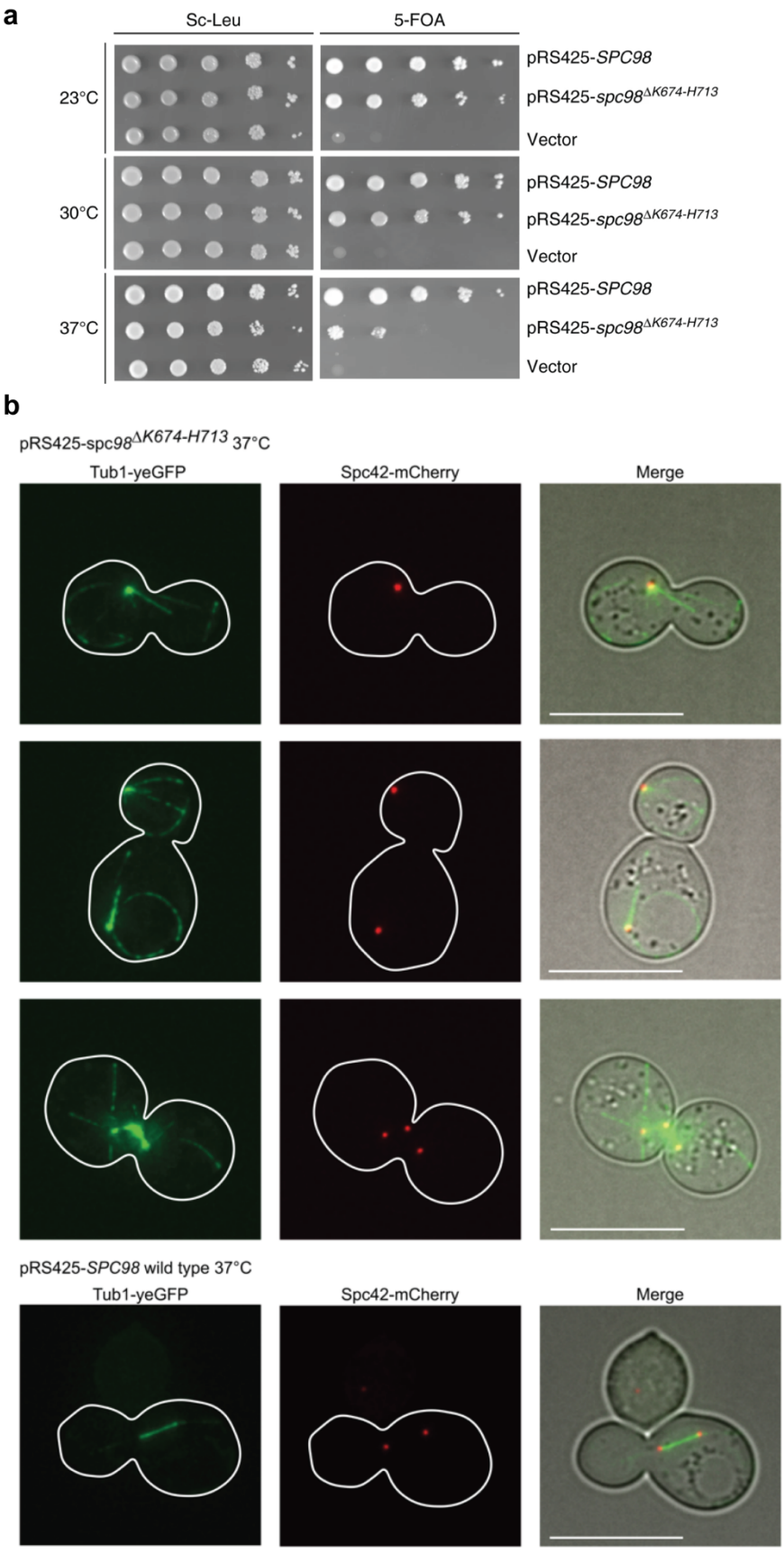
a
Sc-Leu
5-FOA
23°C
30°C
37°C
pRS425-SPC98
pRS425-spc98ΔK674-H713
Vector
b
pRS425-spc98ΔK674-H713 37°C
Tub1-yeGFP
Spc42-mCherry
Merge
pRS425-SPC98 wild type 37°C

Figure 16: Spc98 insertion loop is important for γ-TuSC function and stability *in vivo*

(a) The viability of *S. cerevisiae spc98*$^{\Delta K674\text{-}H713}$ cells. Plasmids (pRS425) containing wild type *SPC98*, *spc98*$^{\Delta K674\text{-}H713}$, or empty vector were separately transformed into *S. cerevisiae* strain ESM243-1 (*MATa Δspc98::HIS3* pRS316-*SPC98*). Serial dilutions of transformants were tested for growth efficiency at the indicated temperatures on SC-Leu and 5-FOA plates for 2–3 days. All cells grew equally well on SC-Leu plates because of the presence of pRS316-*SPC98*. Plates containing 5-FOA only allow the growth of cells that lost the URA3-based plasmid pRS316-*SPC98*. Cells with the empty pRS425 plasmid did not grow on 5-FOA at all temperatures because *SPC98* is an essential gene and therefore loss of pRS316-*SPC98* is lethal. The phenotype of conditional lethal of *spc98*$^{\Delta K674\text{-}H713}$ cells became apparent at 37 °C. The experiment was repeated three times with the same outcome.

(b) Cells of *spc98*$^{\Delta K674\text{-}H713}$ (upper) or *SPC98* (downside) expressing *TUB1-yeGFP* (green) and *SPC42-mCherry* (red) were cultured at 37°C for 3 hours. The *TUB1-yeGFP* (green) and *SPC42-mCherry* (red) fluorescent signals and the merged signals with phase contrast are shown. Scale bars, 10 μm. The experiments were repeated two times with the same outcome.

Data in panels (**a and b**) were produced by Anjun Zheng. Figures were modified from Zupa et al., 2020[3].

3.1.4 The Spc98 insertion loop is not conserved in GCP3 of higher eukaryotes

To figure out whether the insertion loop of *C. albicans* Spc98 is conserved across different species, especially in higher vertebrates such as *Homo sapiens*, the Spc97/GCP2-γ-tubulin and the Spc98/GCP3-γ-tubulin heterodimer structures in *C. albicans* and humans were compared. Due to the lack of the insertion loop in GCP3, the interface between GCP2/3 is extended by direct electrostatic interactions between the charged patches on the γ-tubulin molecules in humans (Fig. 17a, Right). Correspondingly, to explore whether the electrostatic interactions between the neighboring γ-tubulin molecules in human γ-TuSC are conserved or not, a wide range of organisms were used to compare the sequences of Spc98/GCP3 and γ-tubulin. The sequence alignment results show that the

electrostatic interactions between γ-tubulin molecules were conserved besides the organisms that possess the Spc98/GCP3 insertion loop (Fig. 17b,c). This finding indicates that the electrostatic interaction between γ-tubulins of neighboring spokes in human γ-TuSC might replace the function of the insertion loop of Spc98/GCP3 in *C. albicans* γ-TuSC to stabilize the γ-TuSC structure in different species.

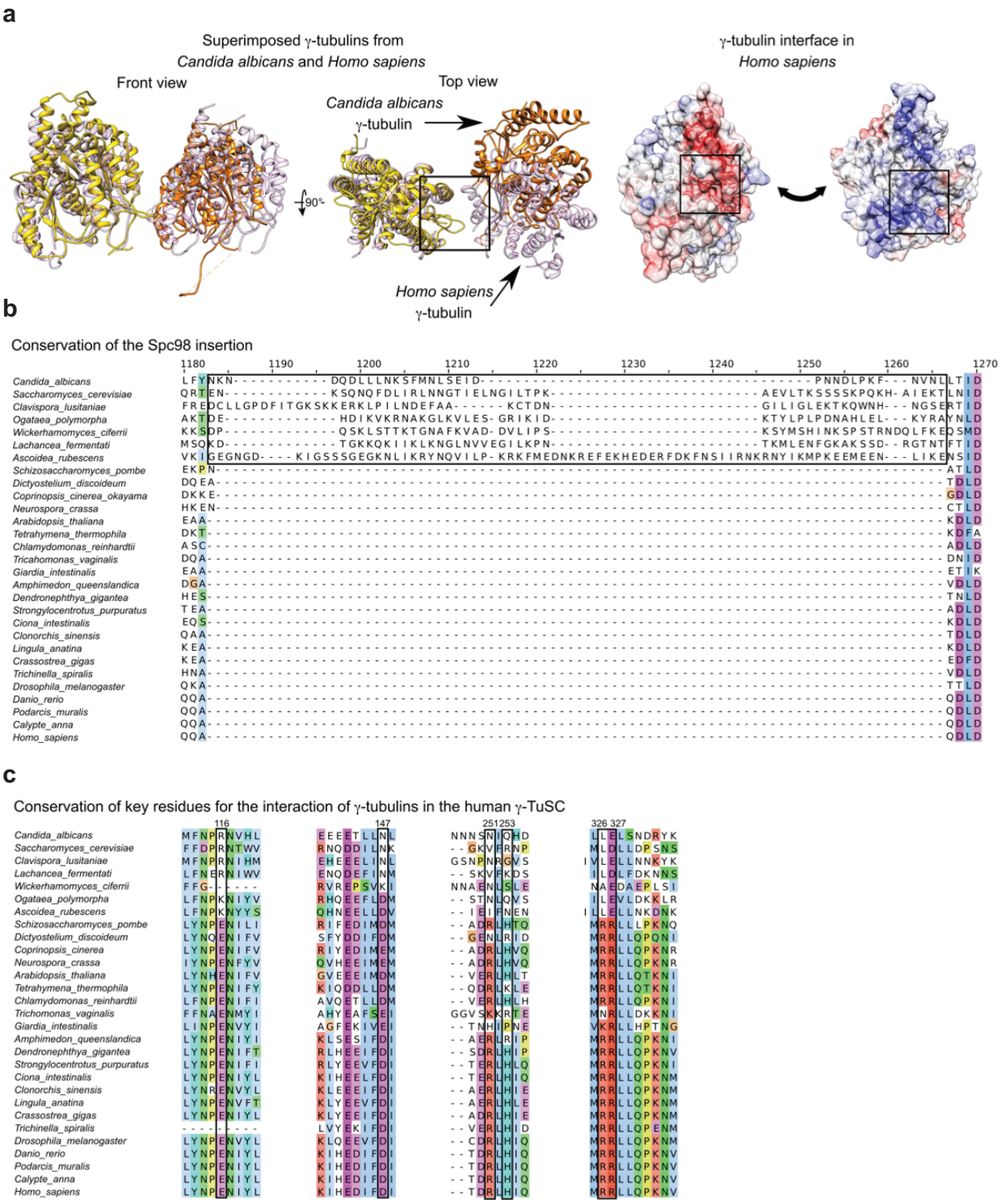

Figure 17: The fungi-specific Spc98 insertion may substitute the function of the neighboring γ-tubulin interaction during evolution

(a) Superposed atomic models for the two γ-tubulin molecules from the γ-TuSC units of

C. albicans (yellow, orange) and human (pink). The γ-tubulin interaction area in the human γ-TuSC is indicated by black boxes (left). In the human γ-TuSC, electrostatic interactions mediate the interactions of the two γ-tubulin molecules (right). Surface representation of the atomic model, colored according to charge (red: negative, blue: positive, white: no charge).

(b) Spc98/GCP3 sequences from a range of organisms were aligned with the region of Spc98 loop insertion highlighted in the black box. Numbering is produced according to the sequence alignment.

(c) γ-tubulin sequences were aligned from the organisms the same as in (**b**) and the amino acids (black boxes) essential for the electrostatic interaction of γ-tubulins in the human γ-TuSC are shown.

Data in panels (**a-c**) were produced by Dr. Erik Zupa. Figures were modified from Zupa et al., 2020[3].

3.1.5 Conformational rearrangement is required for the activation of γ-TuSC oligomer in *C. albicans*

After comparing the Spc98 insertion loop and the electrostatic interactions of γ-tubulins between *C. albicans* and human γ-TuSCs at the amino acid sequence level, we analyzed the structural differences among Spc/GCP paralogues, Spc/GCP-γ-tubulin complexes, and their conformational plasticity in *C. albicans*, *S. cerevisiae*, and humans. γ-TuSC structures were superposed based on the positions of Spc97 and GCP2. The comparison revealed that the displacement of GRIP domains and γ-tubulins was indicated by the R.M.S.D. values of their protein backbone atoms (Table 3). The R.M.S.D. values and the overall structural alignment (Fig. 18a) of the γ-TuSCs *between C. albicans* and *S. cerevisiae* indicate that the dominant conformational rearrangements of GRIP domains occur at the interaction loop on the Spc98 GRIP2 domain and the associated γ-tubulin molecule. This suggests that the conformational transformation into an active MT nucleation template from the ‘open’ to ‘close’ state is mainly triggered by the rearrangement of Spc98 and the associated γ-tubulin molecule (Fig. 18a). The two γ-tubulin molecules within the γ-TuSC need to move 5 Å closer to each other to form the MT nucleation competent ‘closed state’ of the γ-TuSC oligomer.

In contrast, the comparison of the 14-spoked human γ-TuRC helix with the *S. cerevisiae* γ-TuSC oligomer in the 'closed' conformation (Fig. 18b) indicated the overall similar conformation between the two complexes. However, the vertebrate γ-tubulin molecules need to move 2.5 Å further apart to perfectly reflect MT symmetry which is different from the oligomerized *C. albicans* γ-TuSC. This less pronounced arrangement of GCP2/GCP3-γ-tubulin subunits in the human γ-TuSC (2.5 Å versus 5 Å) might be attributed to the asymmetric structure of the γ-TuRC, which originates from the incorporation of GCP4-6 into the complex (Table 4)[2, 186].

Table 3 R.M.S.D. of Cα backbone atoms between γ-TuSC segments in different species

	***Homo sapiens* to *S. cerevisiae* in 'closed' state**	***C. albicans* to *S. cerevisiae* in 'closed' state**	***C. albicans* to *S. cerevisiae* in 'open' state**
Spc97 GRIP1 (Å)	4.088	3.262	2.661
Spc97 GRIP2 (Å)	2.447	1.483	2.716
Spc98 GRIP1 (Å)	7.310	5.579	5.872
Spc98 GRIP2 (Å)	7.784	13.692	7.234
Spc97 γ-tubulin (Å)	2.934	1.432	3.728
Spc98 γ-tubulin (Å)	7.199	18.591	4.490

The table was taken from Zupa et al., 2020[3].

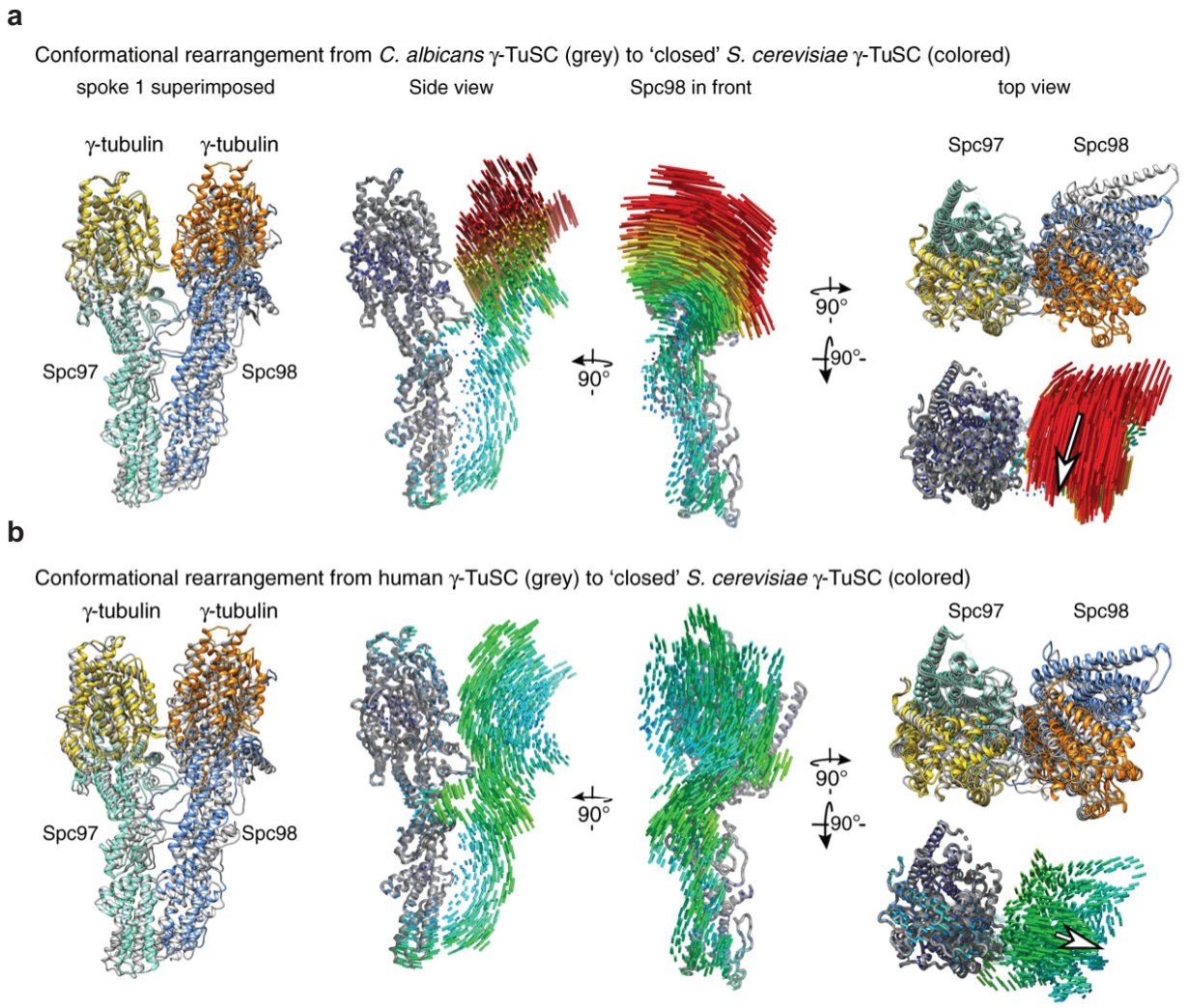

Figure 18: Conformational rearrangement is required from monomer to oligomer formation in *C. albicans* γ-TuSC

(a) *C. albicans* γ-TuSC atomic model was superposed to the *S. cerevisiae* γ-TuSC in the closed conformation (colored) with Spc97-γ-tubulin as fix points.

(b) *C. albicans* γ-TuSC atomic model was superposed to the *human* γ-TuSC in the closed conformation (colored) referenced to *S. cerevisiae* Spc97/GCP2-γ-tubulin.

(a,b) The displacement of domains was visualized by trajectories linking the backbone atoms in the two superposed models. For orientation, atomic models for the first spoke are superposed to trajectories. Trajectories are color-coded from low (blue) to high (red) motion. In the 'top view', arrows representing the average direction and magnitude of γ-tubulin displacement are superposed to the trajectories.

Data in panels (**a and b**) were produced by Dr. Erik Zupa. Figures were modified from Zupa et al., 2020[3].

Table 4 Amino acid sequence identifiers of GCP subunits in various species

Organism	Phylum	GCP2	GCP3	GCP4	GCP5	GCP6
Giardia Intestinalis	*Metamonada*	A8BD62	A8BFK8	KAE8304190.1	ESU36978.1	A8BUR1
Trichomonas vaginalis	*Metamonada*	A2E313	A2E3S1	XP_001325680.1	XP_001323803.1	>XP_001328726.1
Angomonas deanei	*Euglenozoa*	EPY32211.1	EPY37939.1	EPY31448.1	EPY34001.1	EPY30063.1
Tetrahymena thermophila	*Alveolates*	Q23AE3	Q22ZA9	XP_001025759.3	XP_001014477.2	XP_001015474.3
Phytophthora infestans	*Stramenopiles*	KAF4031510.1	KAF4046598.1	KAF4031595.1	KAF4137761.1	KAF4030965.1
Gracilariopsis chorda	*Rhodophyta*	PXF41098.1	PXF45651.1	PXF41306.1	-	PXF43115.1
Chlamydomonas reinhardtii	*Chlorophyta*	A8J5J8	A8JBY6	XP_001689495.1	XP_001699475.1	PNW77310.1
Arabidopsis thaliana	*Spermatophyta*	Q9C5H9	Q9FG37	NP_190944.2	NP_565235.3	NP_189947.2
Candida albicans	*Ascomycota*	Q59PZ2	A0A1D8PS42	-	-	-
Saccharomyces cerevisiae	*Ascomycota*	P38863	P53540	-	-	-
Homo sapiens	*Chordata*	Q9BSJ2	Q96CW5	Q9UGJ1	Q96RT8	Q96RT7

The table was modified based on Zupa et al., 2020[3].

In conclusion, the His purified *C. albicans* γ-TuSC and its high-resolution structure enabled us to compare the structural deviations among different species of *S. cerevisiae*

and human, the insertion loops in *C. albicans* γ-TuSC, especially for Spc98 and Tub4 insertion loops found in *C. albicans* γ-TuSC provide evidence of the MT nucleation template (γ-TuSC in *S. cerevisiae* and *C. albicans*; γ-TuRC in human) variations during the evolution between the lower and higher eukaryote species. Moreover, the structural information also enabled me to perform the in vitro mutation experiment to analyze architecture changes after deleting the insertion loops in *C. albicans* Spc98 and γ-Tubulin. More importantly, the in vivo mutation experiment and analysis further proved the importance of the Spc98 insertion loop in living cells. All in all, with the combination of the structural analysis, the biochemical, and bio-functional analysis, I have illustrated the basic MT nucleation unit in *C. albicans* which is a 'Y'-shaped monomer at the atomic level and distinguished several insertion loops that are important for the γ-TuSC stability at the molecular level and the importance of the insertion loop on Spc98 for the cell viability at the cellular level.

3.2 The structural insight of MT nucleation template of γ-TuRC at the cytoplasmic side in *C. albicans*

This part work is under revision in the Journal of Nature Communications with me as the joint first author.

3.2.1 The reconstitution of *C. albicans* cytoplasmic MT nucleation unit in insect cells

Our previous study of *C. albicans* γ-TuSC indicated a 'monomeric γ-TuSC' with the insertion loop on Spc98 as a stabilizer. To better understand MT nucleation in *C. albicans* at the structural and molecular level, the oligomerisation promoter of the receptor protein Spc72[149], the polymerase protein Stu2 (Stu2 was found to be recruited by Spc72 and to localize at the cytoplasmic side of SPB)[167] and the Mzt1 protein as an additional interaction partner of *C. albicans* γ-TuSC (Mzt1 is absent in *S. cerevisiae*) were included and studied in this part. The previous study shows that Mzt1 and the receptor proteins of Spc110 and Spc72 can promote the oligomerization of the γ-TuSC into the higher oligomers in *C. albicans*[133]. Moreover, Mzt1 was shown to be involved in the recruitment

of γ-TuSC to SPB [135, 187]. How Mzt1 fulfills these functions is still enigmatic. Thus, by using the MultiBac^{TM} system, γ-TuSC together with Spc72, Stu2, or Mzt1 were co-expressed in insect cells and tested for complex formation and oligomerization. Pull-down experiments showed no direct interaction between Mzt1 and Stu2 (Fig. 19b), thus, the Mzt1 and Stu2 were not constructed and co-expressed together in our study.

Surprisingly, when combining γ-TuSC components (Spc97, Spc98, γ-tubulin) with a C-terminally truncated version of the receptor protein of Spc72$^{1-599}$ which is lacking the SPB-binding domain (Fig. 19a) and a FLAG-tagged, full-length version of the MT polymerase Stu2, the FLAG-Stu2 purified products contained all γ-TuSC components, Spc72$^{1-599}$ and Stu2, as judged by Coomassie blue staining (Fig. 19c and Fig. 23a). Additionally, the negative stain EM analysis of the FLAG-Stu2 elute showed a nice distribution of ring structures formed under the TBS buffer condition (150 mM NaCl). In contrast, the wild-type γ-TuSC oligomers were not observed with higher salt concentrations in the presence of Spc110 in previous studies (Fig. 19d)[133, 141].

The reason for using the truncated version of Spc72 (Spc72$^{1-599}$) was that the truncated version of Spc72 (Spc72$^{1-599}$) was enough for Stu2 binding, which was confirmed by pull-down experiments. Moreover, there is no binding of Stu2 and the more C-terminal truncated Spc72 (Spc72$^{600-762}$) (Fig. 19b). Besides, with the amino acid sequence alignment (Fig. 19a), Spc72$^{1-599}$ covered the region (CM1 motif) corresponding to the truncated mutant of Spc110$^{1-220}$ used in the previous study of γ-TuSC oligomer formation in *S. cerevisiae*[137, 141].

Thus, the truncated mutant of Spc72$^{1-599}$ was used for the co-expression experiment in this study. Additionally, to make the writing easier, Spc72 represents Spc72$^{1-599}$ in our insect cell co-expression experiment if not specified particularly. To investigate the oligomeric state of the reconstituted complexes, SEC (size exclusion chromatography), Coomassie blue staining, and negative stain EM were used for the single particle analysis. The oligomeric peak of the γ-TuSC/Spc72$^{1-599}$/FLAG-Stu2 complex in HB100 buffer (100 mM KCl, low salt) from the SEC profile was analyzed (Fig. 19e) and the oligomeric ring-like particles were observed from the peak fraction sample by the negative stain EM (Fig. 19f).

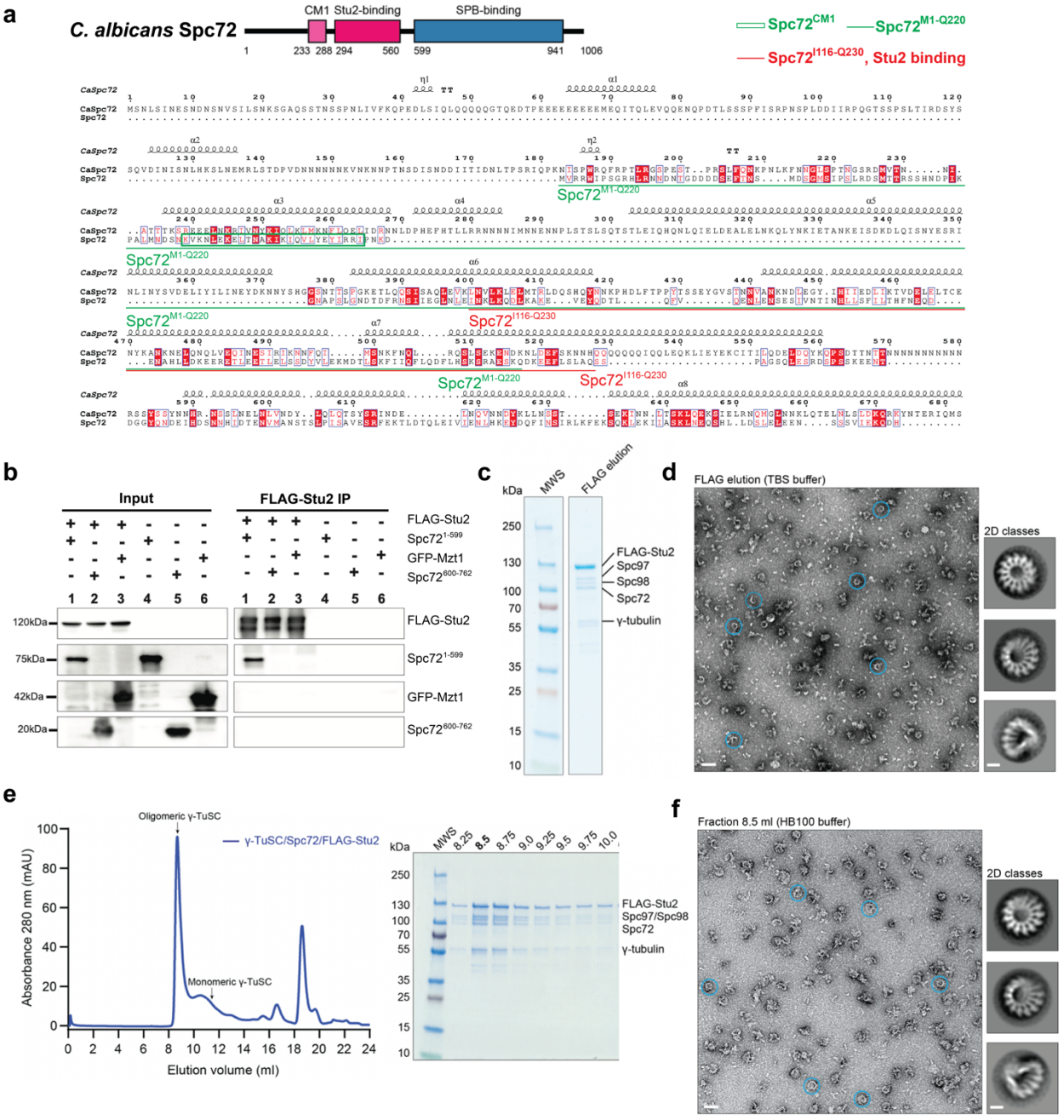

Figure 19: The reconstitution and FLAG purification of γ-TuSC/Spc72$^{1-599}$/FLAG-Stu2 complex from *C. albicans*

(a) The functional domains of Spc72 are marked by different colors (1-233, black: disordered N-termini; 233-288, hot pink: CM1 motif; 294-560, deep pink, Stu2 binding; 599-941, steel blue, SPB binding). Sequence alignment of Spc110 and Spc72 from *S. cerevisiae* and *C. albicans,* two species with CM1 motifs and Stu2 binding regions that are highlighted in green and red colors. The predicted 3D model of *C. albicans* Spc72

(AF-Q5AGV5-F1) downloaded from the AlphaFold Protein Structure Database (https://www.alphafold.ebi.ac.uk) was used for showing the secondary structural helixes (mainly the α helixes, above the aligned amino acid sequence) together with the primary sequences (produced by uploading the predicted protein structure and the amino acid sequence alignment result onto the website of Espript 3.0 (https://espript.ibcp.fr/ESPript/ESPript/)). Spc72^{CM1} (green rectangle), Spc72$^{M1-Q2220}$ (green line), and the Stu2 binding region of Spc72$^{I116-Q230}$ (red line) in *S. cerevisiae* were highlighted in the primary sequence alignment scheme.

(b) The FLAG-Stu2 pull-down result of Stu2, Spc72$^{1-599}$, Spc72$^{600-762}$ and GFP-Mzt1.

(c) The Coomassie blue staining of the FLAG-Stu2 purified product from the complex of γ-TuSC/Spc72$^{1-599}$/FLAG-Stu2 expressed in insect cells. The five components of Spc97, Spc98, γ-tubulin, Spc72, and Stu2 are pointed out with black lines. kDa, kilodalton unit. MWS, molecular weight.

(d) The representative negative stain micrograph of the FLAG-Stu2 purified sample from the γ-TuSC/Spc72$^{1-599}$/FLAG-Stu2 elution. Several different orientated ring-like particles are marked in deep sky-blue circles. Scale bar, 50 nm. 2D classes after 2D class averaging analysis in RELION[190] on the right side are shown. Scale bar, 10 nm.

(e) SEC chromatography profile of γ-TuSC/Spc72$^{1-599}$/FLAG-Stu2 purified from FLAG Stu2 method. The two representative peaks formed from the oligomeric γ-TuSC and monomeric γ-TuSC are marked with arrows. The fractions ranging from 8.25 ml to 10.0 ml were analyzed by SDS-Page gel and Coomassie blue staining with the marked components. kDa, kilodalton unit. MWS, molecular weight.

(f) The representative negative stain EM micrograph of the SEC peak fraction sample of the γ-TuSC/Spc72$^{1-599}$/FLAG-Stu2 complex. Several ring-like particles, oriented in different directions, are marked with deep sky-blue circles. Scale bar, 50 nm. 2D classes after 2D class averaging analysis in RELION[190] on the right side are shown. Scale bar, 10 nm.

Data in panels (**a-c, e**) were produced by Anjun Zheng.

Data in panels (**d and f**) with the micrographs from negative stain EM were provided by Dr. Annett Neuner, and the 2D class averaging micrographs were produced by Anjun Zheng.

The co-expressed complex of γ-TuSC components (Spc97, Spc98, and γ-tubulin) with GFP-Mzt1 and Spc72$^{1-599}$ was then purified through FLAG-Spc97 (Fig. 20a). However, even the Coomassie blue staining and Western-blotting results from both of the peak fractions of the SEC showed GFP-Mzt1 was pulled-down (Fig. 20b,c), the negative stain EM analysis (Fig. 20d) indicated no obvious positive impact on the γ-TuSC ring formation by the addition of Mzt1. Due to the low particle number and low resolution obtained from negative stain EM analysis, it was difficult to judge whether Mzt1 was bound to the γ-TuSC ring or not. Interestingly, the 3D class averaging analysis and 3D alignment of the ring oligomers formed by γ-TuSC/Spc72$^{1-599}$/GFP-Mzt1 and γ-TuSC/Spc72$^{1-599}$/FLAG-Stu2 showed no obvious difference on the structural level (Fig. 20e). Thus, we decided to focus on the complex of γ-TuSC/Spc72$^{1-599}$/FLAG-Stu2 which has higher particle numbers and better sample homogeneity.

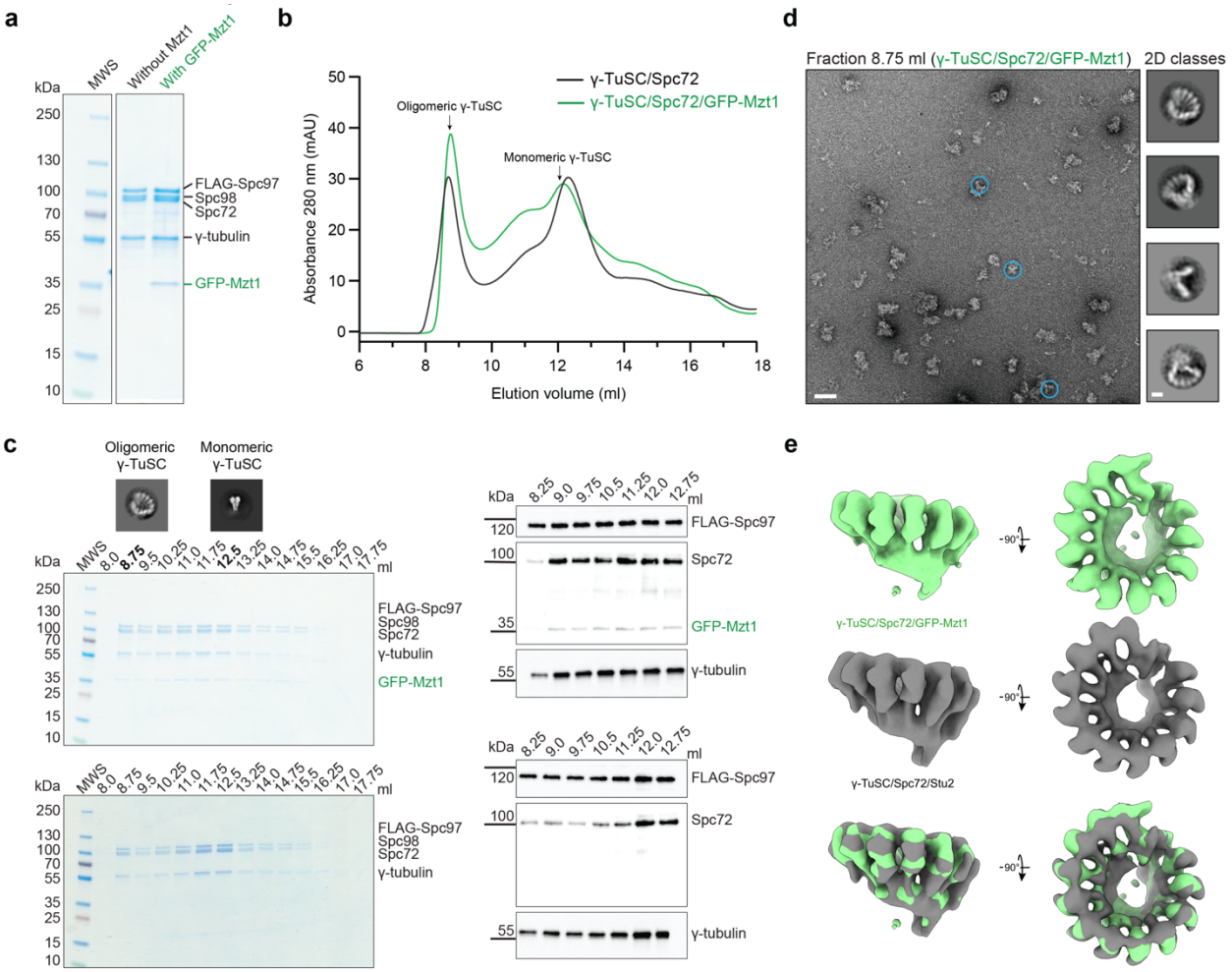

Figure 20: Mzt1 has no positive impact on the *C. albicans* γ-TuSC oligomer formation

(a) The Coomassie blue staining of the FLAG-Stu2 purified products from the complexes of γ-TuSC$^{FLAG\text{-}Spc97}$/Spc72$^{1\text{-}599}$ and γ-TuSC$^{FLAG\text{-}Spc97}$/Spc72$^{1\text{-}599}$/GFP-Mzt1 expressed in insect cells. The components of Spc97, Spc98, γ-tubulin, Spc72, and GFP-Mzt1 are labeled on the side of the gel. kDa, kilodalton unit; MWS, molecular weight.

(b) The SEC chromatography profiles of γ-TuSC$^{FLAG\text{-}Spc97}$/Spc72$^{1\text{-}599}$ (black line) complex and γ-TuSC$^{FLAG\text{-}Spc97}$/Spc72$^{1\text{-}599}$/GFP-Mzt1 (green line) complex purified via FLAG-Spc97. The peaks formed from the oligomeric γ-TuSC and monomeric γ-TuSC are marked with arrows.

(c) The fractions ranging from 8.0 ml to 17.75 ml from the SEC experiment in (**b**) were checked by SDS-PAGE and Coomassie blue staining. kDa, kilodalton unit; MWS, molecular weight. The fractions ranging from 8.25 ml to 12.75 ml from the SEC experiment in (**b**) were further analyzed by Western blotting with FLAG-Spc97, His tagged Spc72 and GFP-Mzt1, and γ-tubulin developed by the corresponding antibodies of anti-FLAG, anti-His and anti-γ-tubulin (home-made). kDa, kilodalton unit; MWS, molecular weight.

(d) The representative negative stain micrograph of the FLAG-Spc97 purified sample from the γ-TuSC/Spc72$^{1\text{-}599}$/FLAG-Stu2 SEC sample (fraction volume of 8.75 ml). Several different orientated ring-like particles are marked in deep sky-blue circles. Scale bar, 50 nm. 2D classes after 2D class averaging analysis in RELION[190] on the right side are shown. Scale bar, 10 nm.

(e) The alignment of the 3D class structures obtained from the 3D class averaging analysis of the negative stain samples of γ-TuSC$^{FLAG\text{-}Spc97}$/Spc72/GFP-Mzt1 (green) and γ-TuSC /Spc72/FLAG-Stu2 (grey) in different orientations. The overlapped structures in the third row are indicated by the grey/green color.

Data in panels (**a-d**) were produced by Anjun Zheng.

Data in panel (**e**) were produced by Bram J.A. Vermeulen.

3.2.2 The *C. albicans* cytoplasmic nucleation unit is conformationally primed for MT nucleation

With the information obtained from the negative stain result (Fig. 19d,f), the FLAG-Stu2 purified γ-TuSC/Spc72/Stu2 sample was used for the cryo-EM single particle analysis (Fig. 23a). The reconstituted γ-TuSC complex from the oligomeric complex shows different resolutions and the Fourier shell correlation (FSC) values also reflect the resolutions of the γ-TuSCs and the oligomeric γ-TuSC complexes (Fig. 21b,c).

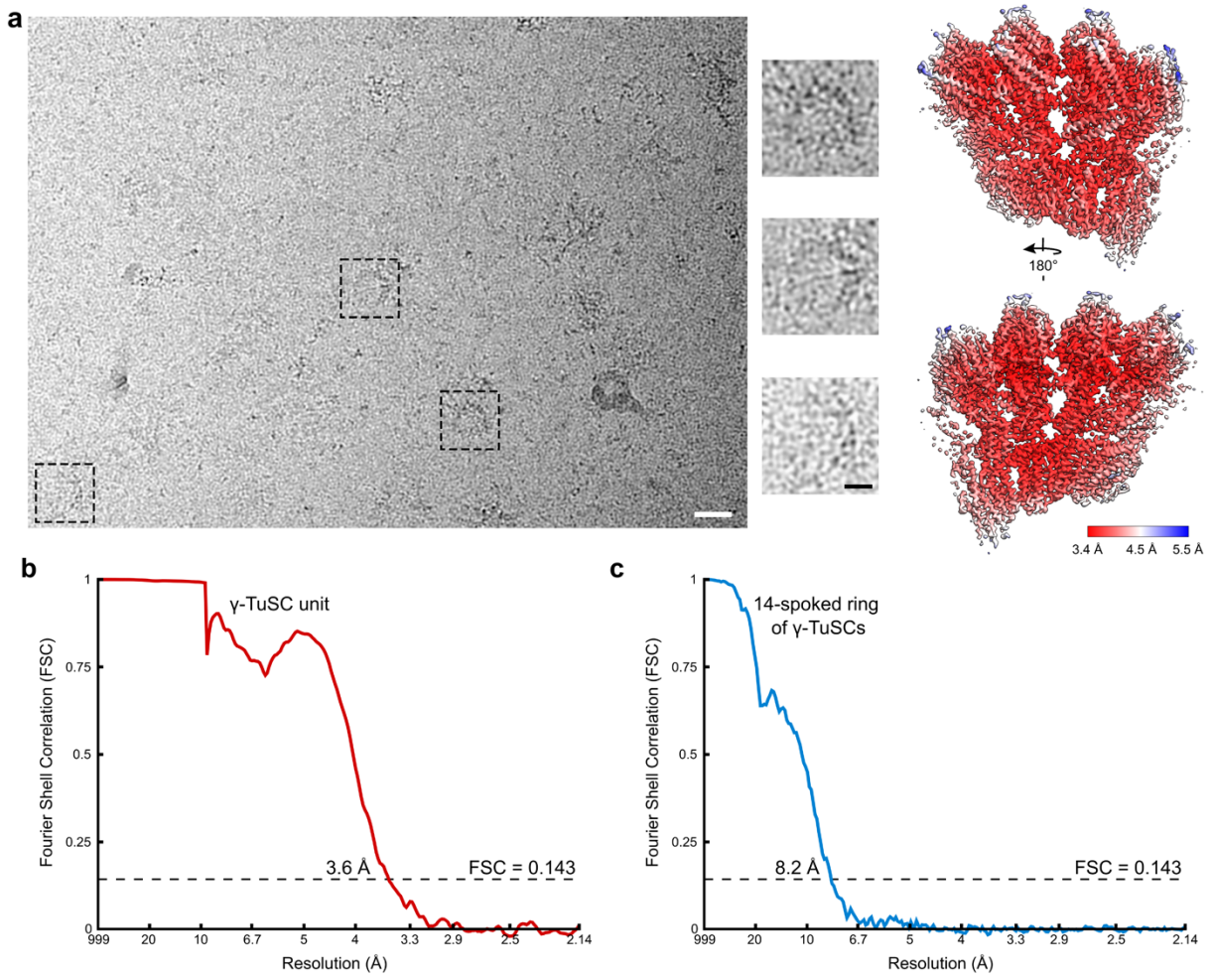

Figure 21: The cryo-EM micrograph and the estimated resolutions of cryo-EM reconstructions

(a) The cryo-EM micrograph of the FLAG-purified γ-TuSC/Spc72/Stu2 complex. The chosen ring-like particles circled in black rectangles were shown enlarged on the right, separately. Micrographs were low-pass filtered to 20 Å. Scale bars, 25 nm (micrograph),

and 10 nm (particles) (left). Reconstructed γ-TuSC dimers were colored according to the local resolution estimation (right).
(b,c) Fourier shell correlation (FSC) between two independently refined half-sets of reconstructions of the γ-TuSC unit within a γ-TuSC dimer (**b**) and the 14-spoked ring of γ-TuSC oligomer (**c**). The resolution values of 3.6 Å (γ-TuSC dimer) and 8.2 Å (14-spoked ring of γ-TuSC oligomer) that cross the FSC=0.143 thresholds are indicated.
Data in panels (**a-d**) were produced by Bram J.A. Vermeulen.

The cryoSPARC program was used for the initial 3D model production (Fig. 22a)[188]. To obtain a better resolution of the γ-TuSC units, the cryo-EM data was processed in two complementary strategies to obtain the two resolutions for the structural analysis: in the first branch, γ-TuSC units were treated as individual asymmetric units with the final resolution of 3.6 Å (Fig. 22b,c), which was sufficient to build a full atomic model of the γ-TuSC structure (Fig. 23b, Table 6). More specifically speaking, the previously partially resolved regions of Spc97 (Thr232-Asp272, Glu495-Pro502, Asn539-Ser566, and Ala686-Ile737) and Spc98 (Asn626-Leu656) in the inter-γ-TuSC interface were now fully accessible in this structure (Fig. 23b). In the second branch, the 14-spoked γ-TuSC oligomers were analyzed in several rounds of particle sorting with a final resolution of 8.2 Å (Fig. 22b,d). The individual γ-TuSC atomic model could be seamlessly docked into the reconstructed 14-spoke γ-TuSC ring, which allowed for the analysis of the γ-tubulin arrangement of the cytoplasmic nucleation unit in *C. albicans* (Fig. 23b). Furthermore, with the comparison of the 13-protofilament MT in yeast *S. pombe*, our complex of γ-TuSC/Spc72/Stu2 assembles into a ring with helical parameters similar as the 13-protofilament MT in *S. pombe* (Table 5). In conclusion, the γ-TuRC structure containing the CM1 motif is in the closed, MT-compatible conformation (Fig. 23c,d). It is different from the spiral γ-TuSC oligomer in *S. cerevisiae* and the vertebrate human γ-TuRC in the presence of the CM1 motifs[119, 149, 186, 189].

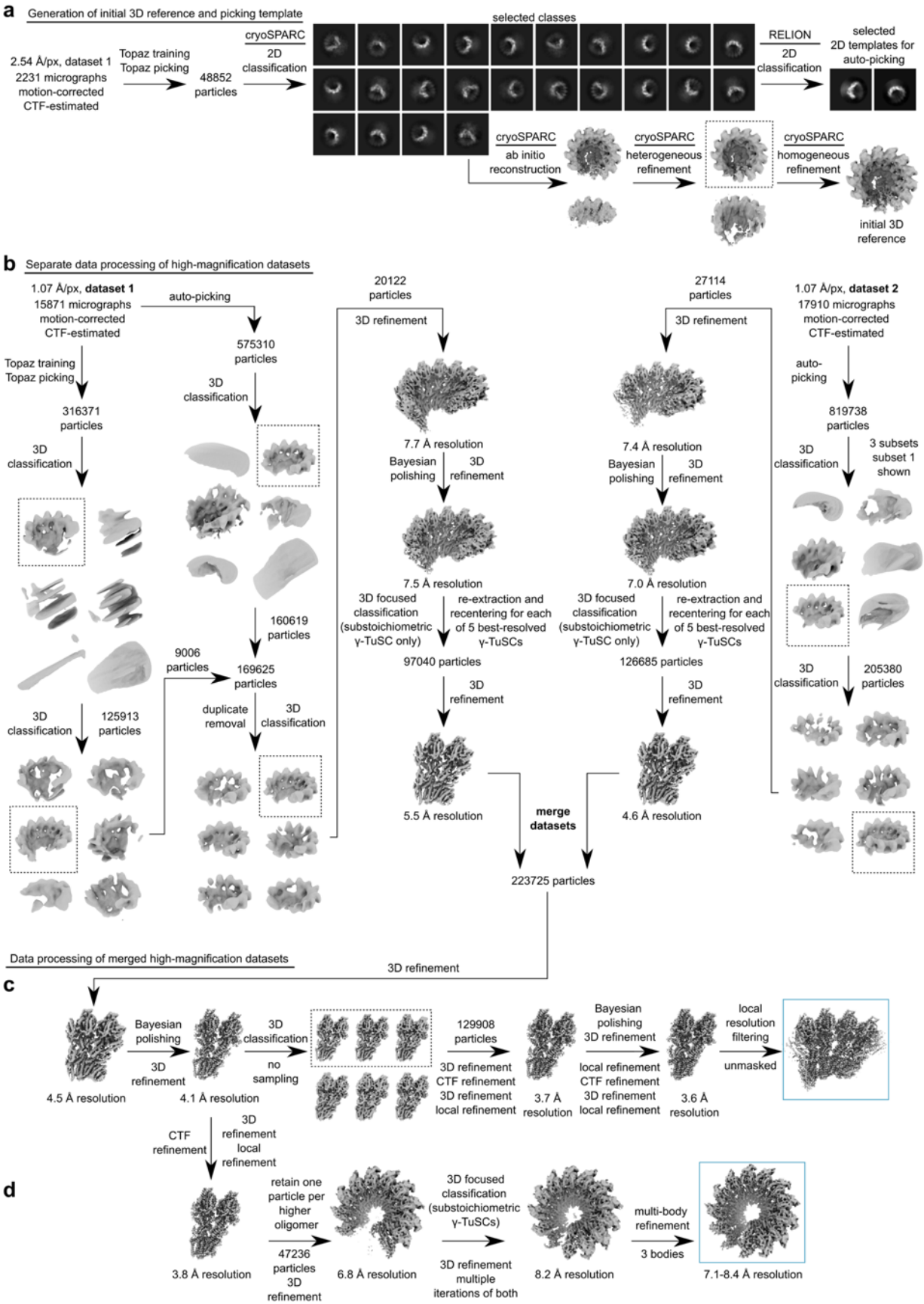
a
Generation of initial 3D reference and picking template
2.54 Å/px, dataset 1
2231 micrographs
motion-corrected
CTF-estimated
Topaz training
Topaz picking
48852
particles
cryoSPARC
2D
classification
selected classes
RELION
2D
classification
selected
2D templates for
auto-picking
cryoSPARC
ab initio
reconstruction
cryoSPARC
heterogeneous
refinement
cryoSPARC
homogeneous
refinement
initial 3D
reference
b
Separate data processing of high-magnification datasets
1.07 Å/px, dataset 1
15871 micrographs
motion-corrected
CTF-estimated
auto-picking
575310
particles
3D
classification
Topaz training
Topaz picking
316371
particles
3D
classification
160619
particles
9006
particles
169625
particles
3D
classification
125913
particles
duplicate
removal
3D
classification
20122
particles
3D refinement
7.7 Å resolution
Bayesian
polishing
3D
refinement
7.5 Å resolution
3D focused
classification
(substoichiometric
γ-TuSC only)
re-extraction and
recentering for each
of 5 best-resolved
γ-TuSCs
97040 particles
3D
refinement
5.5 Å resolution
27114
particles
3D refinement
7.4 Å resolution
Bayesian
polishing
3D
refinement
7.0 Å resolution
3D focused
classification
(substoichiometric
γ-TuSC only)
re-extraction and
recentering for each
of 5 best-resolved
γ-TuSCs
126685 particles
3D
refinement
4.6 Å resolution
1.07 Å/px, dataset 2
17910 micrographs
motion-corrected
CTF-estimated
auto-
picking
819738
particles
3D
classification
3 subsets
subset 1
shown
3D
classification
205380
particles
merge
datasets
223725 particles
Data processing of merged high-magnification datasets
3D refinement
c
4.5 Å resolution
Bayesian
polishing
3D
refinement
4.1 Å resolution
3D
classification
no
sampling
129908
particles
3D refinement
CTF refinement
3D refinement
local refinement
3.7 Å
resolution
Bayesian
polishing
3D refinement
local refinement
CTF refinement
3D refinement
local refinement
3.6 Å
resolution
local
resolution
filtering
unmasked
CTF
refinement
3D
refinement
local
refinement
d
3.8 Å resolution
retain one
particle per
higher
oligomer
47236
particles
3D
refinement
6.8 Å resolution
3D focused
classification
(substoichiometric
γ-TuSCs)
3D refinement
multiple
iterations of both
8.2 Å resolution
multi-body
refinement
3 bodies
7.1-8.4 Å resolution

Figure 22: Cryo-EM data processing flowchart of the γ-TuSC/Spc72/Stu2 complex
(a) The flowchart shows the 2D template generation for particle picking and the 3D reference map for 3D classification and refinement. cryoSPARC[188] and RELION[190] were used for 2D classification and Topaz training[191] was used for particle auto-picking. cryoSPARC[188] was used for the initial 3D reference generation.
(b-d) Two higher magnification datasets were first processed independently and merged to resolve the structure of the γ-TuSC dimer within the oligomer to 3.6 Å (**c**), sufficient to build and refine a full atomic model of γ-TuSC dimer and Spc72^{CM1} motif (Table 6), as well as the full ring of seven γ-TuSC oligomer to 8.2 Å (**d**). The data processing was performed in RELION[190].
Data in panels (**a-d**) were produced by Bram J.A. Vermeulen.

Table 5 Geometric parameters of γ-tubulin within the *C. albicans* γ-TuRC in complex with Spc72 and Stu2 (coordinate taken at Gln12) compared to α-tubulin in a 13 protofilament MT (*S. pombe*, PDB 5MJS[192], coordinate taken at Gln15). n = 13 individual tubulins, shown as mean ± standard deviation

	C. albicans γ-TuRC with Spc72 and Stu2	*S. pombe* 13 protofilament MT
Distance to helical axis (Å)	102.5 ± 1.5	101.9 ± 0.0
Rotation around axis per spoke (degrees)	27.6 ± 0.7	27.7 ± 0.3
Helical pitch increment per spoke (Å)	9.2 ± 0.8	9.5 ± 0.0

The table was produced by Bram J.A. Vermeulen.

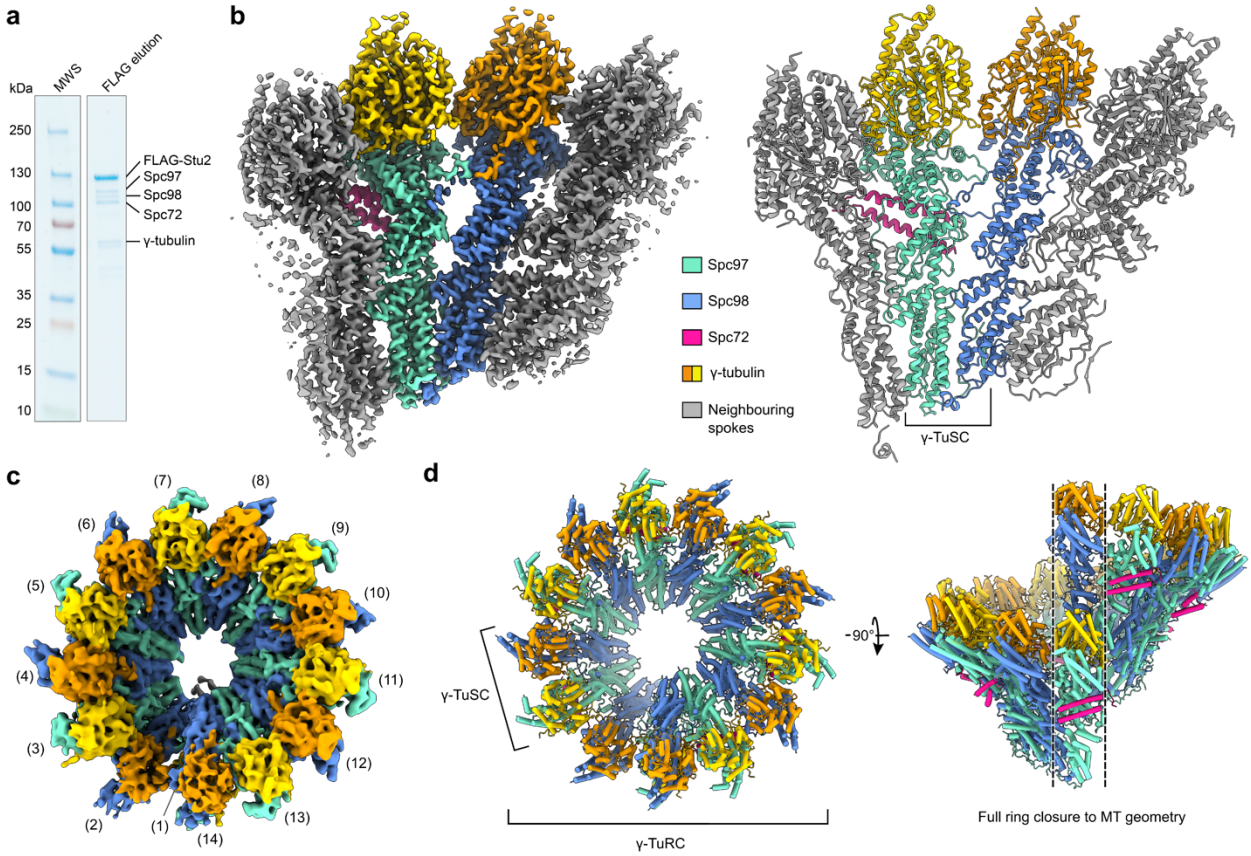

Figure 23: The overall architecture of *C. albicans* γ-TuRC

(a) The Coomassie blue staining of the FLAG-Stu2 purified γ-TuSC/Spc72$^{1-599}$/FLAG-Stu2 complex (**Fig. 19c**). The five components of Spc97, Spc98, γ-tubulin, Spc72, and Stu2 are indicated with black lines. kDa, kilodalton unit. MWS, molecular weight.

(b) The cryo-EM density map (left) and the atomic structure (right) of the γ-TuSC units within the γ-TuSC oligomer. The adjacent γ-TuSC units were shown in grey color and the components of Spc97/Spc98/γ-tubulin, Spc72^{CM1} were depicted in different colors.

(c) The top view of cryo-EM reconstructed 14-spoked γ-TuSC oligomer which forms into a ring-like structure.

(d) The top view of cryo-EM reconstructed 14-spoked γ-TuSC oligomer (Left) and the 90° vertically rotated ring shows a fully and conformationally closed ring geometry matching to the 13-protofilament MT (Right).

Data in panel (**a**) were produced by Anjun Zheng.

Data in panels (**b-d**) were produced by Bram J.A. Vermeulen.

Table 6 Cryo-EM data collection, refinement, and validation statistics

	Candida albicans γ-TuSC in complex with Spc72 within ring-like higher oligomer (EMDB-xxxx) (PDB xxxx)	Full ring of *Candida albicans* γ-TuSC in complex with Spc72 (EMDB-xxxx) (PDB xxxx)	Spokes 12 and 13 of the human γ-TuRC in complex with CDK5RAP2 (PDB xxxx)
Data collection and processing			
Magnification	81000 x	81000 x	
Voltage (kV)	300	300	
Electron exposure (e–/Å^2)	47	47	
Defocus range (μm)	-1 to -2.6	-1 to -2.6	
Pixel size (Å)	1.07	1.07	
Symmetry imposed	C1	C1	
Initial particle images (no.)	1711419	1711419	
Final particle images (no.)	129908	8261	
Map resolution (Å) FSC threshold	3.6 0.143	 0.143	
Map resolution range (Å)	3.4-5.5		
Refinement			
Initial model used (PDB code)	*de novo*	*de novo*	6V6S and 6X0V
Model resolution (Å) FSC threshold			4.5
Model resolution range (Å)			
Map sharpening *B* factor (Å^2)			
Model composition Non-hydrogen atoms Protein residues Ligands			
B factors (Å^2) Protein Ligand			
R.m.s. deviations Bond lengths (Å)			

Bond angles (°)			
Validation MolProbity score Clashscore Poor rotamers (%)			
Ramachandran plot Favored (%) Allowed (%) Disallowed (%)			

The table was produced by Bram J.A. Vermeulen.

3.2.3 The oligomerisation of γ-TuSC is accompanied by conformational changes

In the previous study, we obtained the cryo-EM structure of the monomeric γ-TuSC (PDB 7ANZ) in *C. albicans*. The arrangement of γ-tubulins deviates from the configuration of α/β-tubulin units in MTs[3]. With the cryo-EM structure of the oligomerised *C. albicans* γ-TuSC ring in hand, the comparison of the monomeric and the oligomeric γ-TuSC structures was possible. This indicated extensive conformational changes within the γ-TuSC unit (Fig. 24a). Within the γ-TuSC, the N-terminal part of the GRIP1 domains remain structurally unaffected (residues 91-308: Cα RMSD 1.86 Å (Spc97), residues 150-306: Cα RMSD 1.42 Å (Spc98)), however, the C-terminal parts of GRIP1 undergo a hinge-like rigid-body rotation that positions in the GRIP2 domains and the associated γ-tubulins in an MT-compatible conformation (Fig. 24b). The conformational change is accompanied by the extension interface between the GRIP2 domains in the intra-γ-TuSC (Fig. 24c) and an additional interface between the γ-tubulin molecules in the intra-γ-TuSC (Fig. 24d). Regarding the contact area provided by the GRIP1 domains, it is mainly mediated by a small helix from Spc97 which docks the amino acid of phenylalanine at position 721 into a strongly hydrophobic pocket of Spc98 (Fig. 24e). This Spc97 helix was not structurally resolved in the isolated γ-TuSC model[3] but is now available in the oligomerised γ-TuSC structure in *C. albicans*. It might be stabilized by interactions from the neighboring γ-TuSC units.

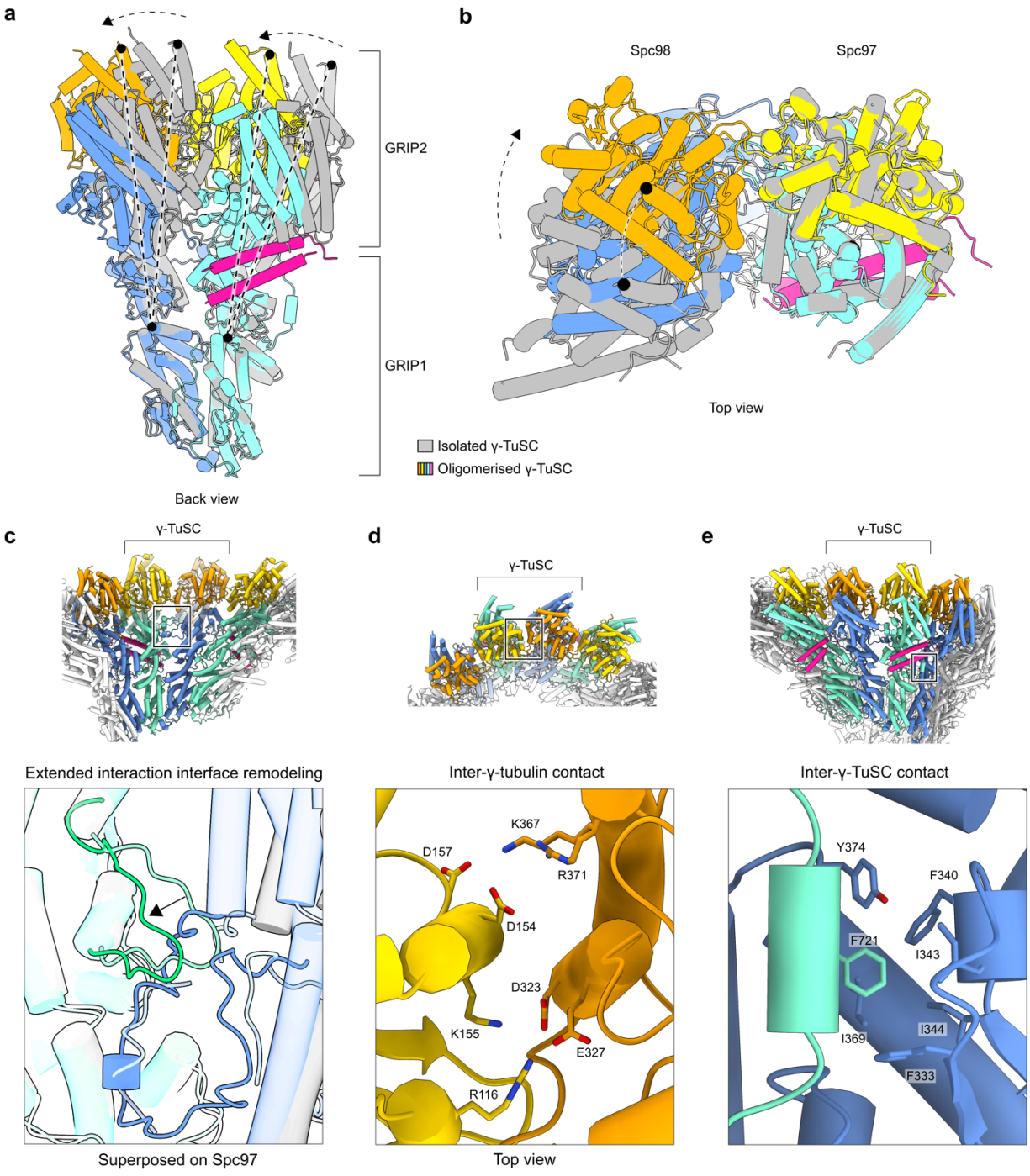

Figure 24: The structural comparison of the monomeric and oligomeric γ-TuSC complexes in *C. albicans*

(a) The overlapping structures of the monomeric and oligomeric γ-TuSC complexes predominantly occur between the GRIP^{1C} (C-terminal part of the GRIP1 domain) and the

GRIP2 domain of Spc97/98, where they interact with γ-tubulins. The oligomeric γ-TuSC are colored as in **Fig. 23b**; the monomeric γ-TuSC are colored in grey.
(b) The γ-tubulin molecules are closer to each other in the oligomeric γ-TuSC compared to that in the isolated γ-TuSC. The oligomeric γ-TuSC are colored as in **Fig. 23b**; the monomeric γ-TuSC are colored in grey. The model in (**a**) is the same as in (**b**) but with a top view.
(c) The insertion loop between GRIP2 domains of Spc98$^{D627\text{-}K650}$ in the intra-γ-TuSC regions can be seen in the oligomeric γ-TuSC, whereas this insertion loop was only partially resolved in the monomeric γ-TuSC[3].
(d) The electrostatic interactions on the amino acid levels between two γ-tubulins in the oligomeric γ-TuSCs.
(e) Spc97^{Phe721} is docked into a strongly hydrophobic pocket formed by the neighboring Spc98.
Data in panels (**a-e**) were produced by Bram J.A. Vermeulen.

In conclusion, Spc72-bound γ-TuSC oligomers coupled large-scale conformational changes to a stoichiometrically MT-compatible conformation in a closed form, especially in terms of the GRIP2 domains of Spc97/Spc98 spokes and the γ-tubulins.

3.2.4 The dimeric Spc72^{CM1} bound to γ-TuSC unit is essential for the oligomerisation of γ-TuSC and the normal cell function

As shown in Fig. 24a, two α-helices forming coiled coils on the outer surface of every Spc97 GRIP2 domain were found in our cryo-EM reconstructed γ-TuSC oligomer. By using the sequence-free model-building function in ModelAngelo[224], the two α-helices were identified to be the dimeric CM1 motifs from Spc72 (Fig. 25a), revealing a dimeric binding mode similar to human CDK5RAP2[120] but different from the monomeric Spc110 in the spiral γ-TuSC oligomers formed in *S. cerevisiae*[149]. The CM1$_{in}$ (CM1 inner helix) is bound and interacts with Spc97 by four distinct interfaces (Fig. 25b), including hydrophobic contacts with two short α-helices on the Spc97 GRIP1 domain (contact 1: CM$^{M257/F260/L264}$ Spc97$^{F342/I345/F346/Y352}$), whereas the corresponding region from R337 to Y353 of Spc97 was not visible in the isolated γ-TuSC structure (PDB: 7ANZ)[3]. The other

three Spc72^{CM1} and Spc97 interacting interfaces include both hydrophobic and electrostatic contacts: contact 2 (CM1$^{I252/V248}$ and Spc97^{L528}), contact 3 (CM1$^{V248/N244/E241}$ and Spc97$^{L755/N756/R762}$) and contact 4 (CM1^{E241} and Spc97$^{R853/R855}$) (Fig. 25b). Additionally, by looking into the interactions between CM1$_{in}$ (the inner helix of the dimeric CM1 motif) and Spc97, they are consistent with a previous mutagenesis study on the Spc72 binding sites (Spc72N^{3A}: K251A/Q253A/K255A; Spc72N^{9A}: I247A/**V248A**/N249A/Y250A/K251A/**I252A**/Q253A/L254A/K255A) with the γ-TuSC, which is reflected by the close interaction of CM1$^{\mathbf{V248/I252}}$ (Fig. 25b, contact 2) with Spc97 on the atomic structural level (Fig. 25b,c)[133].

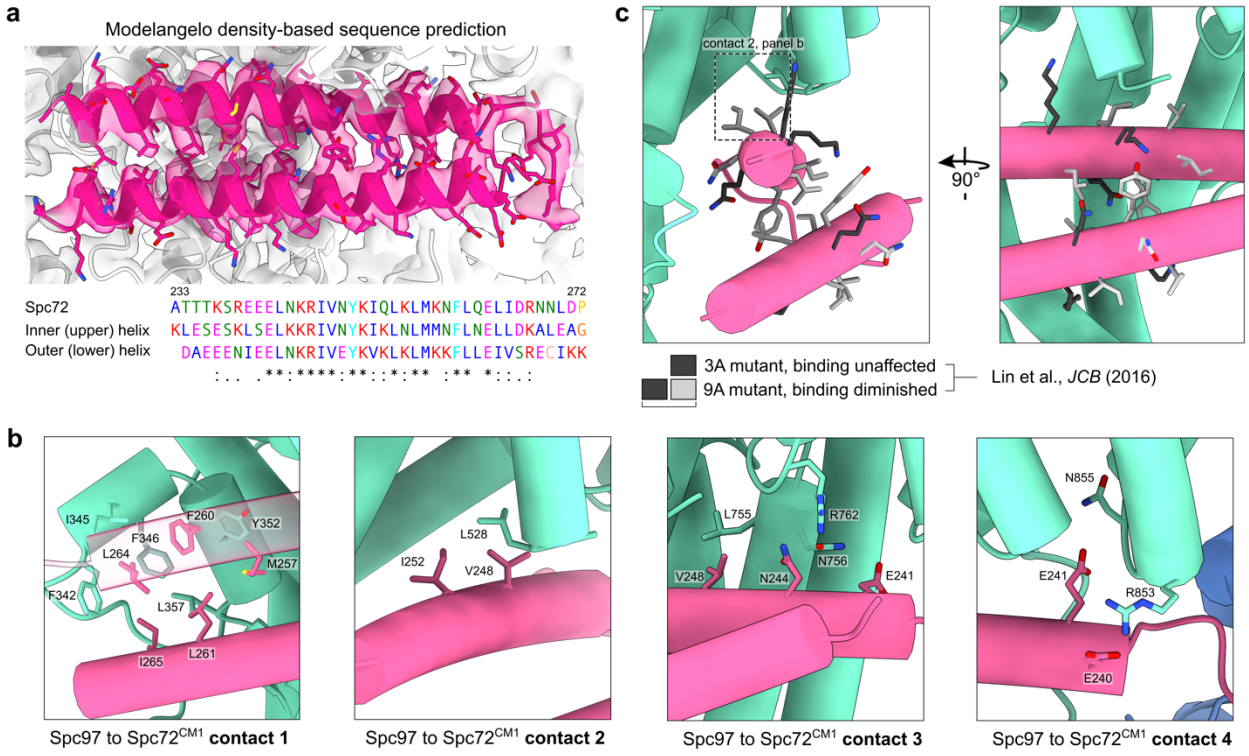

Figure 25: The detailed binding interfaces of Spc72^{CM1} and γ-TuSCs

(a) The Modelangelo[224] density-based sequence prediction for the density bound to Spc97 with the outcome of the dimeric CM1 motifs from Spc72. The Spc72^{CM1} motif sequence (A233-P272) and the Modelangelo[224] predicted Inner (Upper) helix and Outer (lower) sequences are shown, the black dots indicate the same amino acids predicted between the Inner and Outer helixes, and the black asterisks represent the predicted amino acids of the Inner and Outer helixes as in Spc72^{CM1}. The CM1 motifs are in magenta colors.

(b) The 4 interacting contacts in amino acid level between Spc72^{CM1} (magenta) and Spc97 (light blue). The interacting amino acids are labeled.
(c) Description of Spc72^{CM1} with 3A and 9A mutations as in Lin et al[133]. The 9A mutant (light and dark grey) sabotaged the binding affinity to γ-TuSC whereas the binding affinity of the 3A mutant (dark grey) and γ-TuSC remained unaffected which is consistent with the binding mode of CM1 and Spc97 in our structure.
Data in panels (**a-c**) were produced by Bram J.A. Vermeulen.

The CM1 motif contributes to hydrogen contacts towards the Spc98 GRIP2 domain of the neighboring γ-TuSC unit with the amino acid interacting between the N-terminal side of the CM1 motif and the neighboring Spc98 (T234^{CM1} and V500^{Spc98} (backbone to backbone), T236^{CM1} and D497^{Spc98}, S238^{CM1} and S471^{Spc98}) (Fig. 26b,c). These interactions also play an important role in the γ-TuSC oligomerisation. To test the importance of the interface between Spc72 and the neighboring Spc98, the mutant Spc72 (T234P and T236A, referred to as the Spc72^{PA}) was introduced to the co-expression construct of γ-TuSC/Spc72^{PA}/FLAG-Stu2. With SEC (Size-exclusive chromatography) (Fig. 26d) and Western blotting (Fig. 26e) analysis, the Spc72^{PA} mutant complex presented the major ratio from the oligomeric peak shifting to fractions corresponding to non-oligomerised γ-TuSC compared to the non-mutated γ-TuSC/Spc72/FLAG-Stu2 complex (Fig. 26d).

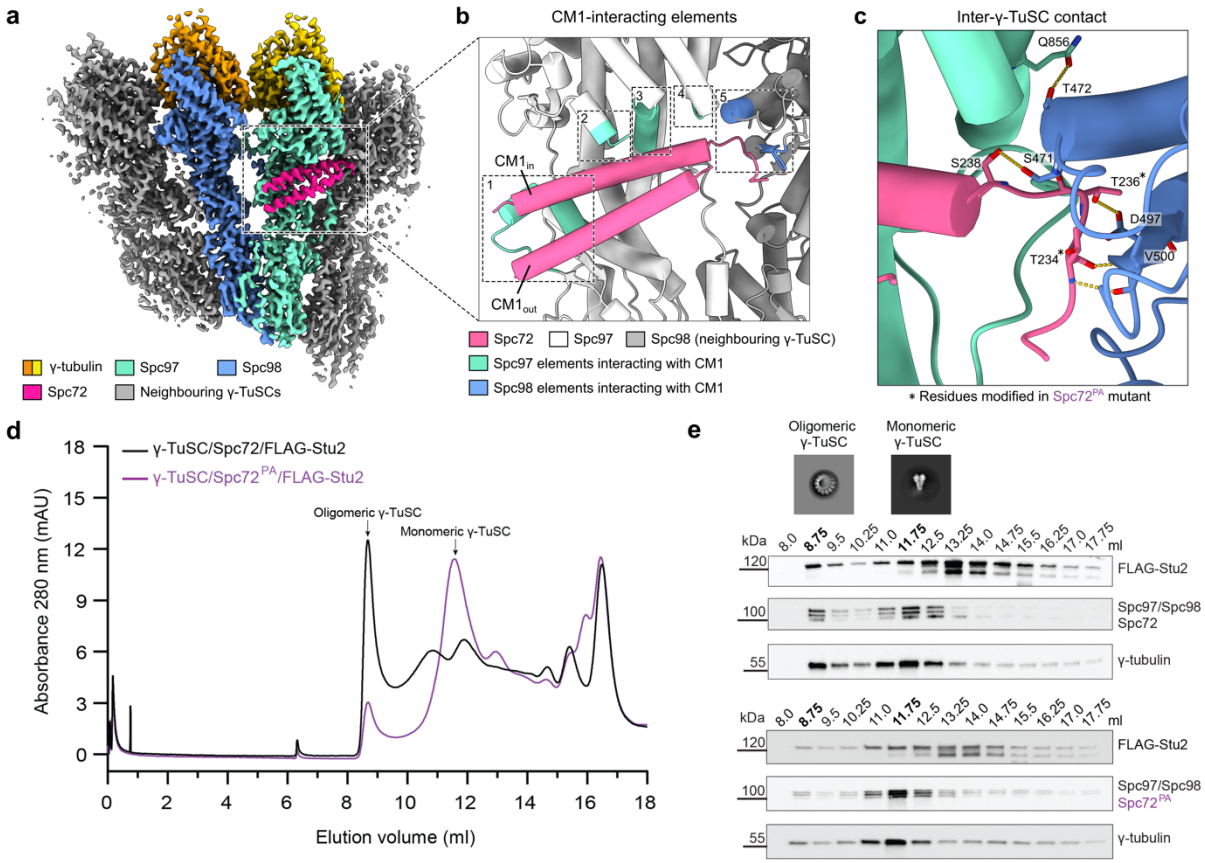

Figure 26: The *in vitro* analysis of the impact of the Sp72^{PA} mutant on γ-TuSC oligomerisation

(a,b) Overview of the five interaction contacts of Spc72^{CM1} with the intra/inter-γ-TuSCs. The outer ($CM1_{out}$) and inner ($CM1_{in}$) helices together form coiled coils. Spc97/Spc98/γ-tubulin and Spc72^{CM1} are colored in the same as in **Fig. 23b**. The neighboring γ-TuSCs are shown in grey.

(c) Amino acids of T234 and T236 of Spc72^{CM1} interact with Spc98.

(d) SEC profiles of Spc72^{PA} mutated γ-TuSC/Spc72^{PA}/FLAG-Stu2 complex and the non-mutated γ-TuSC/Spc72/FLAG-Stu2 complex with the same amount of sample injected into the column.

(e) Visualisation of the protein content of fractions from SEC profiles shown in panel (**d**) by Western blotting. Representative negative stain 2D classes for monomeric and oligomeric species γ-TuSCs highlight the oligomeric state of complexes in indicated fractions. Immunoblotting was performed with antibodies against FLAG-Stu2, His-

Spc97/His-Spc98/His-Spc72^{WT}/His-Spc72^{PA}, and γ-tubulin (home-made anti-*C. albicans* γ-tubulin antibody).
Data in panels (**a-c**) were produced by Bram J.A. Vermeulen.
Data in panels (**d and e**) was produced by Anjun Zheng.

To further identify the impact of T234P/T236A mutations on Spc72 *in vivo*, the model organism *S. cerevisiae* was used due to the higher biosafety level lab that is required for *C. albicans* work. The sequence alignment of Spc72 between these two species indicated that the PA point mutations were not well conserved in *S. cerevisiae*. To better cover the T234/T236 positions in *S. cerevisiae* Spc72, the region from P55 to N62 was identified and deleted (Fig. 27a). The deletion mutant of *spc72*$^{\Delta P55\text{-}N62}$ was introduced in the S288c background strain in which *SPC72* is vital for viability[167] whereas *SPC72* is not strictly essential the W303 strain but its absence leads to pronounced growth defects[144].
The drop-out test for cell viability of the wild-type *SPC72* and *spc72*$^{\Delta P55\text{-}N62}$ cells showed no difference at temperatures ranging from 16ºC to 30ºC (Fig. 27b). However, when checking phenotypes of *spc72*$^{\Delta P55\text{-}N62}$ cells in W303 background by tracing signals of *TUB1-GFP* (MT marker) and *SPC42-mCherry* (SPB marker), *spc72*$^{\Delta P55\text{-}N62}$ cells showed defective cytoplasmic MTs (cMTs) (Fig. 27c, yellow arrows) including abnormally long cMTs and loss of cMTs (Fig. 27c; asterisks). The DAPI staining experiment also showed that the normal nuclei separation was impaired in the mutant cells: 4 times higher frequency of a stretched DAPI staining region located in the bud neck in *spc72*$^{\Delta P55\text{-}N62}$ cells compared with wild-type *SPC72* cells, indicating a delay in nuclear separation; a 4-time higher frequency of two DAPI staining regions confined in the mother cell in *spc72*$^{\Delta P55\text{-}N62}$ cells compared with that in wild-type *SPC72* cells (Fig. 27d,e).

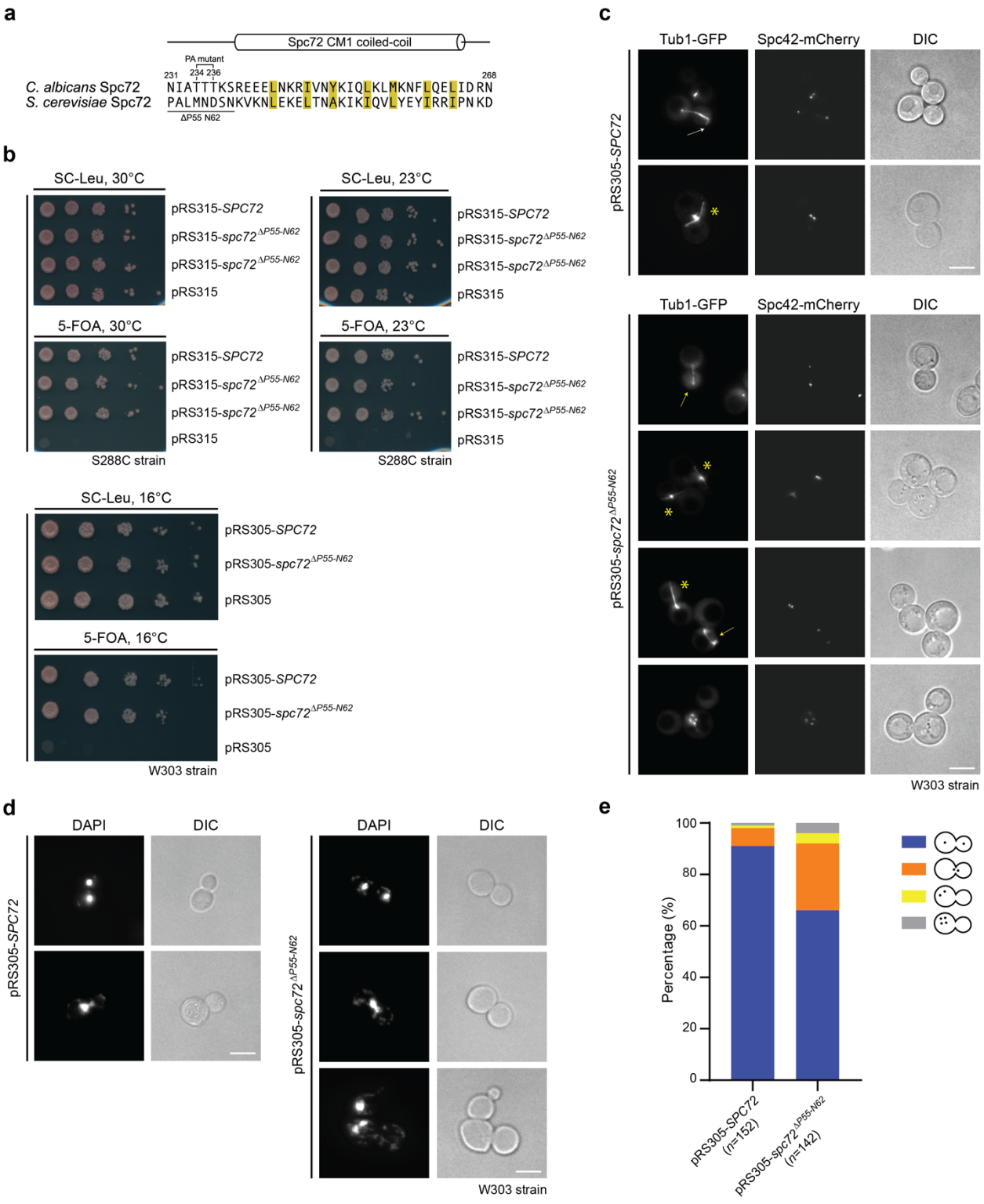

Figure 27: The in vivo analysis of the impact of *spc72*$^{\Delta P55\text{-}N62}$ mutant on the cell viability and cell cycle in *S. cerevisiae*

(a) Sequence alignment of *C. albicans* and *S. cerevisiae* Spc72^{CM1} motifs. The

hydrophobic residues at the dimerization interface are shown in yellow colors. Residues mutated to proline and alanine (T234P and T236A) in *C. albicans* Spc72 are not conserved in *S. cerevisiae* Spc72. The region of P55-N62 on *S. cerevisiae* Spc72 covering *C. albicans* T234P and T236A mutations is marked by a line.

(b) The viability test of *spc72*$^{\Delta P55\text{-}N62}$ mutant cells in *S. cerevisiae*. The wild-type and *spc72*$^{\Delta P55\text{-}N62}$ cells were serially diluted and grown on SC-Leu or 5-FOA plates for 2 days at 30°C, 3 days at 23°C, or 5 days at 16ºC. Viability tests were performed three times.

(c) Phenotypes of *SPC72* and *spc72*$^{\Delta P55\text{-}N62}$ cells (W303 strain background) cultured on 5-FOA plates at 16°C were observed by using *TUB1-GFP* (marking microtubules) and *SPC42-mCherry* (marking the SPB). Cytoplasmic MTs are indicated by a white arrow and defective astral MTs by yellow arrows. Elongated astral MTs are marked by yellow asterisks. Scale bar, 5 μm. DIC = differential interference contrast. Phenotype analysis was performed independently twice.

(d) DAPI staining analysis of *SPC72*, and *spc72*$^{\Delta P55\text{-}N62}$ mutant cells (W303 strain background) cultured at 16°C. Scale bar, 5 μm. DIC = differential interference contrast. Phenotype analysis was performed independently twice.

(e) Quantification of nuclear phenotypes of *SPC72* and *spc72*$^{\Delta P55\text{-}N62}$ cells from (**d**) shown as bar plot (n=152, *SPC72* cells and n=142, *spc72*$^{\Delta P55\text{-}N62}$ cells). In *SPC72* cells, 91% of cells display normal separation of nuclei (dark blue), 7% of cells have the nuclei at the bud neck (orange color), 1% of cells have the nuclei in the mother cell body (yellow color) and 1% of cells have multiple nuclei (grey color). In *spc72*$^{\Delta P55\text{-}N62}$ mutant cells, 66% of cells display normal separation of nuclei (dark blue), 26% of cells have nuclei at the bud neck (orange color), 4% of cells have the nuclei in the mother cell (yellow color) and 4% of cells have multiple nuclei (grey color).

Data in panel (**a**) were produced by Bram J.A. Vermeulen.

Data in panels (**b-e**) were produced by Anjun Zheng.

3.2.5 The dimeric CM1 motif interacting with γ-TuRC is evolutionarily conserved

The CM1 motif of *C. albicans* Spc72 binds to Spc97 as a dimer. This prompted us to investigate the CM1 binding mode across a wide range of ascomycetes and several

representative eukaryote species by using DeepCoil2[193]. With the alignment of the coiled-coil interface residues and the predicted propensity of the coiled-coil formation in CM1 motifs, it turned out that the dimeric CM1 motifs are highly conserved including human CDK5RAP2, *C. albicans* Spc110, and *S. cerevisiae* Spc72, except for *S. cerevisiae* Spc110 adopting a monomeric binding mode to γ-TuSCs (Fig. 28a). With the knowledge of the conserved dimerized CM1 binding mode across species, we further compared the differences in detail between the *C. albicans* γ-TuSC oligomer and the human γ-TuRC on a structural level[2, 119, 186] . The close inspection of human γ-TuRC with the CDK5RAP2^{CM1} motif (EMD-21985)[120] revealed the corresponding equivalents in the human system participated in the interaction interface as *C. albicans* Spc72 CM1 (Fig. 28b,c).

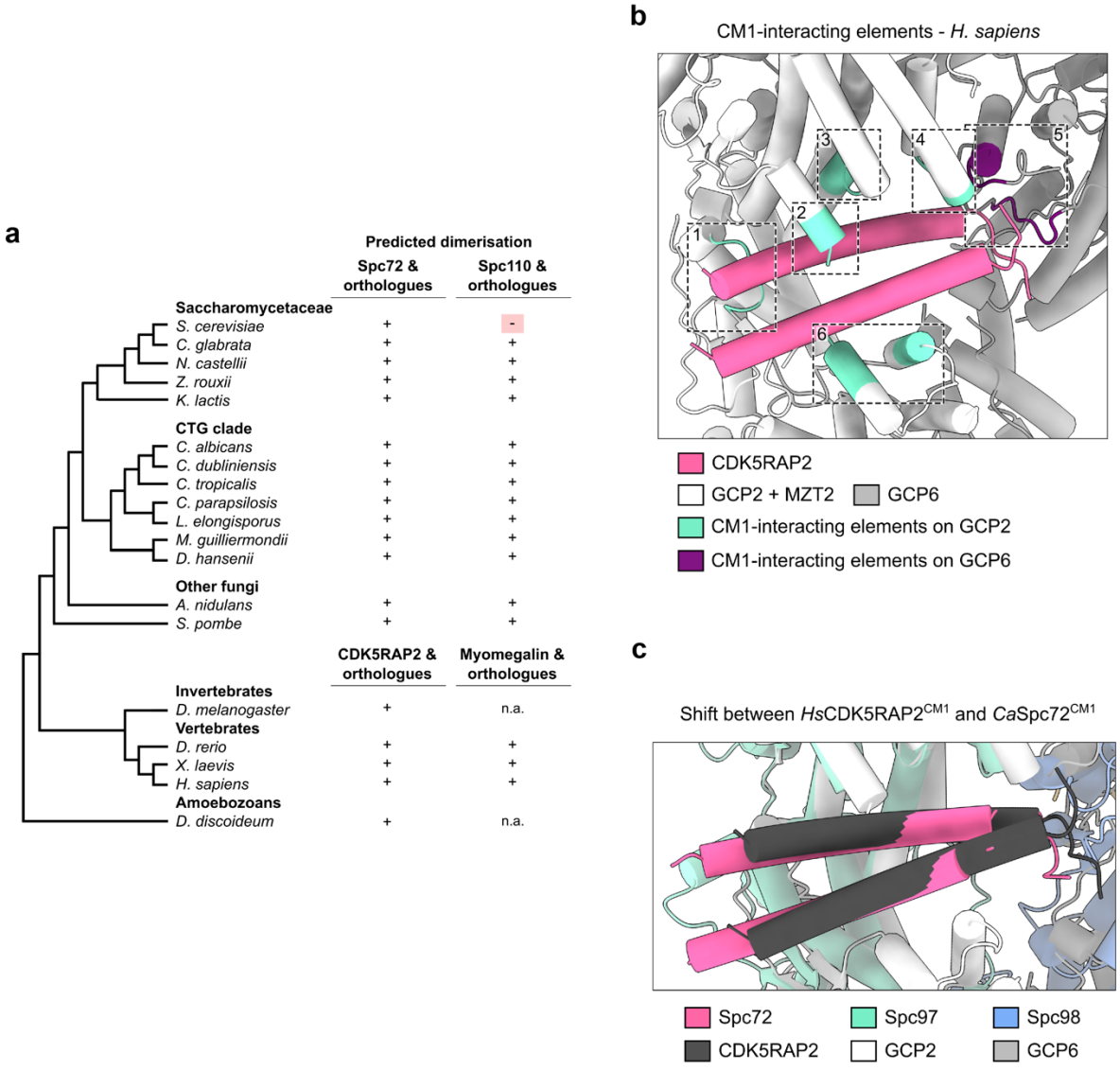

Figure 28: The dimeric CM1 motif interacting with γ-TuRC is evolutionarily conserved

(a) The CM1 dimerisation motif prediction among Spc72/Spc110 orthologues in fungi and CDK5RAP2/myomegalin (CDK5RAP2 paralogue) in higher eukaryotes along the evolutionary tree. DeepCoil2[194] was used for dimerisation prediction. Plus represents the dimerisation and minus represents the non-dimerisation of the CM1 motif.

(b) The interacting interfaces containing the contacts 1 to 4 (marked in dashed, black rectangles) on human GCP2 (homologue of Spc97), GCP6, and CDK5RAP2^{CM1} adopt the same binding mode as the interacting interfaces formed by Spc72^{CM1}, Spc97, and the neighboring Spc98 in the oligomeric γ-TuSC in *C. albicans* (**Fig. 26a,b**). The color scheme is indicated.

(c) The Spc72^{CM1} and CDK5RAP2^{CM1} position alignment from the zoom-in view on the whole structural level of *C. albicans* and humans γ-TuRCs, indicating a slight shift while retaining the same binding mode of the interaction elements shown in Fig. 28b. The aligned structures were superposed by aligning Spc97 with GCP2$^{473-895}$. The color scheme is indicated.

Data in panel (**a-c**) were produced by Bram J.A. Vermeulen.

However, due to the not well-conserved amino acid sequence (Fig. 29a) and not well-constructed structural models (PDB: 6V6S/6X0V) in the human system, the structure of human γ-TuRC with the CDK5RAP2^{CM1} was further modified by Bram J.A. Vermeulen to show the different binding modes of the CM1 motifs and γ-TuRCs between *C. albicans* and human (Fig. 29b). The dimeric CM1 motif binding mode was conserved in these two systems, however, from the residual level and the specific interaction positions, the CM1 motif-containing α-helix is shifted by 8-14 Å (inner and outer helix, respectively) in the relative positioning of CM1-interacting spokes in *C. albicans* and human γ-TuRCs (Fig. 28c). In conclusion, even the dimeric CM1 motif binding mode is conserved in human and *C. albicans* γ-TuRCs, the specific amino acid interacting positions and angles of the CM1 helixes vary, which might be the evolutionary outcome of adapting to variations of γ-TuRC architecture in different species.

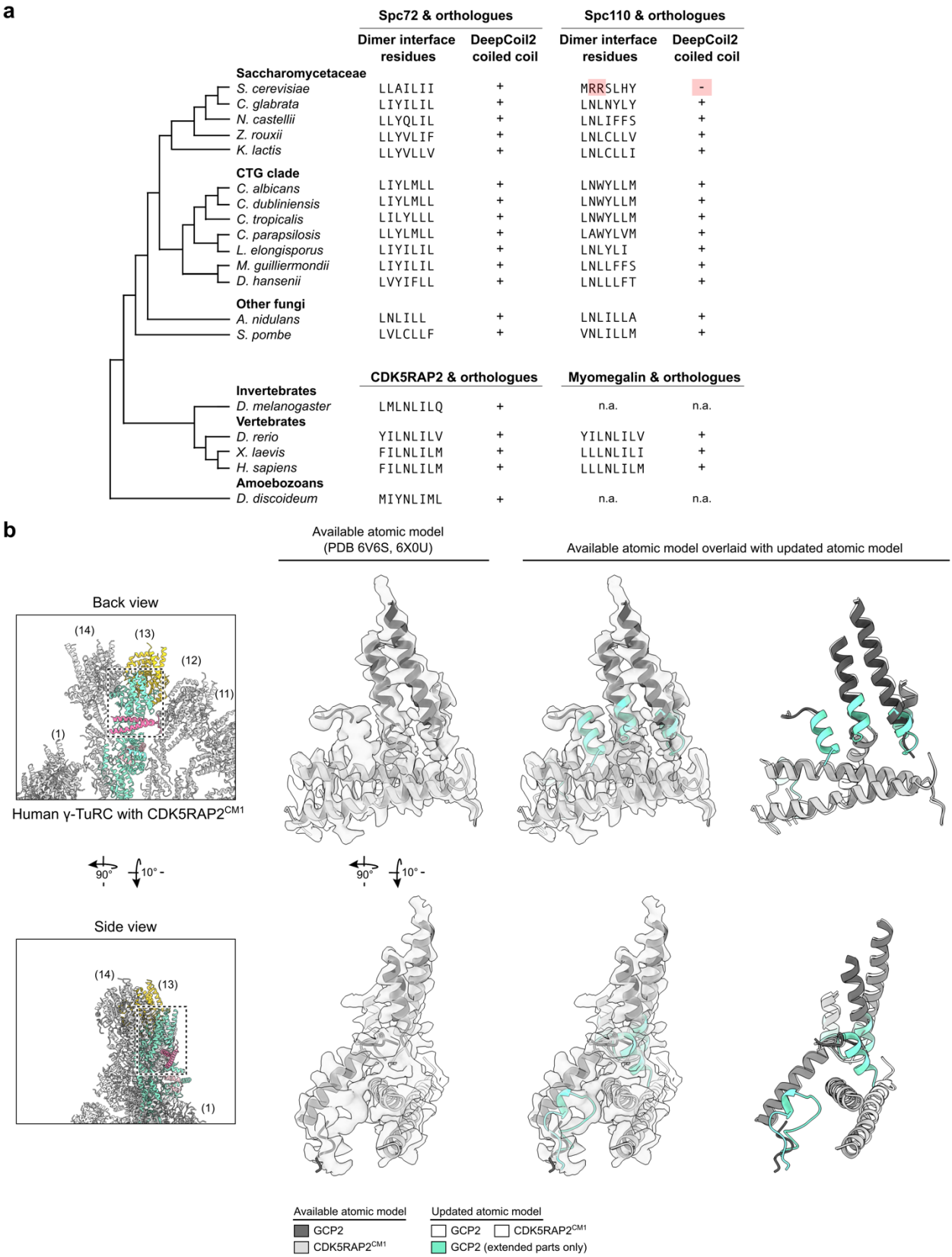
a
Spc72 & orthologues
Dimer interface residues
DeepCoil2 coiled coil
Spc110 & orthologues
Dimer interface residues
DeepCoil2 coiled coil
Saccharomycetaceae
S. cerevisiae LLAILII + MRRSLHY -
C. glabrata LIYILIL + LNLNYLY +
N. castellii LLYQLIL + LNLIFFS +
Z. rouxii LLYVLIF + LNLCLLV +
K. lactis LLYVLLV + LNLCLLI +
CTG clade
C. albicans LIYLMLL + LNWYLLM +
C. dubliniensis LIYLMLL + LNWYLLM +
C. tropicalis LILYLLL + LNWYLLM +
C. parapsilosis LLYLMLL + LAWYLVM +
L. elongisporus LIYILIL + LNLYLI +
M. guilliermondii LIYILIL + LNLLFFS +
D. hansenii LVYIFLL + LNLLLFT +
Other fungi
A. nidulans LNLILL + LNLILLA +
S. pombe LVLCLLF + VNLILLM +
CDK5RAP2 & orthologues
Myomegalin & orthologues
Invertebrates
D. melanogaster LMLNLILQ + n.a. n.a.
Vertebrates
D. rerio YILNLILV + YILNLILV +
X. laevis FILNLILM + LLLNLILI +
H. sapiens FILNLILM + LLLNLILM +
Amoebozoans
D. discoideum MIYNLIML + n.a. n.a.
b
Available atomic model (PDB 6V6S, 6X0U)
Available atomic model overlaid with updated atomic model
Back view
(14)
(13)
(12)
(11)
(1)
Human γ-TuRC with CDK5RAP2CM1
90°
10°
Side view
(14)
(13)
(1)
Available atomic model
GCP2
CDK5RAP2CM1
Updated atomic model
GCP2
CDK5RAP2CM1
GCP2 (extended parts only)

Figure 29: The dimerised CM1 motif is evolutionarily conserved among different species

(a) The CM1 motifs in orthologues of Spc72/Spc110, CDK5RAP2/myomegalin from fungi to higher eukaryotes along the evolutionary tree. Plus represents the dimerisation and minus represents the non-dimerisation of the CM1 motif predicted by DeepCoil2. The predicted residues involved in the dimerisation of the CM1 motif were shown and the residues colored in red indicate the negative impact on CM1 dimerisation.

(b) The updated structural model of human γ-TuRC and CDK5RAP2^{CM1} after modification based on the previous atomic models (PDB 6V6S3[119] and 6X0V4[120], shown in light and dark grey) shows the interface of 'contact 1' between GCP2 and CDK5RAP2^{CM1}, which was found in *C. albicans* Spc72^{CM1} and Spc97 interfaces of 'contact 1' to 'contact 4' (**Fig. 26a,b**) but was not found in the available cryo-EM reconstruction (EMD 21985[120]) before. Only density segments corresponding to CM1 motif and their interaction elements are shown in the updated human structural model of γ-TuRC and CDK5RAP2^{CM1}.

Data in panels (**a and b**) were produced by Bram J.A. Vermeulen.

3.2.6 The dimerisation of CM1 is essential for the function of Spc72

Having seen the conservation of the dimerised CM1 motifs across different species, we also explored the function of dimeric Spc72^{CM1} both *in vitro* and *in vivo*. Three amino acids (L243/I247/L254) contributing to the dimerisation of CM1 motifs were mutated to arginine (Spc72$^{1-599}$ 3R mutant, referred to Spc72^{3R}) to disrupt the CM1 dimeric formation (Fig. 30a). Pull-down experiment was performed to test the binding of Spc72$^{1-599}$ and Spc72^{3R} with γ-TuSC, and it turned out that Spc72^{3R} mutant showed a slightly decreased binding efficiency to γ-TuSC compared to Spc72$^{1-599}$ (Fig. 30b). Since the overall binding ability between Spc72^{3R} with γ-TuSC was maintained, the γ-TuSC/Spc72^{3R}/FLAG-Stu2 mutant complex was co-expressed in insect cells and used for the oligomeric distribution analysis by SEC. The ratio of oligomeric γ-TuSC was drastically decreased (Fig. 30c,d), indicating that Spc72^{CM1} dimerisation is essential for the oligomeric γ-TuSC formation in *C. albicans*, either by impacting the binding with γ-TuSC or stability of the formed γ-TuSC oligomers.

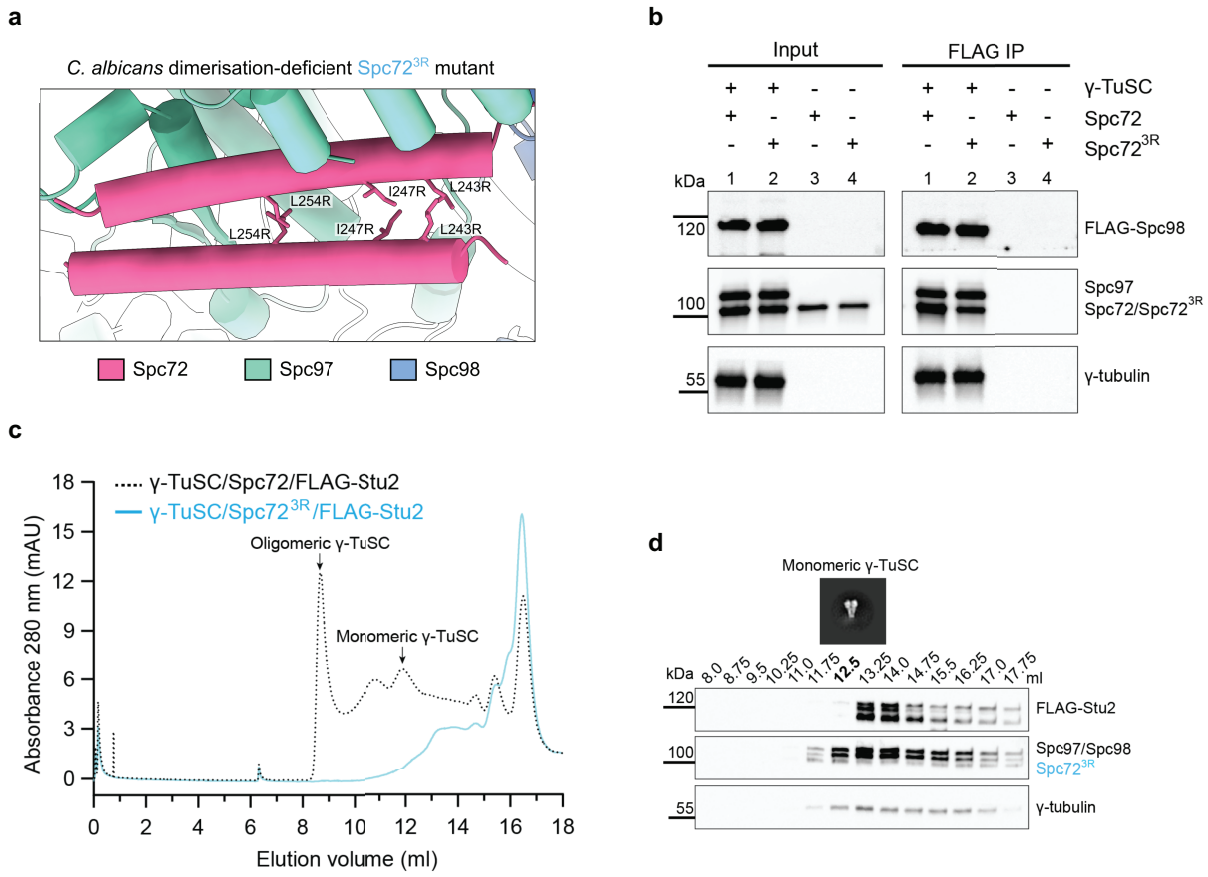

Figure 30: CM1 dimerisation is essential for γ-TuSC oligomerisation

(a) The positions of three mutations of L243R, I247R, and L254R in Spc72^{CM1} are reflected as six positions due to the dimeric CM1 motifs. The amino acid side chains are shown. The color scheme is indicated.

(b) Pull down of Spc72 and Spc72^{3R} with the FLAG-tagged-Spc98 γ-TuSC, showing the binding of Spc72^{3R} to the γ-TuSC is not strongly affected by the 3R mutation. Immunoblotting was performed with antibodies against FLAG-Spc98, His-Spc97/His-Spc72, and γ-tubulin.

(c) SEC chromatograms of γ-TuSC/Spc72/FLAG-Stu2 complex (black line) or the complex of γ-TuSC/Spc72^{3R}/FLAG-Stu2 (sky blue and dash line) show that disruption of CM1 dimerisation abrogates γ-TuSC oligomerisation. Fractions corresponding to monomeric and oligomeric γ-TuSCs are indicated with arrows.

(d) Western blotting result of γ-TuSC/Spc72^{3R}/FLAG-Stu2 in panel (**c**). Representative negative stain 2D classes for monomeric and oligomeric species γ-TuSCs highlight the oligomeric state of complexes in indicated fractions. Immunoblotting was performed with

antibodies against FLAG-Stu2, His-Spc97/His-Spc98/His-Spc72^{3R} and γ-tubulin. Western blot for γ-TuSC/Spc72/FLAG-Stu2 is shown in Figure. 26e. Experiments in panels **(b-d)** were performed independently twice.
Data in panel (**a**) were produced by Bram J.A. Vermeulen.
Data in panels (**b-d**) were produced by Anjun Zheng.

Meanwhile, to test the function of Spc72^{CM1} dimerisation *in vivo*, the 3R mutant (L67R/L71R/I78R, *spc72^{3R}*) based on sequence alignment was introduced in *S. cerevisiae* Spc72 (Fig. 31a). *spc72^{3R}* mutant cells in the S288c background were unable to complement the wild-type *SPC72* (Fig. 31b). The *spc72^{3R}* mutant cells in the W303 background showed a strong growth defect compared to wild-type *SPC72* (Fig. 31b). Moreover, the DAPI staining experiment shows approximately 89% of *spc72^{3R}* mutant cells accompanied by the obvious phenotypes of enlarged cell size, increased number of nuclei, and co-localization of nuclei in the mother cell body (Fig. 31c,d). To analyze phenotypes of *spc72^{3R}* mutant cells, *spc72^{3R}* mutant cells in the W303 background were used to trace signals of *TUB1-GFP* (MT marker) and *SPC42-mCherry* (SPB marker) and it turned out that these mutant cells were unable to arrange normal cytoplasmic MTs and spindle MTs (Fig. 31e). These phenotypes are consistent with a spindle position checkpoint (SPOC)-dependent cell cycle arrest of cells with misaligned anaphase spindle caused by defective cMTs[195]. In summary, Spc72^{CM1} dimerisation is essential for *C. albicans* γ-TuSC oligomerisation and the formation of functional cMTs in *S. cerevisiae*.

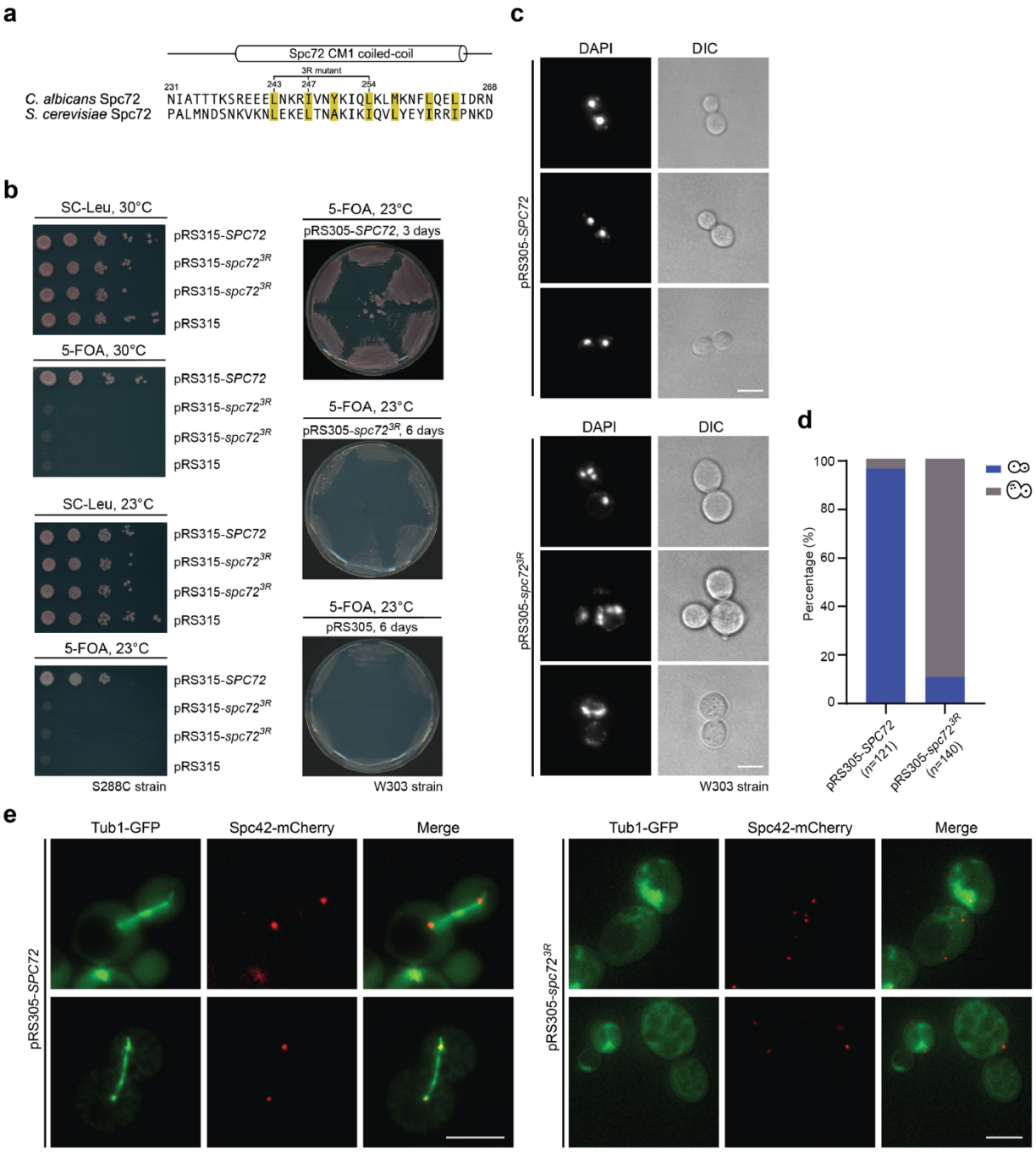

Figure 31: The CM1 dimerisation of Spc72 is indispensable for cell viability *in vivo*

(a) The amino acid sequence alignment between *C. albicans* and *S. cerevisiae* Spc72 CM1 motifs. The 3R mutant positions from these two fungi are relatively conserved with the amino acids from *C. albicans* Spc72 of L243, I247, and L254 marked on top. The relatively conserved residues are highlighted in yellow color.

(b) Viability test of wild-type *SPC72* or the *spc72*^{3R} mutant in budding yeast cells. Cells were grown at 30°C for 2 days or at 23ºC for 3 days. Viability tests were performed three times successfully.
(c) The *spc72*^{3R} mutant cells display enlarged cell size and mispositioning of the nuclei (DAPI staining regions) by using the DAPI-stained cells under microscopy. Scale bars, 5 µm. DIC = differential interference contrast. Phenotypic analysis was successfully performed in two independent replicates.
(d) Quantification of DAPI-stained nuclei in *SPC72* (n=121) and *spc72*^{3R} (n=140) cells. In *SPC72* cells, 98% of the cells show normal separation of nuclei in anaphase (dark blue); 2% have enlarged cell size and multiple nuclei (dark grey). In *spc72*^{3R} mutant cells, 11% of the cells showed normal separation of nuclei (dark blue); 89% of the cells had enlarged cell size and multiple nuclei (dark grey).
(e) *SPC72* and *spc72*^{3R} cells phenotype analysis cultured at 23°C. *TUB1-GFP* was used for tracing cytoplasmic and nuclear MT signals, whereas *SPC42-mCherry* was used for tracing of the SPB. Scale bar, 5 µm.
Data in panel (**a**) were produced by Bram J.A. Vermeulen.
Data in panels (**b-e**) were produced by Anjun Zheng.

3.2.7 Stu2 and γ-TuSC/Spc72 interaction is mediated by Spc72$^{430-480}$ and Stu2$^{894-924}$

Even after purifying the γ-TuSC using FLAG-Stu2, we were unable to detect a Stu2 density on the γ-TuSC oligomer complex via cryo-EM (Fig. 23a-c). We decided to analyze the binding mode between Stu2 and Spc72. According to a previous study, it is the coiled-coil region of Stu2$^{855-888}$ that interacts with Spc72 and Spc72 recruits Stu2 to the SPB in *S. cerevisiae*[167]. To better dissect the interaction between Stu2 and Spc72 in *C. albicans*, pull-down experiments combined with AlphaFold 2-based structural predictions were used to narrow down the Stu2 interacting regions on Spc72.
To verify the C-terminal region of Stu2 interacting with Spc72 in *C. albicans*, two Stu2 mutant proteins, Stu2$^{\Delta 666-768}$ and Stu2$^{\Delta 894-924}$, were constructed and expressed in insect cells (Fig. 32a). Accordingly, several mutant proteins of Spc72, Spc72$^{1-599}$, Spc72$^{1-239}$, Spc72$^{1-290}$, and Spc72$^{291-599}$ based on the predicted Spc72 structure scheme (Fig. 19a),

were constructed and expressed in *E. coli* cells (Fig. 32b). The first pull-down experiment of wild-type/mutated Stu2 and Spc72 showed it was Spc72$^{291-599}$ that interacted with Stu2$^{894-924}$ (Fig. 32c). To further narrow down the binding site of Stu2 within amino acids 291-599 on Spc72, AlphaFold 2 was used to predict the regions involved in the interaction between Stu2$^{894-924}$ and Spc72$^{291-599}$. The interacting regions predicted by AlphaFold 2 are mainly located at the Spc72 C-terminal side of the CM1 motif, which are two flexibly linked regions of the dimerised coiled-coil of aa 293-418 and 434-560 (Fig. 32d). Furthermore, the predicted two shorter helixes in Spc72 (aa 305-345 or 435-475) located in the longer coiled-coil regions of 293-418 and 434-560 are more likely to interact with Stu2$^{894-924}$ (Fig. 32d). To verify these predictions, the Spc72 fragments spanning the first or second coiled-coil module (aa 291-428 and 429-599), the two shorter coiled-coil helixes (aa 300-350 and 430-480), and as negative control Spc72$^{230-290}$ were constructed in pET28b vector. A GFP tag was fused to the N-termini of the Spc72 constructs (Fig. 32e). In this pull-down experiment, I observed interaction between wild-type Stu2 with Spc72$^{429-599}$ and Spc72$^{430-480}$ (Fig. 32f). In contrast, no clear binding bands were observed between Stu2$^{\Delta 894-924}$ and the Sp72 mutants (Fig. 32f). In short, our pull-down experiments have successfully narrowed down the interacting regions between Spc72 and Stu2 of Spc72$^{430-480}$ and Stu2$^{894-924}$.

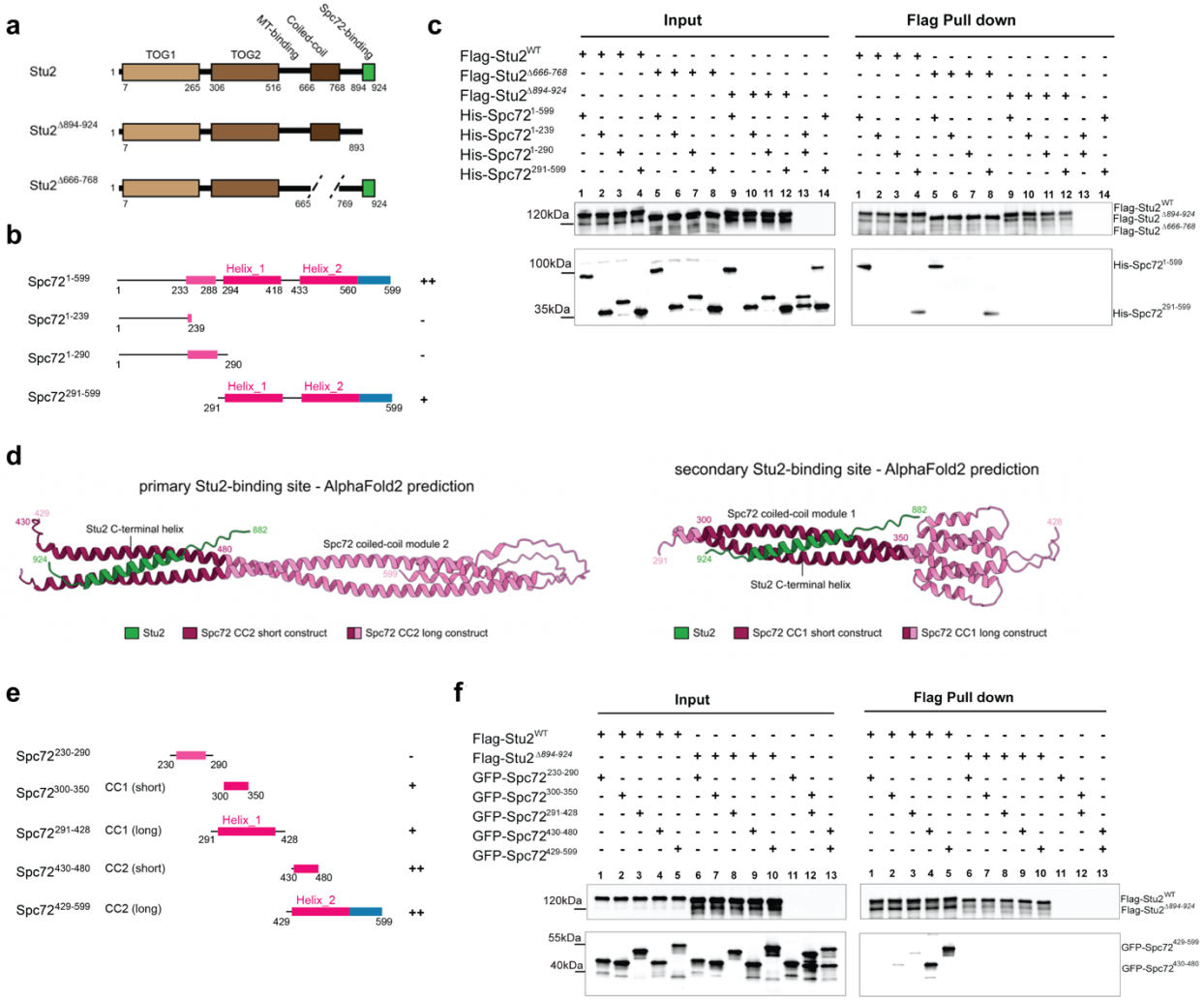

Figure 32: The pull-down experiment combined with AlphaFold 2 predictions narrowed down the interacting regions between Stu2 and Spc72

(a) The structure schemes of wild-type Stu2 and Stu2$^{\Delta 666-768}$ and Stu2$^{\Delta 894-924}$ mutants. TOG domains, MT-binding domain, coiled-coil, and Spc72 binding domain are shown in different colors.

(b) The structure schemes of Spc72$^{1-599}$, Spc72$^{1-239}$, Spc72$^{1-290}$, and Spc72$^{291-599}$ were produced based on Fig. 19a. Plus and minus represent the comparably binding affinities between Spc72 proteins and Stu2.

(c) The pull-down experiment of Stu2 (**a**) and Spc72 mutants (**b**). The FLAG tags are on Stu2 and Stu2 mutants. Only Spc72$^{1-599}$ and Spc72$^{291-599}$ were pulled down.

(d) The AlphaFold 2 predicted two long helixes of 293-418 and 434-560 aa (pink) and two

shorter regions of 305-345 or 435-475 aa (dark red) inside of the two long helixes on Spc72 interacting with the C-terminal helix of Stu2 (green).
(e) The structure schemes of Spc72$^{230-290}$, Spc72$^{300-350}$, Spc72$^{291-428}$, Spc72$^{430-480}$, and Spc72$^{429-599}$ based on the AlphaFold 2 prediction for the interactions between the C-terminal helix of Stu2 and Spc72 in (**d**), the plus and minus represent the comparably binding affinities among the Spc72 mutants with Stu2.
(f) The pull-down experiment of Stu2 (**a**) and Spc72 mutants (**e**). The FLAG tags are on Stu2 and Stu2 mutants. Spc72$^{291-428}$ and Spc72$^{430-480}$ were pulled down. Spc72$^{300-350}$ and Spc72$^{291-428}$ were slightly pulled down under the same condition.
Data in panels (**a-c, e, and f**) were produced by Anjun Zheng.
Data in panel (**d**) were produced by Bram J.A. Vermeulen.

When looking back to these two coiled-coil interactions on Spc72, the strongly negatively charged amino acids are featured on the surfaces providing electrostatic interactions with the positively charged Stu2 (Fig. 33b). Notably, the C-terminal helix of Stu2 interacting with Spc72 is well conserved among Stu2/CKAP5/XMAP215/chTOG homologs across fungi and higher eukaryotes (Fig. 33c).
In conclusion, our pull-down experiments combined with the AlphaFold 2-based structure predictions identified the region of interaction between Stu2 and Spc72 at the residual level. Correspondingly, we have proposed a model to better illustrate the process: Spc72 is important for the oligomerisation of the γ-TuSC ring and with the interaction with Stu2, Stu2 can be recruited to the MT nucleation unit at the cytoplasmic side. Concerning Stu2, the α/β-tubulin molecules delivered by Stu2 are anchored at the MT template of γ-TuSC rings. Since our structure revealed a ‘closed’ ring which might already be matched to the MT, we mainly consider that Spc72 plays an important role in oligomerizing the γ-TuSC into a ‘closed’ or a ‘near-closed’ γ-TuRC, and then through the binding of Stu2 and its bound α/β-tubulin, the 13-protofilament forms from the α/β-tubulins delivered by Stu2 can be perfectly matched to the closed γ-TuRC at the cytoplasmic side of the SPB (Fig. 33d). However, we cannot exclude conformational changes between the 13-protofilaments and the γ-TuRC when they are synergistically forming a comparably stable MT to support the growth of MTs at the cytoplasmic side of the SPB. Moreover, how Stu2 is involved in such

conformational changes and whether there are other components or modifications of the core proteins involved in this biological process, remains unclear.

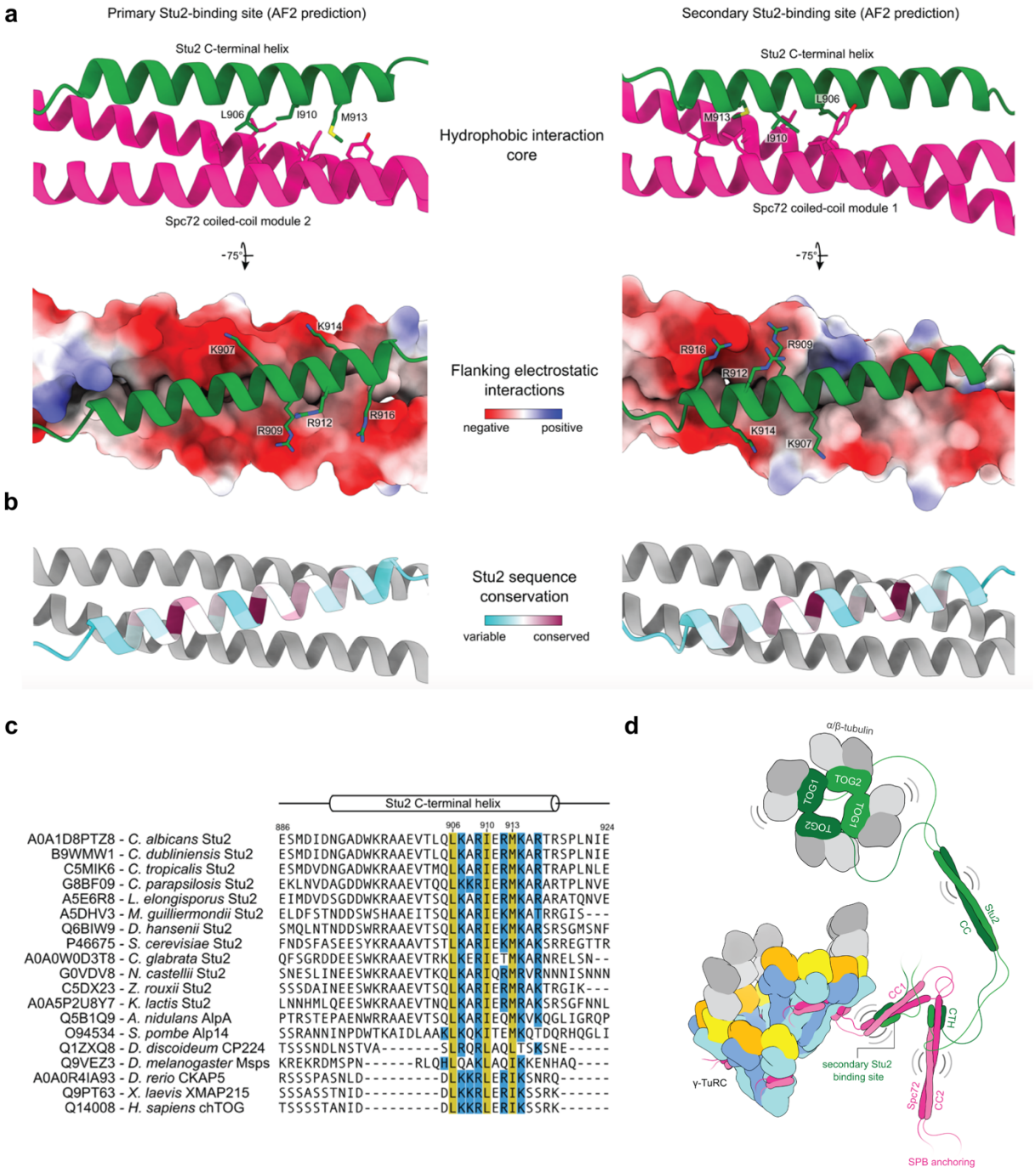

Figure 33: The properties of Stu2 and Spc72 interaction predicted by AlphaFold 2

(a) The hydrophobic and electrostatic interactions of Stu2 (green) and Spc72 (pink) coiled-coil modules 1 and 2 based on the AlphaFold2-predicted binding interfaces of

the primary and secondary binding sites in **Fig. 32d**, respectively. Conserved Stu2 residues are numbered.

(b) The Stu2 sequence conservation was mapped onto the AlphaFold 2-predicted binding interfaces of the primary and secondary binding sites on Spc72 (grey) based on (**a**). This mapping shows that conserved residues mainly face Spc72, while variable residues predominantly point away from the predicted interfaces. Sequence conservation of the C-terminal helix Stu2/Spc72 binding helix across different species.

(c) Sequence conservation of the C-terminal helix Stu2/Spc72 binding helix across different species. Conserved hydrophobic residues involved in the AlphaFold 2-predicted interface are highlighted in yellow, whereas positive charges are highlighted in blue. UniProt IDs are indicated.

(d) Model for the architecture of the MT nucleation unit. It shows how seven units of Spc72 binds to the γ-TuRC through the dimeric CM1 motifs and how seven units of Spc72 anchor Stu2 to the SPB. Only one Spc72 dimer and one unit of Stu2 with bound α/β tubulins are shown in detail.

Data in panels (**a-d**) were produced by Bram J.A. Vermeulen.

4 Discussion

The mechanism of MT nucleation is important for us to understand cell cytokinesis, cell migration, and cytoskeleton formation. In this study, I have been working with one of the simplest MT nucleation units, the γ-TuSC of *C. albicans*, and tried to understand the molecular basis and features of MT nucleation from the structural level. In conclusion, the work in this thesis has successfully solved two cryo-EM structures of the isolated and oligomeric γ-TuSCs from *C. albicans* in collaboration with Dr. Stefan Pfeffer's lab. The high-resolution atomic models of the monomeric and oligomeric γ-TuSC structures have enabled us to conduct functional experiments to verify some important amino acids and regions *in vivo* and to better understand the mechanisms of the oligomerisation of γ-TuSC in *C. albicans*. In addition to the structural information obtained from these two structures, the data allowed us to compare the differences in the MT nucleation units between yeast and higher eukaryotes, such as humans. This comparison provides insights into the evolutionary relationships and variations among these species.

4.1 The structural and functional analysis of *C. albicans* γ-TuSC

Our reconstituted *C. albicans* γ-TuSC in insect cells with the Bac-to-Bac Baculovirus Expression system has enabled us to pursue the structural analysis of this 300-kDa complex. The previous work performed with the *S. cerevisiae* γ-TuSC showed a 'Y'-shaped structure[142, 196] composed of two copies of Tub4p (the yeast γ-tubulin) and one each of the Spc97 and Spc98 proteins. A similar architecture was also observed in *C. albicans* γ-TuSC (Fig. 12a)[133]. In our study on *C. albicans* γ-TuSC, the oligomeric γ-TuSC was not identified, which means the addition of GTP is by itself not sufficient to trigger the oligomerisation of γ-TuSC because we have used elution buffer with GTP during the purification. Surprisingly, GDP-bound (GTP hydrolyzed by γ-tubulin) γ-tubulin was found in our γ-TuSC structure (Fig. 12d). The alignment of GDP-bound γ-TuSC with the MT spatial arrangement reveals a significantly different symmetry compared to the orientation in curved MTs. Instead, it aligns more closely with the symmetry of straight MTs (Fig. 12c). Furthermore, a similar conformation was observed in the *S. cerevisiae* γ-TuSC oligomer[141]. This suggests that the binding of γ-tubulin and the hydrolysis of GTP may

play a more crucial role in interacting with α/β-tubulins, rather than in the oligomerization and activation of the γ-TuSC[118].

However, when comparing the structures of *C. albicans* and human γ-TuSCs, we observed significant structural differences between the two systems. In the human γ-TuSC, the interactions between the GRIP1 domains of GCP2 and GCP3 are primarily dominated by electrostatic interactions. In contrast, the *C. albicans* γ-TuSC features more hydrophobic interactions between the GRIP1 domains of Spc97 and Spc98. Additionally, another significant difference is the markedly divergent interface between the Spc/GCP-γ-tubulin spokes. Specifically, the insertion loop (Asn626-Leu656) from the Spc98 GRIP2 domain (Fig. 14b) is important for the internal interaction of γ-TuSC (interaction with Spc97). Such an insertion loop is absent in human GCP3 which indicates different γ-TuSC assembly and regulation modes in different organisms.

Although the conformational plasticity of the *C. albicans* γ-TuSC was observed during cryo-EM data processing (Fig. 11b), this flexibility was negligible compared to the conformational changes required for γ-TuRC assembly and activation. Several factors could explain these phenomena: (1) The MT symmetry-matched γ-TuSC oligomer requires additional interactions with neighboring γ-TuSCs; (2) the phosphorylation of γ-TuSC components might be necessary to induce oligomerization, as suggested by previous studies[197-200]. (3) The other regulator factors such as Spc110/Pcp1/PcpA, Spc72/Mto1/ApsB, MZT1, XMAP215, CAMSAPs, chTOG, and TPX2 might be involved in the γ-TuSC oligomerisation and the activation of γ-TuRC in different species[133, 141, 147, 148, 160, 201, 202]. In *S. pombe*, the crystal structures of ctGCP3-NTD·ctMzt1 and ctGCP5-NTD·ctMzt1 presented the direct binding of Mzt1 with γ-TuRC, and the in vivo experiments indicate Mzt1 is involved in the SPB localization and MT nucleation of γ-TuRC[203]. What's more, the reconstituted Mto1/2, γ-TuSC, and Mzt1 complex (MGM complex) in *S. pombe* showed an increased γ-TuSC oligomerisation and MT nucleation activity *in vitro*[204]. In conclusion, the structural comparison of γ-TuSCs from different species has provided valuable insights into both the similarities and discrepancies at the atomic level across various systems. This comparison also highlights directions for future investigations such as the depletion of the MAP proteins or other proteins of interest, introducing the phosphorylation mutations on γ-TuSC and its receptor proteins and

analyzing the cell phenotypes by higher-resolution microscopy such as expansion microscopy[205] or using the cryo-ET technology[206] to do the in vivo structural modeling at the atomic level and with the wild-type cells as the control.

4.2 The structural and functional analysis of C. albicans γ-TuRC

Our reconstituted *C. albicans* γ-TuRC in insect cells with the MultiBac Expression system has enabled us to pursue the structural analysis of the γ-TuRC in the oligomeric structure unlike the monomeric one in section **3.1**. Three major interesting observations were obtained in this study. First, analysis of the whole reconstituted structure formed by γ-TuSC/Spc72$^{1-599}$/Stu2 indicated that it is the closed and thereby active ring complex even in the absence of attached MTs. Moreover, we also observed densities from Spc97 (Thr232-Asp272, Glu495-Pro502, Asn539-Ser566, and Ala686-Ile737) and Spc98 (Asn626-Leu656) which were not visible in the isolated γ-TuSC (Fig. 14a). This indicates that the stability of the entire structure could be achieved through interactions between neighboring γ-TuSCs.

Second, except for the interacting interfaces between the inter-γ-TuSCs, the most important contribution is from the dimeric CM1 motif bound to Spc97 (Fig. 25), which adopts a similar binding mode as the human CDK5RAP2 and γ-TuRC but different from the Spc110 binding to γ-TuRC in *S. cerevisiae*. The biochemical experiments of the pull-down experiment and the size-exclusive experiment showed a decreased binding affinity of Spc72$^{1-599:3R}$ mutant with γ-TuSC and the impaired γ-TuRC formation (Fig. 30b,c). The in vivo experiment performed in *S. cerevisiae* further verified the importance of the dimeric CM1 for cell viability and cell division which was reflected by the cell death in S288c strain (Fig. 31b), and the abnormal cell size, multi nuclei, defective nMTs, and cMTs in W303 stain (Fig. 31c). Due to the flexibility binding of Spc72 and γ-TuRC, only the region from 233-272 (within the assumed CM1 motif: 233-288) of Spc72 was visible by cryo-EM. Additionally, the more N-terminal side of the CM1 motif was found to be interacting with the neighboring γ-TuSC, which further proved the dimerised CM1 was important in promoting and stabilizing the γ-TuRC in *C. albicans*. Moreover, the two important amino acids of T234/T236 were also tested by SEC and the in vivo experiments with the results consistent with the structural finding (Fig. 26c), in which the PA-corresponding mutant

cells were viable (Fig. 27b) whereas the 3R mutant cells were inviable (Fig. 31b) in S288c background.

Third, even the density of Stu2 is missing from the structure of the γ-TuSC/Spc72$^{1-599}$/Stu2 complex which was surprising, considering that the purification method was via Stu2 and the Coomassie blue staining result showed a comparably higher content of Stu2. We then combined the pull-down experiment and the AlphaFold 2 prediction and decided the shorter region of Spc72$^{430-480}$ is mainly responsible for the interaction with the C-termini of Stu2 (Fig. 32d,f). Finally, with all the information we obtained from this study, a proposed model for the MT nucleation mechanism was depicted: the dimeric Spc72 binds to each γ-TuSC and promotes the oligomerisation of γ-TuSC by enhancing the interactions of the neighboring γ-TuSCs (the more N-terminal region of the CM1 motif interacting with the neighboring Spc98 (Fig. 26c)). In brief, the dimeric CM1 is doubling the interacting interfaces among the neighboring γ-TuSCs. Additionally, Spc72 recruits Stu2 and its bound α/β-tubulins to form a bridge between the α/β-tubulins and the γ-TuSC, facilitating the spatial arrangement necessary for MT localization onto the γ-TuSC (Fig. 33d).

Altogether, Spc72 guides γ-TuSCs and the α/β-tubulins-Stu2 complex to anchor at the cytoplasmic side of the SPB. Although the precise mechanism of MT nucleation remains to be investigated, studying the in vivo minus end at the cytoplasmic side could verify the binding mode of Stu2 to the minus end at the atomic level. To realize this, a strategy combining cryo-ET, cryo-EM, and AlphaFold prediction will be utilized.

In conclusion, our structure and biochemical information enabled us to propose the possible mechanism of the MT nucleation process at the cytoplasmic side. Due to the missing (it is undetectable) Stu2 density from the cryo-EM density map in our current database and the compromised resolution we could reach, the model is incomplete. However, with the native minus-end structure at the nuclear side in *S. cerevisiae* published recently, the authors found the additional densities bound to α/β and γ-tubulins from outside of MTs in minus-end from in vivo biological sample, and the mass spec data suggests one biggest possibility is the coiled-coils are from Stu2^{207}**.** The intriguing aspect is that the additional densities from the coiled coils are at low resolution, making it difficult to determine the origin of the protein. However, they could deplete Stu2 with a degron

system and check whether the density disappears. The problem here is that they use a yeast strain which is not suitable for genetic manipulations**.** Thus, optimizing SPB purification with the S288C or W303 background might be a strategy.

Based on the updated data combined with our findings, the hypothesis remains open: if these coiled-coils are from Stu2, it suggests that Stu2 may be involved in MT nucleation. The author used the CLMS and gel filtration to check the interaction of Stu2 and the yeast γ-TuRC components (Spc97/Spc98/Tub4 and $Spc110^{1–400}$) and found no direct interaction with γ-TuRC[207]. However, whether Stu2 can directly interact with Spc110, similar to its interaction with Spc72, remains unclear. Therefore, further investigation is needed to explore the interaction between Stu2 and Spc110 (the full-length of Spc110). Besides, several MAPs such as Kip1 and Cin8 (the kinesins) and components from kinetochore were also present in their CLMS result[207] and since Stu2 is also found at kinetochores and kinetochores are clustered at the SPB throughout the cell cycle[208, 209], which raises the question whether Stu2 can play a role in building a connection between the SPB components such as γ-TuRC and the kinetochore or not? To better answer the question, the *ndc10-1* cells could be used[210] because in these cells kinetochores are not assembled and detach from SPBs. Thus, using super-resolution microscopy, it can be tested whether Stu2 localizes to the nuclear side of the SPB in the absence of assembled kinetochores. If this is the case, it would support the model of direct Stu2 binding to Spc110.

Additionally, another possibility is that the coiled-coils might originate from Spc110. If this proves to be the case, obtaining more complete structures of the minus-ends at higher resolutions, both *in vitro* and *in vivo*, would be immensely beneficial.

Overall, with the advancement of cryo-EM and cryo-ET technologies, all the aforementioned puzzles are poised to be unraveled in the future. One widely accepted observation thus far is that the MT nucleation systems in certain yeast cells (*S. cerevisiae* and *C. albicans*) differ significantly from those in higher eukaryotic cells such as *Xenopus* and humans[2, 3, 119, 133, 141, 142]. This analysis not only sheds light on the evolutionary processes across the phylogenetic tree but also underscores the complexity of MT nucleation units in higher organisms.

In humans, MZT1 was found to be a linker between the intact γ-TuRC and the centrosome targeting factor of NEED1 and helps γ-TuRC targeting to centrosomes and MZT1 can bind not only to GCP3 but also other GCPs of GCP5/6 *in vivo*[123]. The human reconstituted γ-TuRC structure further verified the multi-binding mode of MZT1 to GCPs (GCP3/GCP5 and GCP6), especially for the MZT1-GCP3 module at the luminal bridge (stabilized by the GCP6 GRIP1-NTE), it might support stable 6-spoked core elements (GCP2/3-4/5-4-6) to recruit the rest of GCP2/3s to promote the full ring assembly of γ-TuRC in humans. However, for the function of the MZT1-GCP3 and MZT1-GCP5 modules on the outer surfaces of γ-TuRC, these MZT1s could be involved in the post-translational modification or the centrosome-localization regulator of γ-TuRC by releasing or binding to GCP3/5 from outside[121].

C. albicans MZT1, a homolog of human MZT1, was shown to enhance the MT nucleation activity together with γ-TuSC/Spc110N or γ-TuSC/Spc72N by 5-13 times compared with γ-TuSC alone *in vitro* by using the porcine brain α/β-tubulins. Additionally, *C. albicans* MZT1 and γ-TuSC can both bind $Spc72^{CM1}$, however, they bind to different amino acid residues on $Spc72^{CM1}$, which indicates the different binding modes and different roles that Spc72 and MZT1 play for the γ-TuRC assembly and stabilization.

Our study on the aspect of structural analysis of the negative stain EM result from the γ-TuSC/Spc72/MZT1 complex showed a low quality of the γ-tubulin ring complex particles (Fig. 20d), which could be due to the longer version of $Spc72^{1-599}$ used in our study whereas, in Tien-chen Lin's study, the shorter version of $Spc72^{1-420}$ was used[133], thus, what is the role of the N-terminal region of Spc72 plays in the interaction of MZT1 and γ-TuSC, remains to be explored. Moreover, in our structural analysis, γ-TuSC can be oligomerized into γ-TuRC in the absence of MZT1, which means MZT1 might be more involved in the γ-TuSC recruitment to the SPB as found in *S. pombe*, *Arabidopsis*, and *A. nidulans*[134, 211, 212].

On the nuclear side of SPB, $Spc110^{1-220}$, and γ-TuSC can assemble an open-state ring structure[141], which is different from the in vivo minus end structure in a closed state with additional density found on the outer surfaces of Spc98:γ-tubulin:α-tubulin subunits[207]. Whether in *C. albicans*, a closed minus end with Spc110 and the coiled coils bound exists at the nuclear side of the SPB remains to be determined. Additionally, the role of MZT1

in γ-TuRC assembly and activation at the nuclear and cytoplasmic sides is still unclear. In Tien-chen Lin's study, Spc110 has a higher binding affinity for γ-TuSC/MZT1 compared to γ-TuSC alone, unlike Spc72, which does not show this difference. This suggests slight variations in how γ-TuSC binds to Spc110 and Spc72 in the presence of MZT1.

In the future, conducting genetic deletion or mutation experiments *in vivo* and analyzing *C. albicans* using fluorescence microscopy and cryo-EM technology will help elucidate the role that MZT1 plays in γ-TuRC assembly, activation, and localization.

5 Materials and methods

5.1 Materials

Table 7 Instrument and equipment

Item	Company
Bio-Rad C1000 Touch® Thermal Cycler	Bio-Rad Laboratories, Inc.
Nanodrop® ND-1000	Thermo Fisher Scientific
Bio-Rad DNA Sub Cell	Bio-Rad Laboratories, Inc.
Microwave oven	SHARP
Ultrospec 2100 pro, UV/Visible Spectrophotometer	Amersham Biosciences
Gel-Doc XR Imaging System	Bio-Rad Laboratories, Inc.
FastGene B/G LED Transilluminator	NIPPON Genetic EUROPE, GmbH
Amersham Imager 600	GE Healthcare
LAS4000IR	FUJIFILM
Eppendorf Centrifuge 5810R, 5702R, 5424R, 5417R	Eppendorf AG
RC 6 Plus centrifuge	Sorvall
Discovery 90 SE centrifuge	Sorvall
Discovery M120 SE centrifuge	Sorvall
F9S 4x1000y	Thermo Fischer Scientific
Type 50.2 Ti	Beckman
Rotor S100AT4-606	Thermo Fischer Scientific
Sonicator UP50H	Hielscher
Luna-II®Automated Cell Counter	Logos Biosystem
Luna® Cell Counting Slide	Logos Biosystem

Item	Company
Neubauer improved cell counting	Paul Marienfield GmbH & Co. KG.
4-20% Mini-PROTEAN® TGX Stain-FreeTM Protein Gels, 10/15 well	BIO-RAD, 4568093, 4568096
Bio-Rad mini-PROTEAN® Tetra System	Bio-Rad Laboratories, Inc.
Bio-Rad PowerPac® HC	Bio-Rad Laboratories, Inc.
Bio-Rad Trans-Blot® Turbo Transfer System	Bio-Rad Laboratories, Inc.
Äkta go	Cytiva
Mono Q® 5/50 GL column	Cytiva
Superose 6 Increase 10/300 GL column	Cytiva
CanoScan 5600F	Canon
Deltavision RT microscope	Applied Precision, GE
Talos L120C	Thermo Fisher Scientific
JEOL JEM1400	Jeol
Vitrobot	Thermo Fisher Scientific
Glacios (200 kV)	Thermo Fisher Scientific
Titan Krios G1 (300 kV and Quanta GIF energy filter, 20 eV)	Thermo Fisher Scientific
200 mesh R2/1 holey carbon copper	Quantifoil
Whatman 50 filter paper	GE Healthcare, CAT No:1450-070
Filter 0.2µm/0.4µm	Whatman GE Healthcare Life Science
PVDF 0.45 µm	Millipore Merck
Amicon Ultra-0.5 30 kDa MWCO	MERCK UFC5030

Table 8 Software

Software	Company
SnapGene	GSL Biotech LLC
DNAStar Lasergene	DNAStar Inc.
Nanodrop 2000/2000c	Thermo Fisher Scientific
Fiji	Schindelin et al, 2012
ImageJ 1.46r software package	National Institutes of Health
MP Navigator EX	Canon
LAS4000IR	FUJIFILM, v2.1
Unicorn	Cytiva (Version 7.5)
EPU	Thermo Fischer Scientific (version 2.6, 2.9)
Gctf	Zhang et al., 2016 (version 1.06)
RELION	Zivanov et al., 2018 version 3.1
UCSF-Chimera	Pettersen et al., 2004 version 1.13.1)
PRISM	Graphpad (version 9.1/9.2)
Adobe Illustrator	Adobe

Table 9 Chemical

Item	Company
GelRed®	Biotium
Coomassie Brilliant Blue G250	Sigma Aldrich
DNA ladder, 1kb	New England Biolabs Gmbh
PageRuler™ Plus Prestained Protein Ladder	Thermo Fisher Scientific
ProfinityTM IMAC Ni-Charged Resin	Bio-Rad

Item	Company
Cellfectin® II	Thermo Fisher Scientific
FBS	Gibco by Life Technologies Ltd
Sf-900® III medium	Thermo Fisher Scientific
Penicillin Streptomycin	Gibco by Life Technologies Ltd
Trypan blue solution	Sigma-Aldrich, Lot # RNBJ7454
Benzonase®	Sigma-Aldrich
Anti-FLAG M2 Affinity Resin	Sigma-Aldrich
3x FLAG peptide	Gentaur Molecular Products BVBA
Trans-Blot Turbo RTA Mini 0.2 µm PVDF Transfer Kit	BIO-RAD Laboratories, Inc., 1704272
ClarityTM Western ECL Substrate Luminol/Enhancer solution	BIO-RAD Laboratories, Inc.
GTP (Guanidine Triphosphate)	AppliChem GmbH
BamHI	New England Biolabs (NEB)
NdeI	New England Biolabs (NEB)
XhoI	New England Biolabs (NEB)
Cre recombinase	New England Biolabs (NEB)

Table 10 Cell lines

Cell line	Source and detail
E.coli DH5α	Sigma-Aldrich
E.coli pirHC	Geneva-Biotech
E.coli DH10Multibac	Geneva-Biotech
E.coli DH10EmBacY	Geneva-Biotech

Cell line	Source and detail
E. coli BL21 CodonPlus-RIL	Stratagene
Sf9 insect cells (*Spodoptera frugiperda*)	Sigma-Aldrich
Sf21 insect cells (*Spodoptera frugiperda*)	EMBL protein expression facility

Table 11 Plasmids

Plasmid	Source
pACEBac1	MultiBac system GENEVA Biotech
pIDC	MultiBac system GENEVA Biotech
pIDK	MultiBac system GENEVA Biotech
pet28b	Novagen

Table 12 General buffers

Buffer	Content
6x DNA loading buffer	0.25% w/v Bromophenol blue, 0.25% w/v Xylene cyanol, 30%, v/v Glycerol
1x TAE	20 mM TRIS-Cl pH 7.5, 1 mM EDTA, adjusted with acetic acid
Minipreparation resuspension buffer (S1)	50 mM TRIS-Cl pH 8.0, 10 mM EDTA, 100 µg/ml RNase A (DNase free)
Minipreparation lysis buffer (S2)	200 mM NaOH, 1% SDS
Minipreparation neutralization buffer (S3)	2.8 M K-Acetate, pH5.1
LB-Medium (Luria/Miller) (C.Roth X968)	10 g/l Trypton, 5 g/l Yeast extract, 10 g/l NaCl, pH7.0 ±0.2

Buffer	Content
LB-Agar (Luria/Miller) (C.Roth X969)	10 g/l Trypton, 5 g/l Yeast extract, 10 g/l NaCl, 15 g/l Agar-Agar, pH7.0 ±0.2
2xYT-Medium (C.Roth)	16 g/l Trypton, 10 g/l Yeast extract, 5 g/l NaCl, pH7.0 ±0.2
1x TBS	10 mM TRIS-Cl pH8.0, 150 mM NaCl
1x TBS-T	10 mM TRIS-Cl pH8.0, 150 mM NaCl, 0.05% v/v Tween20
4x Lämmli buffer	200 mM TRIS-Cl, 40% (v/v) glycerol, 8% (w/v) SDS, 100 mM DTT, 0.08% (w/v)
1x SDS running buffer	25 mM TRIS-Cl, 192 mM Glycine, 0.1% (w/v) SDS
Coomassie staining solution	90 mg Coomassie Brilliant Blue G250, 3 ml HCl (37%) in 1 l H_20
Blotting buffer	25 mM TRIS-Cl, 192 mM Glycine, 0.25% (w/v) SDS, 20% (v/v) Methanol
Immunoblot blocking buffer	5% (w/v) nonfat dry milk in 1x TBS-T buffer

5.2 Molecular cloning

5.2.1 PCR amplification

Plasmids and DNA fragments of inserts were amplified by PCR following the standard protocol, the Q5 High-Fidelity DNA Polymerase Kit (NEB) was used for the targeted DNA amplification with the reaction system and the PCR thermocycler settings listed in Table 13 and Table 14. The NEBuilder Assembly Tool (https://nebuilder.neb.com/#!/) was used for primer design. All the primers used in the thesis are listed in Table 15.

Table 13 Composition of the PCR reaction mixture

Composition	Concentration	50 µl volume	100 µl volume
5X Q5 Reaction Buffer	1X	10 µl	20 µl
2 mM dNTPs	200 µM	5 µl	10 µl

Composition	Concentration	50 µl volume	100 µl volume
10 µM Forward Primer	0.5 µM	2.5 µl	5 µl
10 µM Reverse Primer	0.5 µM	2.5 µl	5 µl
Template DNA	< 10 ng	1 µl	1 µl
Nuclease-Free Water	1X	28.5 µl	58 µl
Q5 High-Fidelity DNA Polymerase	0.02 U/µl	0.5 µl	1 µl

Table 14 PCR program

Step	Temp	Time
Initial Denaturation	98°C	30 sec
25-35 Cycles	98°C 50-72°C* 72°C	10 sec 30 sec 20-30 sec/1kb
Final Extension	72°C	5 min
10 µM Reverse Primer	4°C	

The * indicates that the annealing temperature is adjusted according to the used primers.

Table 15 Primer list

Primer Name	Sequence (5' to 3')	Source
cTub4-pFB-F0	GTTTCGGTCTCCACGCATCG	this study
cTub4-pFB-R	TATTCCGGATTATTCATACCGTCCCAC	this study
cTub4-pFB-R	CTTTGAATTCCGCGCGCTTCG	this study
cTub4-T38-K71-F	GTCCGACGGGAGCTCATATAGAAATGATCATC	this study
cTub4-T38-K71-R	GATGATCATTTCTATATGAGCTCCCGTCGGAC	this study
cSpc98-pFBHTA-F	GATTACGATATCCCAACGAC	this study
cSpc98-pFBHTA-R	GTAGGCCTTTGAATTCCGGATC	this study

cSpc98-D627-K650-F	GCTTTTTTACAATAAAAATTTTAATGTTAATCTGTTG	this study
cSpc98-D627-K650-R	CAACAGATTAACATTAAAATTTTTATTGTAAAAAAGC	this study
Spc98-D674-H713-F	CGCCAGGGTTTTCCCAGTC	this study
Spc98-D674-H713-F1	CTGCAACGCACAGAGAATGCAATCGAAAAGACGCTG	this study
Spc98-D674-H713-R1	CAGCGTCTTTTCGATTGCATTCTCTGTGCGTTGCAG	this study
Spc98-D674-H713-R	CAGGAAACAGCTATGAC	this study
pFastbac1-FLAG-Stu2_Fwd	CCGTCCCACCATCGGGCGCGGATCCATGGATTACAA AGATGATGATGATAAGCTGGAAGTTCTGTTCCAGGGG CCCATGAGCACTGAAGAAGAAG	this study
pFastbac1-Stu2_Rev	TTCCGCGCGCTTCGGACCGGGATCTCATTCTATGTTC AGTGGAC	this study
pIDC-FLAG-Stu2_Fwd	TAAAAAAACCTATAAATATGGATTACAAAGATGATGATG	this study
pIDC-FLAG-Stu2_Rev	TCGAGACTGCAGGCTCTAGATCATTCTATGTTCAGTGGA	this study
pET28b-Spc72_Fwd	CTGGTGCCGCGCGGCAGCCATATGTCGAACTTAAGTATCAATG	this study
Spc72-Thr426_Rev	AGTAAAGAGGTCGTGTGGTTTATTATTGTACTGATG	this study
Spc72-Arg410_Fwd	CGTCTGGATCAGTCACATCAGTACAATAATAAACCAC	this study
pET28b-Spc72_Rev	AGTGGTGGTGGTGGTGGTGCTCGAGTCAGTTATTGTCGTTCGTGGTC	this study
pIDS-Spc72$^{1-599}$_Fwd	AAAACCTATAAATATGCATCATCATCATCAT	this study
pIDS-Spc72$^{1-599}$_Rev	GACTGCAGGCTCTAGACTAGTTGAGCTCATTG	this study
MultiBac_vector_fwd	TCTAGAGCCTGCAGTCTCG	Würtz et al., 2021[213]
MultiBac_vector_rev	ATATTTATAGGTTTTTTTATTACAAAACTG	Würtz et al., 2021
pACEBac1-His-Spc97_Fwd	AAAACCTATAAATATGTCGTACTACCATCA	this study
pACEBac1-His-spc97_Rev	ACTGCAGGCTCTAGACTATTCTGGAAAGCA	this study
pIDC-Spc98_Rev	GACTGCAGGCTCTAGACTACAGTAATTTACTC	this study
pIDK-Tub4-Fwd	AAAACCTATAAATATGCCAGGTGAAACA	this study
pIDK-Tub4-Rev	ACTGCAGGCTCTAGACTAAATACCCATATC	this study
Combination_vector_fwd	TTCGCGACCTACTCCGGA	Würtz et al., 2021

Combination_vector_rev	CAGATAACTTCGTATAATGTATGCT	Würtz et al., 2021
Combination_insert_fwd	ATACGAAGTTATCTGTTCGCGACCTACTCCGGA	Würtz et al., 2021
Combination_insert_rev	GGAGTAGGTCGCGAAGATCCAGACATGATAAGATAC ATTG	Würtz et al., 2021
pACEBac1-FLAG-Spc97_Fwd	TAAAAAAACCTATAAATATGGATTACAAAGATGATGAT GATAAGCTGGAAGTTCTGTTCCAGGGGCCCATGAATA CGTTCTCCTCTC	this study
pACEBac1-FLAG-Spc97_Rev	TCGAGACTGCAGGCTCTAGACTATTCTGGAAAGCACA ATTC	this study
pIDC-Spc98_Fwd	TAAAAAAACCTATAAATATGGCTCTGAACAAAGTG	this study
pIDC-FLAG-Spc98_Fwd	TAAAAAAACCTATAAATATGGATTACAAAGATGATGAT GATAAGCTGGAAGTTCTGTTCCAGGGGCCCATGGCT CTGAACAAAGTG	this study
pFastbac1-FLAG-Spc98_Fwd	TCCCACCATCGGGCGCGGATCCATGGATTACAAAGA TGAT	this study
pIDC-GFP-Mzt1_Fwd	TAAAAAAACCTATAAATATGGTGAGCAAGGGCGAGGA	this study
pIDC-GFP-Mzt1_Rev	AGACTGCAGGCTCTAGATCAGTGGTGGTGGTGGT	this study
pIDS-Spc72$^{1\text{-}599:PA}$_Fwd	TAAAAAAACCTATAAATATGCACCACCACCACCACCAT TC	this study
pIDS-Spc72$^{1\text{-}599:PA}$_F1	ACAAAAGAATCGTCAACTACAAAATCCAACTTAAATTA ATG	this study
pIDS-Spc72$^{1\text{-}599:PA}$_R1	CATTAATTTAAGTTGGATTTTGTAGTTGACGATTCTTTT GT	this study
pIDS-Spc72$^{1\text{-}599:PA}$_Rev	TGTCGAGACTGCAGGCTCTAGACTAGTTGAGCTCATT GAGGGA	this study
pIDS-Spc72$^{1\text{-}599:3R}$_F1	TGATAGATCGTAATAACCTAGACCCGCATGAGTTTCA CAC	this study
pIDS-Spc72$^{1\text{-}599:3R}$_R1	GTGTGAAACTCATGCGGGTCTAGGTTATTACGATCTA TCA	this study
pFastbac1-FLAG-Stu2_F1	GTCCCACCATCGGGCGCGGATCCATGGATTA	This study
pFastbac1-FLAG-Stu2$^{\Delta 894\text{-}924}$_Fwd	GTCCCACCATCGGGCGCGGATCCATGGATTA	this study
pFastbac1-FLAG-Stu2$^{\Delta 894\text{-}924}$_Rev	CGCTTCGGACCGGGATCcTCATCCATTGTCAATGTCC AT	this study

pFastbac1-FLAG-Stu2$^{\Delta 666-768}$_Fwd	AGCTCAGTCACTAATGAAGAAGTTAACATCAGTTCCAGCAATTCCA	this study
pFastbac1-FLAG-Stu2$^{\Delta 666-768}$_Rev	TGGAATTGCTGGAACTGATGTTAACTTCTTCATTAGTGACTGAGCT	this study
pET28b-Spc72$^{1-599}$_Rev	AGTGGTGGTGGTGGTGGTGCTCGAGTCAGTTGAGCTCATTGAGGGAAG	this study
pET28b-Spc72$^{1-239}$_Rev	TGGTGGTGGTGGTGCTCGAGTCAACGCGATTTAGTCGTG	this study
pET28b-Spc72$^{1-290}$_Rev	TGGTGGTGGTGGTGCTCGAGTCACTCGTTGTTCATGATGT	this study
pET28b-Spc72$^{291-599}$_Rev	TGCCGCGCGGCAGCCATATGAATAATCCGCTGTCGAC	this study
pRS315_Fwd	TAGTTATTTGCGGTGACTCGAG	this study
pRS315_Rev	CATGGATCCACTAGTTCTAGA	this study
Spc72_F1	GCTCTAGAACTAGTGGATCCA	this study
Spc72_R1	CTCGAGTCACCGCAAATAACTA	this study
Spc72^{3R}_F2	CAAGTACTCTATGAATACATTCGCAGAATC	this study
Spc72^{3R}_R2	GATTCTGCGAATGTATTCATAGAGTACTTG	this study
SPC72$^{\Delta P55-N62}$_F2	TCATAACGATCCCATCAAGAACAAAGTCAAAAATTTGGA	this study
SPC72$^{\Delta P55-N62}$_R2	TCCAAATTTTTGACTTTGTTCTTGATGGGATCGTTATGA	this study
pET28b-GFP-Fwd	CGGGATCCGAATTCGAGCT	this study
pET28b-GFP-Rev	CCCCTGGAACAGAACTTC	this study
pET28b-GFP-Spc72$^{230-290}$_Fwd	GAAGTTCTGTTCCAGGGGCCAATGAACAATATCGCGACCA	this study
pET28b-GFP-Spc72$^{230-290}$_Rev	AGCTCGAATTCGGATCCCGCTCGTTGTTCATGATGT	this study
pET28b-GFP-Spc72$^{300-350}$_Fwd	GAAGTTCTGTTCCAGGGGCCAATGCAAACATCTACTCTG	this study
pET28b-GFP-Spc72$^{300-350}$_Rev	CTCGAATTCGGATCCCGAATGCGGCTTTCGTAGT	this study
pET28b-GFP-Spc72$^{291-428}$_Fwd	GAAGTTCTGTTCCAGGGGCCAATGAATAATCCGCTGTCGA	this study
pET28b-GFP-Spc72$^{291-428}$_Rev	AGCTCGAATTCGGATCCCGTGGCGGAGTAAAGAGGT	this study

pET28b-GFP-Spc72$^{430-480}$_Fwd	GAAGTTCTGTTCCAGGGGCCAATGACCAGTAGCGAGTA	this study
pET28b-GFP-Spc72$^{430-480}$_Rev	AGCTCGAATTCGGATCCCGGTTTTGCAATTCATTTTTG	this study
pET28b-GFP-Spc72$^{429-599}$_Fwd	GAAGTTCTGTTCCAGGGGCCAATGTACACCAGTAGCGAGT	this study
pET28b-GFP-Spc72$^{429-599}$_Rev	CTCGAATTCGGATCCCGGTTGAGCTCATTGAGGGA	this study

5.2.2 DNA gel electrophoresis

The PCR-amplified DNA products were run on an agarose gel. The DNA agarose gel was prepared with 1% agarose (w/v) (Biozym) dissolved in 1xTAE buffer in a microwave oven. When the solution cooled down to 50-60°C, GelRed® (Biotium) was added at a dilution of 10,000 times and mixed well. The DNA products were then run at a constant voltage of 160 V, with 1 kb GeneRuler (Thermo Scientific) as a size marker. The DNA fragments were then isolated by using a scalpel upon visualization with an LED Transilluminator. The Bio-Rad machine (Gel Doc XR) was used for visualizing DNA fragments via ultraviolet light which was not used for the DNA isolation from the gel. DNA fragments excised from agarose gels were extracted using a Qiagen gel extraction kit following the instructions of the manual.

5.2.3 DNA Assembly and Cre-recombination

The sources of the gene fragments were synthesized and ordered (IDT USA and TWIST BIOSCIENCE) or generated with the mutations, truncations, and tags with PCR. The gel extraction kit (QIAquick Gel Extraction Kit) was used to obtain the purified DNA, the InFusion/NEBuilder Hifi assembly kit (New England Biolabs®) was used for the DNA fragment assembly. For the ligation assembly, the corresponding restriction enzymes of *BamHI*, *NdeI*, and *XhoI* (NEB) were used (1 µl in 50 µl PCR reaction) and the mixture was incubated for 1 h at 37°C to obtain the enzymatically digested and linearized PCR or plasmid products. For the plasmids used in the MultiBac system, the Cre-recombinase was used with the instruction of the MultiBac Manual version 5.1 (Geneva Biotech). In

short, 1-2 µg plasmids were added in an equal ratio of 1:1 with 1.5 µl of Cre-recombinase (NEB) in a 20 µl reaction volume and then incubated for 1 h at 37°C.

5.2.4 The assembled DNA and Cre-recombined product transformation

The InFusion/NEBuilder Hifi assembled DNA fragments and the Cre-recombined products were generally transformed into *DH5α* competent cells. Whereas for the MultiBac system (Geneva Biotech, MultiBac manual version 5.1), the assembled DNA fragments containing pIDK, pIDC, and pIDS were transformed into *pirHC* cells, only DNA fragments assembled with pACEBac1 were transformed into *DH5α* competent cells. DH10MultiBac^{TM}/DH10EmBacY cells were used for bacmid production. For transformation, the competent *E. coli* cells were defrosted on ice for 15-20 min, and then ~ 2 - 8 µl DNA product from the InFusion/NEBuilder Hifi assembly reaction, or 18 µl Cre-recombined products were used for transformation into *DH5α* competent cells; ~ 100 ng - 1000 ng plasmids were used for transformation into DH10Mbac/DH10MbacY for the bacmid production. After the incubation of the DNA and the competent cell for 20 - 30 min on ice, cells were heat-shocked at 42°C for 30 sec and immediately put onto the ice and incubated for 2 min. Then, 500 - 800 µl of LB medium without antibiotics was used for the cell recovery at 37°C for 1 h. The recovery time is longer (8 - 10 h) at 37°C for the Cre-recombined products and the transformation into DH10MultiBac/DH10EmBacY. After cell recovery, the cells were plated on LB plates with the respective antibiotics. All the competent cells were prepared by Ursula Jäkle with the protocol based on the principle that calcium chloride and heat-shock treatment can promote bacteria cells to uptake up DNA from the surrounding environment[214]. The competent cells were aliquoted, flash-frozen in liquid N_2 and stored at -80°C for long-term usage.

5.2.5 The plasmid and bacmid purification

The S1/S2/S3 buffers (Table 12) were used for plasmid and bacmid purification. Briefly, 300 µl S1 buffer was used for cell lysis and added to the 5 ml cell pellet with thorough resuspension. Then, 300 µl S2 buffer was added and mixed gently by 5 – 7 times rotation. Next, 350 µl S3 buffer was added to precipitate the protein, cell membrane, lipids, and chromosomal DNA. 5 - 7 rotations were required to mix the solutions. The samples were

centrifuged at 14,000 rpm for 15 min at 4°C to isolate the supernatant and precipitation. After centrifugation, the supernatant (700 µl) was transferred to a fresh Eppendorf tube (1.5 ml), and 600 µl of isopropanol was added and thoroughly mixed. The samples were again centrifuged at 14,000 rpm for 15 min at 4°C. After the second centrifugation, the DNA was pelleted down and 500 µl ice-cold 70% ethanol was added to the pellet after removing the supernatant to wash the DNA. The DNA with 70% ethanol was again centrifugated at 14, 000 rpm for 5 min and the wash step with 70% ethanol was repeated 1 more time. After the second time of centrifugation, the ethanol was removed by aspiration and the samples were placed at room temperature with the Eppendorf tube caps open to dry the DNA pellet, and ~ 50 µl of ultrapure water was used to dissolve the DNA.

For the bacmid preparation, the samples were transferred to a sterile hood after the second centrifugation to remove the isopropanol, and bacmid DNA was then washed twice with 70% ethanol to avoid contamination. The NanoDrop® spectrophotometer was then used for the DNA concentration measurement. After concentration measurement, the purified DNA was sent for sequencing to the company Microsynth (https://www.microsynth.com/). For confirming the bacmid, the PCR was used for the successful insertion verification. All the plasmids generated in this thesis study are listed in Table 16.

Table 16 Plasmid list

Baculovirus insect cell expression constructs	Plasmid
pZAJ-1	pFastbac-HTA-*HIS-SPC98*$^{\Delta D627\text{-}K650}$
pZAJ-2	pFastbac1-*Tub4*$^{\Delta T38\text{-}K71}$
pZAJ-47	pIDC-*FLAG-STU2*
pZAJ-48	pACEBac1-*HIS-SPC97*
pZAJ-49	pIDC-*HIS-SPC98*
pZAJ-66	pACEBac1-*HIS-SPC97*/*HIS-SPC98*
pZAJ-50	pIDK-*TUB4*
pZAJ-51	pIDS-*SPC72*$^{1\text{-}599}$
pZAJ-70	pIDK-*TUB4*/*SPC72*$^{1\text{-}599}$
pZAJ-73	pIDS-*SPC72*$^{1\text{-}599:PA}$

pZAJ-74	pIDS-*SPC72*$^{1\text{-}599:3R}$
pZAJ-75	pIDK-*TUB4*/*SPC72*$^{1\text{-}599:PA}$
pZAJ-76	pIDK-*TUB4*/*SPC72*$^{1\text{-}599:3R}$
pZAJ-82	pACEBac1-*FLAG-SPC97*
pZAJ-62	pIDC-*SPC98*
pZAJ-83	pACEBac1-*FLAG-SPC97*/*SPC98*
pZAJ-81	pIDC-*GFP-MZT1*
pZAJ-44	pFastbac1-*FLAG-STU2*
pZAJ-104	pFastbac1-*FLAG*-STU2$^{\Delta 666\text{-}768}$
pZAJ-105	pFastbac1-*FLAG-STU2*$^{\Delta 894\text{-}924}$
pZAJ-107	pFastbac1-*FLAG-SPC98*
***E. coli* constructs**	**Plasmid**
pZAJ-35	pET28b-*STU2*
pZAJ-45	pET28b-*SPC72*
pZAJ-57	pET28b-*SPC72*$^{1\text{-}599}$
pZAJ-87	pET28b-*SPC72*$^{1\text{-}239}$
pZAJ-88	pET28b-*SPC72*$^{1\text{-}290}$
pZAJ-89	pET28b-*SPC72*$^{291\text{-}599}$
pZAJ-97	pET28b-*GFP-SPC72*$^{230\text{-}290}$
pZAJ-98	pET28b-*GFP-SPC72*$^{300\text{-}350}$
pZAJ-99	pET28b-*GFP-SPC72*$^{291\text{-}428}$
pZAJ-100	pET28b-*GFP-SPC72*$^{430\text{-}480}$
pZAJ-101	pET28b-*GFP-SPC72*$^{429\text{-}599}$
***S. cerevisiae* strain constructs**	**Plasmid**
pZAJ-3	pRS425-*SPC98*$^{\Delta D674\text{-}H713}$
pZAJ-91	pRS315-*SPC72*
pZAJ-92	pRS315-*SPC72*$^{\Delta P55\text{-}N62}$
pZAJ-93	pRS315-*SPC72*^{3R}
pZAJ-94	pRS305-*SPC72*
pZAJ-95	pRS305-*SPC72*$^{\Delta P55\text{-}N62}$
pZAJ-96	pRS305-*SPC72*^{3R}

5.3 Protein expression

5.3.1 Recombinant baculovirus production in insect cells

After bacmid purification, the freshly purified bacmid DNA was used for the transinfection into the Sf9 cells. In brief, a 6-well plate was inoculated with 1 ml of the Sf9 cells at the cell density of ~ 1.0 x 10^6/ml for each well. After cells settled down, the medium was changed with 2 ml of SF900 III medium (Thermo Fisher Scientific) supplemented with 1.5% fetal bovine serum (FBS, Gibco). During the cell plating, the freshly prepared bacmid DNA (6 - 8 µl) was mixed with 100 µl SF900 medium. 8 µl of Cellfectin® II (Invitrogen, Thermo Fisher Scientific) was in the meantime mixed with 100 µl SF900 medium. Both mixtures were added to make a final solution with a volume of ~ 216 µl for an incubation time of 20 - 30 min at RT. After incubation, the bacmid DNA with the transfection reagent (~ 216 µl) was dropped into two plated cell layers (2 wells in a 6-well plate). After 3 - 5 h incubation at 27°C, the medium was changed to SF900 III medium supplemented with antibiotics of 100 units/ml Penicillin and 100 units/ml Streptomycin (Gibco), and 10% FBS. Another 72 h were required for the cell incubation to obtain the P1 baculovirus. For the P1 baculovirus harvest, the cells were centrifugated at 800 x g for 5 min and the supernatant (P1 baculovirus) was stored and protected from light at 4°C until further usage (storage time should be controlled to max. 1 month).

For P2 baculovirus production, 1 ml of P1 baculovirus was added to 30 ml of Sf9/Sf21 cells at a cell density of ~1.0 x 10^6/ml and the cell density was followed every day after the P1 baculovirus addition to the cells. The cells were cultured in suspension in flasks. Once the cell size increased and the cell number was unchanged, the P2 baculovirus was harvested after another 48 h incubation period. The P2 baculovirus was supplemented with 5% FBS and then stored and protected from light at 4°C until further usage (storage time should be max. 1 month).

For the insect cell of Sf9 and Sf21 culturing, the Sf900 III medium supplemented with antibiotics of 100 units/ml Penicillin and 100 units/ml Streptomycin (Gibco) were used for the cell passage. Cell splitting was performed every 2 days. Luna II (Logos Biosystems), or Neubauer counting chamber (0.1 mm, Profondeur) was used for cell counting, and

Trypan blue (Sigma-Aldrich) was used to determine for cell viability. The general insect cell passage and storage was done by Ursula Jäkle.

5.3.2 Recombinant protein expression in insect cells

After the P2 baculovirus was obtained, the P2 baculovirus was used to infect a larger amount of cells. For the Bac-to-Bac® Baculovirus Expression System (Invitrogen life technologies), three (maximum number) independently produced baculoviruses were pooled and Sf21 cells (~ 1.0 - 1.5 x 10^6/ml) were infected. The baculovirus to cell volume ratio was 1:100. The infected cells were cultured in the shaker at 27°C for 60-70 h and cells were harvested (800 x g for 5 min), flash frozen in liquid N_2 and stored at -80°C until further usage. Expression volumes varied from 50 - 800 ml according to the experimental purpose.

5.3.3 Protein expression in *E. coli* cells

After plasmid purification from DH5a cells and confirmed from the DNA by sequencing, the plasmid was then transformed into *E. coli* BL21 CodonPlus-RIL (Stratagene) and the positive colonies were sculptured from the plate and inoculated into the LB medium containing the appropriate antibiotics in a volume of 5 ml cultured overnight. After that, 5 ml cells were added to 1 l cells in 2xYT medium, and cells were cultured at 37°C for 3-5 h. The cell density was tested with the spectrophotometer (Amersham Biosciences) until the OD_{600} value reached 0.6-0.8, and the cells were taken out from the shaker and placed at RT for 20-30 min to cool them down. Then, 0.5 mM isopropyl-ß-D-thiogalactopyranoside (IPTG) was added and the cells were cultured for another 16-20 h at 18°C. The cells were centrifugated, pelleted, aliquoted, and flash-frozen as popcorn in liquid N_2 and stored at -80°C for further usage.

5.4 Protein purification

5.4.1 Purification of wild-type and mutant *C. albicans* γ-TuSCs

The wild-type and mutant *C. albicans* γ-TuSCs were expressed in Sf21 insect cells using the Bac-to-Bac® Baculovirus Expression System (Invitrogen life technologies) and the

bacmid preparation, the baculovirus production and protein expression were performed according to previous studies[3, 133]. Briefly, pFastBac plasmids containing wild-type *SPC97*, wild-type *SPC98*, wild-type *TUB4*, mutant *SPC98*$^{\Delta D627\text{-}K650}$, or mutant *TUB4*$^{\Delta T38\text{-}K71}$ were transformed into competent DH10Bac™ cells (obtained from Prof. Imre Berger, Grenoble) to isolate the recombinant bacmid DNA colonies (white color) cultured on plates containing antibiotics (kanamycin, gentamicin, and tetracycline), X-gal and IPTG for white/blue detection. The protocol for the bacmid trans-infection and protein expression in Sf21 cells is described in section 4.3.

Cells containing wild-type γ-TuSC (Spc97/Spc98/Tub4) or mutant γ-TuSC of Spc97/Spc98$^{\Delta D627\text{-}K650}$/Tub4 and Spc97/Spc98/Tub4$^{\Delta T38\text{-}K71}$ were lysed in RSB buffer (10 mM Tris-Cl pH 7.4, 10 mM NaCl, 1.5 mM $MgCl_2$, 1 mM DTT, 250 µM EGTA, and one Roche inhibitor tablet/50 ml). The cell lysate was then centrifuged under the speed of 179,000 × g at 4°C for 35 min (SORVALL Discovery 90SE ultracentrifuge, 50.2 Ti rotor), after centrifugation, the supernatant was incubated with Protino® Ni-TED Resin (MACHEREY-NAGEL) for 1 h at 4°C, and protein was eluted with 500 mM Imidazole. The sample was further purified by anion-exchange chromatography and the eluted proteins from His purification were loaded onto the Mono Q® 5/50 GL column (GE Healthcare). The used buffers are listed in Table 17. The protein peaks from the MonoQ chromatogram were verified by SDS-PAGE and used for negative stain EM.

5.4.2 Purification of *C. albicans* complexes containing γ-TuSC, Spc72, Stu2 or Mzt1

As mentioned in section **4.3**, the MultiBac system was used for obtaining the multi-bacmid plasmids. By using the PCR, InFusion/NEBuilder Hifi assembly and Cre-recombination, 5 different multi-bacmid plasmids were obtained: **(1)** γ-TuSC/Spc72$^{1\text{-}599}$/FLAG-Stu2; **(2)** γ-TuSC/Spc72$^{1\text{-}599:3R}$/FLAG-Stu2; **(3)** γ-TuSC/Spc72$^{1\text{-}599:PA}$/FLAG-Stu2; **(4)** γ-TuSC$^{FLAG\text{-}Spc97}$/Spc72$^{1\text{-}599}$/GFP-MZT1 and **(5)** γ-TuSC$^{FLAG\text{-}Spc97}$/Spc72$^{1\text{-}599}$.

The cells containing different combined complexes from (1) to (5) were resuspended in TBS buffer (50 mM Tris-Cl, pH7.4; 150 mM NaCl, 1 mM $MgCl_2$, 1 mM EGTA) supplemented with 1 mM DTT, 0.05% Tween-20 (vol/vol), and one complete EDTA-free protease inhibitor tablet (PI tablet, Roche) per 50 ml. The cell suspension was then lysed

by sonication (Polytron PT3100, 4000 rpm for 4 min) and incubated with Benzonase (1:500 vol/vol) for 20 min. After sonication, the cell lysate was centrifuged at 45 000 rpm for 35 min (Sorvall Discovery 90SE ultracentrifuge, 50.2 Ti rotor). Then, the supernatant was incubated with Anti-FLAG M2 Affinity Gel (Sigma-Aldrich) for 2 h at 4°C, and 500 µg/ml 3 × FLAG peptide (Gentaur) in TBS buffer was used for protein elution with the elution time of 20 min, and the beads was washed for 3 times with the Wash buffer (50 mM Tris-Cl, pH7.4, 150 mM NaCl, 1 mM MgCl2, 1 mM EGTA and one PI tablet per 50 ml) before elution. The samples from eluate were analyzed by SDS-PAGE. The protein (containing 2.5% glycerol in a final concentration) was flash-frozen in liquid N2 and stored at −80°C until further use.

5.4.3 Anion exchange chromatography and size exclusion chromatography

The anion exchange as mentioned in section **4.4.1** was used for further polishing of the wild-type and mutant *C. albicans* γ-TuSCs. The Mono Q® 5/50 GL column was connected to the ÄktaGo instrument (Cytiva) with Unicorn software (version 7.6) installed on the operating computer. The column was firstly washed with the high salt buffer (Buffer B, Table 17) to remove the non-specifically bound proteins, then equilibrated with low salt buffer (Buffer A, Table 17) twice by following the Mono Q® 5/50 GL manual. The purification was executed at a flow rate of 0.4 ml/min and proteins were eluted with a salt gradient ranging from 20 mM NaCl (Buffer A) to 1 M NaCl (Buffer B) over 20 column volumes.

The size exclusion chromatography (SEC) was used for distinguishing and separating the oligomeric and monomeric *C. albicans* γ-TuSCs purified in section **4.4.2**. The Superose 6 Increase 10/300 GL column (Cytiva) was connected to the ÄktaGo instrument (Cytiva) with Unicorn software (version 7.6) installed on the operating computer. The column was equilibrated with ddH_2O once and HB100 buffer (Table 17) subsequently. The program was executed at a flow rate of 0.25 ml/min with the elution volume of 2 column volumes.

Table 17 Buffers used for protein purification

Buffers	Composition
RSB buffer	10 mM Tris-Cl pH7.4, 10 mM NaCl, 1.5 mM $MgCl_2$, 1 mM DTT, 250 µM EGTA
TBS buffer	50 mM Tris-Cl pH7.4, 150 mM NaCl, 1 mM $MgCl_2$, 1 mM EGTA
Buffer A	50 mM Tris-Cl pH7.4, 20 mM NaCl, 0.5 mM EGTA
Buffer B	50 mM Tris-Cl pH7.4, 1 M NaCl, 0.5 mM EGTA
HB100	40 mM K-HEPES, pH7.4, 100 mM KCl, 1 mM EGTA, 1 mM $MgCl_2$

5.5 Biochemistry methods

5.5.1 SDS-polyacrylamide gel electrophoresis (SDS-PAGE) and immunoblot

SDS-PAGE was used for the molecular size analysis of the targeting protein. In brief, protein samples containing 1x Laemmli buffer (4x Laemmli buffer diluted to 1x) were denatured at 95°C for 5 min and then loaded on 4-20% gradient gels (PROTEAN® TGX Stain-FreeTM Bio-Rad). The Mini-PROTEAN® Tetra system (Bio-Rad) was used for gel running at a constant of 30 mA. The PageRuler^{TM} Plus Prestained Protein Ladder (Thermo Fisher Scientific) was used as the indicator for the gel running. After gel running, the gels were stained with Coomassie Brilliant Blue G250 buffer (Sigma Aldrich) and visualized by CanoScan 5600F (Canon) or used for immunoblot analysis.

For the immunoblot analysis, the proteins on SDS-PAGE gels were transferred to the PVDF membrane by the Trans-Blot Turbo Transfer System (Bio-Rad) following the instructions. After transfer, the membranes were incubated in 1 x TBS-T buffer containing 5% milk powder (w/v) for 1 h at RT. The membranes were then washed 3 times with 1 x TBS-T buffer and the appropriate volume of the 1 x TBS-T buffer containing the primary antibody (dilution time varies) was then incubated with the membranes overnight. After the primary antibody incubation, the membranes were then again washed 3 times with 1 x TBS-T buffer, and the secondary antibody (dilution time varies) in 1x TBS-T buffer was used for the second incubation with the membranes for another 1 h. The membranes were washed the last three times with 1 x TBS-T buffer. Then, the membranes were

incubated with enhanced chemiluminescence (ECL) solutions for 3-5 minutes and were documented with the LAS/Amersham imaging system.

5.5.1 Pull-down experiment

The pull-down experiment was mainly performed in the second part (section 3.1) of the thesis. First, to verify the interaction regions between Stu2 and Spc72, 1 ml of cell pellet from FLAG-tagged wild-type Stu2, Stu2$^{\Delta 666\text{-}768}$ mutant, or Stu2$^{\Delta 894\text{-}924}$ mutant was used for the pull-down. The cell pellet was lysed in TBS-200 (50 mM Tris-Cl, pH7.4, 200 mM NaCl, 1 mM EGTA, 1 mM $MgCl_2$, PMSF (1:100 vol/vol), Brij35 (0.25% vol/vol) and one PI tablet per 50 ml). Then, to test the binding of the Spc72^{3R} mutant to FLAG-tagged γ-TuSC, 1 ml of cell pellet from FLAG-tagged γ-TuSC$^{FLAG\text{-}Spc98}$ sample was used for pull-down. The cell pellet was lysed in TBS (50 mM Tris-Cl, pH7.4, 150 mM NaCl, 1 mM EGTA, 1 mM $MgCl_2$, PMSF (1:100 vol/vol)) and one PI tablet per 50 ml).

For both experiments, cells were then sonicated (3 × 1 min with 0.8 amplitude, Hielscher UP50H) and centrifuged at 20,000 × g for 30 min at 4°C. The supernatant was incubated with Anti-FLAG M2 Affinity Gel (Sigma-Aldrich) and incubated for 2 h at 4°C. After incubation, affinity gel was washed 3 times with wash buffer (50 mM Tris-Cl, pH7.4; 200 mM NaCl, 1 mM EGTA, 1 mM $MgCl_2$, one PI tablet per 50 ml for Stu2 and Spc72 interactions, same buffer with 150 mM NaCl was used for γ-TuSC and Spc72^{3R} interactions) before the addition of the Spc72 fragments (20 µg) or with the same volume of wash buffer (as negative control). As a complementary negative control, meanwhile, the same amount of Anti-FLAG M2 Affinity Gel was used and incubated with Spc72 fragments (20 µg) in the absence of FLAG-Stu2. Then, the mixtures were incubated for 1 h. For elution, wash buffer was supplemented with 300 µg/ml 3 × FLAG peptide. Eluted proteins were separated by 4-20% precast polyacrylamide gels (Bio-Rad), immunoblotted with the antibody, and visualized with a LAS-3000 imaging system (Fujifilm Life Science). The antibodies used in this study are listed in Table 18. Additionally, all the buffers used in the section 5.5.1 are listed in Table 19.

Table 18 Antibody list

Antibody	Description
anti-FLAG antibody	mouse; clone 9A3, 1:1000; Cell Signaling
anti-penta-His antibody	anti-penta-His (mouse, 1:2000; Qiagen 34660)
anti-γ-tubulin antibody	guinea pig; 1:1000; home-made *C. albicans* γ-tubulin antigen (331-498aa fragment was sent to Eurogentec for antibody production

Table 19 Pull-down related buffers

Buffer	Composition
TBS-200	50 mM Tris-Cl pH 7.4, 200 mM NaCl, 1 mM EGTA, 1 mM $MgCl_2$
TBS buffer	50 mM Tris-Cl pH 7.4; 150 mM NaCl, 1 mM $MgCl_2$, 1 mM EGTA

5.6 Yeast phenotype analysis

5.6.1 *S. cerevisiae spc72$^{\Delta P55\text{-}N62}$* and *spc72^{3R}* phenotype analysis

To analyze the growth phenotype of the Spc72 mutants (*spc72$^{\Delta P55\text{-}N62}$* and *spc72^{3R}*) in *S. cerevisiae in vivo*, the plasmids of pRS315-*SPC72*, pRS315-*spc72$^{\Delta P55\text{-}N62}$*, pRS315-*spc72^{3R}*, and pRS315 were transformed into strain ESM448-1 (*MATa ura3-52 lys2-801 ade2-101 trp1Δ63 his3Δ200 leu2Δ1 Δspc72::KanMx6* pRS316-*SPC72*) in the S228c background (Table 20). The transformed cells were plated onto SC-Leu-Ura plates and incubated for 2 days at 30°C. The colonies were inoculated into SC-Leu liquid medium cultured at 30°C overnight and then were serially diluted and dropped onto SC-Leu and 5-FOA plates continuously cultured at 30°C and 23°C for 2 to 3 days.

For analyzing the mutant cells by fluorescent microscopy, pRS305-*SPC72*, pRS305-*spc72$^{\Delta P55\text{-}N62}$*, pRS305-*spc72^{3R}*, and pRS305 plasmids were digested with HpaI and transformed into the *S. cerevisiae* YJP287-1 strain *(Δspc72::KanMx6* pRS316-*SPC72 SPC42-mCherry-hgh GFP-TUB1-ADE2*) in W303 background (Table 20). Transformants were plated onto SC-Leu-Ura plates and cultured for 2 days at 30°C. For each plate, 6 colonies were selected, replated on SC-Leu and 5-FOA plates, and then cultured at 23°C

for another 3-6 days. Cells transformed with *SPC72* or *spc72*^{3R} were then cultured in SC-Leu (+ adenine) medium at 23°C for 1 to 2 days and stained with DAPI or directly observed using a DeltaVision microscope (see below). For the mutant cells containing *spc72*$^{\Delta P55\text{-}N62}$, cells were serially diluted, dropped onto SC-Leu and 5-FOA plates, and cultured at 16°C for 5 days. Cells were then cultured in SC-Leu (+ adenine) medium at 16°C for 2 days and stained with DAPI or directly observed using a DeltaVision microscope (see below).

Table 20 Yeast strain list

Yeast strains	Description
ESM448-1 strain, S288c background	*MATa ura3-52 lys2-801 ade2-101 trp1Δ63 his3Δ200 leu2Δ1 Δspc72::KanMx6* pRS316-*SPC72*
ESM243-2 strain, S288c background	*MATa ura3-52 lys2-801 ade2-101::pRS402-yeGFP-TUB1 trp1Δ63 his3Δ200 leu2Δ1 Δspc98::HIS3* pRS316-*SPC98 SPC42-mCherry-natNT2*
ESM448-1, S288c background	*MATa ura3-52 lys2-801 ade2-101 trp1Δ63 his3Δ200 leu2Δ1 Δspc72::KanMx6* pRS316-*SPC72*
YJP287-1, W303 background	*MATa ade2-1 ura3-1 his3-11, 15 trp1-1 leu2-3, 113 can1-100 Δspc72::KanMx6* pRS316-*SPC72 SPC42-mCherry-hgh GFP-TUB1-ADE2*

5.7 Electron microscopy experiment

EM experiments were supported by the Cryo-Electron Microscopy Network of Heidelberg University (HDcryoNet). The SDS@hd and bwHPC services were used for data storage and processing. DeltaVision microscopy was supported by AG Schiebel.

5.7.1 Negative stain EM and the data processing

The negative stain EM part and image acquisition were conducted by Dr. Annett Neuner. The negative stain EM methods for the γ-tubulin small complex were documented in the published work[3]. In brief, samples for the test were applied on glow-discharged copper-palladium 400 EM mesh grids covered with an approximately 9-10 nm-thick continuous

carbon layer and incubated for 30 s at RT. Grids were blotted with Whatman filter paper 50 (cat no. 1450-070, Cytiva) and rinsed with 3 drops of distilled water, followed by staining with 3% uranyl acetate in distilled water. Micrographs were acquired on a Talos L120C TEM equipped with a 4 k × 4 k Ceta CMOS camera (Thermo Fisher Scientific) using the EPU software (Thermo Fischer Scientific) at an approximate defocus of −2 µm to −2.5 µm and an object pixel size of 0.2552 nm.

For the γ-tubulin small complex project[3], 997 images of wild-type γ-TuSC, 821 images of mutant γ-TuSC (Spc98$^{\Delta D627\text{-}K650}$), and 1147 images of mutant γ-TuSC (Tub4$^{\Delta T38\text{-}K71}$) were acquired. For the γ-TuRC, 609 images of γ-TuSC/Spc72/FLAG-Stu2 sample in TBS buffer, 726 images of γ-TuSC/Spc72/FLAG-Stu2 in HB100 buffer (SEC), and 2481 images of γ-TuSC/Spc72/GFP-Mzt1 in HB100 buffer (SEC) were acquired. The dataset was acquired from one imaging session.

Image analysis for all datasets was performed in RELION 3.0 Beta[190]. Gctf was used for micrograph contrast transfer function (CTF) estimation[215]. For the datasets of the small complexes, ~1000 particles were manually selected and extracted at a pixel size of 0.51 nm in boxes of 128 pixels. Particles were subsequently subjected to 2D classification into 50 classes with a translational search range of 20 pixels (2 pixels increment) and a mask diameter of 350–400 Å. 2D classes representing true positive particles were selected and used as references for automated particle picking. The overall number of picked particles was 347,445 for the wild-type γ-TuSC, 154,883 for the Spc98$^{\Delta D627\text{-}K650}$ mutant γ-TuSC, and 241,205 for the Tub4$^{\Delta T38\text{-}K71}$ mutant γ-TuSC. Particles were subjected to 2D classification into 200 classes with parameters as described above. 2D classes representing true positive particles were selected for a second round of 2D classification using the same parameters. Selected classes of the Tub4$^{\Delta T38\text{-}K71}$ mutant γ-TuSC were subjected to a third round of classification into 170 classes. The final number of particles used for computing the ratios of particles with a straddled appearance were 77,858 for the wild-type γ-TuSC, 11,901 for the Spc98$^{\Delta D627\text{-}K650}$ mutant γ-TuSC and 15,450 for the Tub4$^{\Delta T38\text{-}K71}$ mutant γ-TuSC.

For the datasets of the ring complexes, γ-TuSC/Spc72/FLAG-Stu2 samples in TBS and HB100 buffer and there are 3,179 and 6,106 particles manually picked and extracted at a pixel size of 0.51 nm (TBS) and 0.656 nm (HB100) in boxes of 128 pixels. For γ-

TuSC/Spc72/GFP-Mzt1, 1,629 ring-like particles were manually selected from 2,481 images and extracted at a pixel size of 0.51 nm and box size of 128 pixels. Particles were then 2D classified into 50 classes, with a mask diameter of 400 Å. After 2D classification, the best 2D classes were subjected to 3D classification into 4 classes and a regularisation parameter T of 10 (for γ-TuSC/Spc72/FLAG-Stu2 in TBS buffer and for γ-TuSC/Spc72/GFP-Mzt1) or 6 classes and a regularization parameter T of 8 (γ-TuSC/Spc72/FLAG-Stu2 in HB100 buffer). After 3D classification, 3D auto-refinement was performed, with the human γ-TuRC (EMD-21074)[119] as a reference.

5.7.2 DeltaVision microscope

For visualizing yeast cells with the fluorescent proteins, 3 µl of cells were dropped onto glass slides and then covered with a 35-mm glass dish. Images were acquired with a DeltaVision RT system (Applied Precision) on an Olympus IX71 microscope equipped with 100X NA UPlanSAPO objective lens (Olympus) with the same exposure time and illumination settings and 2 × 2 binning. For DAPI-stained cells, the DAPI channel was selected for live cell imaging, and TRITC/FITC channels were selected for tracing the signals from *TUB1-GFP* and *SPC42-mCherry* with the softWoRx software (Applied Precision).

5.8 Cryo-EM experiments

Cryo-EM experiments, as well as model building based on cryo-EM densities for the recombinant *C. albicans* γ-TuSC were performed by Dr. Erik Zupa, and the processing information of the Cryo-EM part in detail can be found in the published work[3].

For the cryo-EM analysis of γ-TuSC/Spc72/FLAG-Stu2 complex, the cryo-EM sample preparation, the model building, and the structural prediction part were performed by Bram J.A. Vermeulen with the processing information described below.

5.8.1 Cryo-EM sample preparation and data acquisition for γ-TuSC/Spc72/ FLAG-Stu2 complex

The R2/1 Cu 200 mesh grids (Quantifoil) were glow-discharged for one min in a PELCO easiGlow. 4 µl of γ-TuSC/Spc72/FLAG-Stu2 was applied to the glow-discharged grid by using a Vitrobot Mark IV (Thermo Fisher Scientific, Eindhoven) at 4°C and relative humidity of 100%. The blot time was 5 s with the blot force of 5. After 10 s of waiting and after 1 s of draining, the grid was plunge-frozen into liquid ethane.

EPU software (Thermo Fisher Scientific) installed with a 300 kV Titan Krios (Thermo Fisher Scientific/FEI, Eindhoven) equipped with a K3 camera and a Quantum Gatan Imaging Filter (Gatan) operated at 20 kV energy slit width were used for the data acquisition. 2,231 movies at a magnification of 33,000 x (2.54 Å/px) in 50 fractions were exposed at a rate of 24 e-/px/s and a cumulative electron exposure of 43 e-/Å2, with a nominal defocus of -1 µm to -3 µm at a 0.5 µm increment. Two more datasets of 15,871 and 17,910 movies were acquired at 81,000 x magnification (1.07 Å/px) with a 100 µm objective aperture and exposed at rates of 16 e-/px/s and 17 e-/px/s, respectively, resulting in a cumulative electron exposure of 47 e-/Å2 spread over 50 fractions. Movies were acquired at a nominal defocus of -1 µm to -2 µm (dataset 1) or -1.6 µm to -2.6 µm (dataset 2) in steps of 0.5 µm.

5.8.2 Cryo-EM data processing for γ-TuSC/Spc72/FLAG-Stu2 complex

RELION 3.1[190] was used for the initial processing of the complex of γ-TuSC/Spc72/FLAG-Stu2. MotionCor2[216] and Gctf[215] were used for the motion correction of the micrograph movies and the CTF parameter estimation. In short, the 2D class generated from the initial dataset in RELION was used for the auto-picking and the 3D classification of the datasets acquired at a higher magnification (Fig. 22a). For the 2D model generation, 331 particles were manually picked from 50 randomly selected micrographs and extracted at 5.08 Å/px which was then used as for training a resnet8 model in Topaz[191]. 48,852 particles from 2,231 micrographs were auto-picked in Topaz and all the picked particles were extracted in RELION 3.1 and then moved to CryoSPARC 3.2.0[188] to select particles representing higher γ-TuSC oligomers. To obtain the 2D template for auto-picking, particles were converted back to RELION format using csparc2star.py (part of the pyEM

package[217]), re-extracted, and classified in 2D in RELION 3.1. Then, particles were subjected to reconstruction into 2 classes followed by heterogeneous refinement in two classes and finally homogeneous refinement, all in CryoSPARC, to generate a 3D reference map.

Using the reference map generated, 3D classification was then separately performed on the auto-picked particles (1 round) and Topaz-picked particles (2 rounds) of dataset 1. The best classes from the auto-picked particles and Topaz-picked particles were joined, duplicates were excluded and the remaining particles were 3D classified together, resulting in 20,122 particles for the class that was retained for further processing. These particles were subjected to 3D auto-refinement, recentered, and re-extracted at 2.14 Å/px. For the auto-picked particles of dataset 2, three random subsets were subjected to another two rounds of 3D classification, and the 27,114 particles from the two rounds of 3D classification were used for further processing which were recentered and re-extracted at 2.14 Å/px. For both datasets, the retained particles were then separately subjected to 3D auto-refinement. All subsequent processing was then done in RELION 3.0, where another round of 3D auto-refinement was performed, followed by Bayesian polishing[218] and another round of 3D auto-refinement.

As each particle represents an oligomer of γ-TuSCs of different sizes, each particle was re-extracted 5 times at 2.14 Å/px, each time re-centering a different one of the 5 best resolved γ-TuSC unit to the box center, similarly to symmetry expansion. For the γ-TuSC unit that displayed substoichiometry, particles containing this unit were first enriched by focused 3D classification without sampling, followed by local refinement and re-extraction with recentering (dataset 1) or re-extraction directly following 3D classification (dataset 2). For the other 4 γ-TuSC units, re-extraction with recentering directly followed the 3D auto-refinement was used. This resulted in 97,040 (dataset 1) or 126,685 (dataset 2) particles of centered γ-TuSC units and these two datasets were separately used for 3D auto-refinement. The 3D auto-refinement from the 2 datasets produced 223,725 particles (Fig. 22c). All the particles were then subjected to 3D auto-refinement, Bayesian polishing, and 3D auto-refinement, followed by focused 3D classification on the centered γ-TuSC unit, retaining 129,908 particles. The remaining particles were again subjected to several cycles of 3D auto-refinement, CTF refinement (per-particle defocus and beamtilt)[219], and

Bayesian polishing. The final density was sharpened by post-processing, resulting in a reconstruction of a single γ-TuSC within the higher oligomers at 3.6 Å (Fig. 21b). In this reconstruction, the inter-γ-TuSC interactions of the neighboring spokes were resolved to side chain resolution (Fig. 21a).

To assess the geometry of the full, 14-spoked rings of γ-TuSC units (Fig. 22d), the merged set of 223,725 particles from both datasets was CTF refined after Bayesian polishing. The 3D refinement was performed with a solvent mask for a full ring of γ-TuSC units. Subsequently, multiple rounds of focused 3D classification on substoichiometric γ-TuSCs and 3D refinement were performed, retaining a set of 8,261 particles of a full 14-spoked ring of γ-TuSC units and reaching 8.2 Å resolution (Fig. 21c). Finally, multi-body refinement[220] was performed with 3 bodies (covering spokes 1-4, 5-10 and 11-14) reaching resolutions between 7.1 and 8.4 Å.

5.8.3 γ-TuSC/Spc72/FLAG-Stu2 complex protein identification and model building

The initial atomic models for the γ-TuSCs (Fig. 22b) within higher oligomers were built using ModelAngelo[224] based on post-processed reconstruction, and the missing segments were manually built in Coot[221]. For some regions, the density quality only allowed Cβ-truncated residues to be built. Model errors were corrected by iterative rounds of manual correction in Coot and real-space refinement in Phenix[222], with a restraint weight of 0.6. Backbone geometry errors and clashes were resolved using MDFF simulation in ISOLDE[223].

ModelAngelo 0.2.4[224] as an independent tool for determining the identity of two coiled-coil α-helices outside of the Spc97 GRIP2 domain was run on the post-processed reconstruction without providing prior information on protein sequences. Both α-helices were identified as Spc72 with the alignment of the amino acid sequences of *C. albicans* Spc72$^{1-599}$ (UniProt[225] ID Q5AGV5), Stu2 (A0A1D8PTZ8), Spc97 (Q59PZ2), Spc98 (A0A1D8PS42) and γ-tubulin (O93807), and the comparison was conducted in ModelAngelo[224].

To build a model of a 14-spoked ring of γ-TuSC units, atomic models of the γ-TuSC were rigid-body docked into the reconstruction of the 14-spoked ring of γ-TuSCs using UCSF

Chimera[226]. To extend the available atomic model of the interaction of the CM1 motif of human CDK5RAP2 with GCP2 at spoke 13 and GCP6 at spoke 12 of the γ-TuRC, i.e., a combination of GCP2 and GCP6 from PDB-6V6S[119] and CDK5RAP2 from PDB-6X0V[120], an atomic model was built by ModelAngelo[224] providing EMD-21985[120] and protein sequence information as input. From the model built by ModelAngelo[224], GCP2 residues 442-455, 611-620, 869-883, and 767-774 were added to the composite model of GCP2, GCP6, and CDK5RAP2 from PDB-6V6S and PDB-6X0V. The pseudoatomic model for the Mzt2/GCP2N module present in PDB-6X0V[120] was replaced by the predicted Mzt2/GCP2N module in complex with a dimer of CDK5RAP2 (residues 60-200) from an AlphaFold2 Multimer (version 2.3.1)[179, 183], trimmed to exclude parts not represented by the cryo-EM density. Models were corrected by iterative rounds of manual correction in Coot, MDFF simulation in ISOLDE, and real-space refinement in Phenix, focusing on segments that were not present in the originally available models.

5.9 AlphaFold predictions

The dimeric Spc72$^{1-599}$ and Spc72$^{1-599}$ in complex with Stu2$^{882-924}$ models were predicted in AlphaFold Multimer. The top-ranked models of Spc72$^{1-599}$ in complex with Stu2$^{882-924}$ predicted in AlphaFold Multimer were trimmed to match the corresponding fragments of residues 291-428 or 429-599 of Spc72, and the models of Stu2 and Spc72 interaction were implemented in ColabFold[227].

6 Data analysis

Image processing and analysis were performed with the open-source software package ImageJ 1.46r (National Institutes of Health)[228]. SEC data and cell quantification from the yeast experiment were processed using the Prism software (GraphPad v. 8.0).

6.1 Data availability

The γ-TuSC Cryo-EM density was deposited in the Electron Microscopy Data Bank (EMDB) under accession code EMD-11835. Atomic model for the γ-TuSC were deposited at the Protein Data Bank (PDB) under accession code PDB-7ANZ.

For the γ-TuSC/Spc72/Stu2 project, the atomic coordinates and the associated cryo-EM densities were deposited in the Protein Data Bank and the Electron Microscopy Data Bank with the accession codes of PDB-xxxx / EMD-xxxx (γ-TuSCs), PDB-xxxx / EMD-xxxx (14-spoked ring), and PDB-xxxx (human CDK5RAP2^{CM1} in complex with GCP2/GCP6/Mzt2) available after this part of the work is published online.

Models predicted by AlphaFold-Multimer will be made available at the ModelArchive (https://modelarchive.org/) upon publication. Source data are provided in this paper. Published structural data used in this article: PDB-7ANZ [https://www.rcsb.org/structure/7ANZ], PDB-6X0V [https://www.rcsb.org/structure/6X0V], PDB-5MJS [https://www.rcsb.org/structure/5MJS], PDB-6V6S [https://www.rcsb.org/structure/6V6S], EMD-21985 [https://www.ebi.ac.uk/emdb/EMD-21985].

References

(1) Sanchez, A. D.; Feldman, J. L. Microtubule-organizing centers: from the centrosome to non-centrosomal sites. *Current opinion in cell biology* **2017**, *44*, 93-101.
(2) Liu, P.; Zupa, E.; Neuner, A.; Böhler, A.; Loerke, J.; Flemming, D.; Ruppert, T.; Rudack, T.; Peter, C.; Spahn, C.; et al. Insights into the assembly and activation of the microtubule nucleator γ-TuRC. *Nature* **2020**, *578* (7795), 467-471. DOI: 10.1038/s41586-019-1896-6 From NLM.
(3) Zupa, E.; Zheng, A.; Neuner, A.; Würtz, M.; Liu, P.; Böhler, A.; Schiebel, E.; Pfeffer, S. The cryo-EM structure of a γ-TuSC elucidates architecture and regulation of minimal microtubule nucleation systems. *Nature Communications* **2020**, *11* (1), 5705.
(4) Glotzer, M. Cytokinesis in Metazoa and Fungi. *Cold Spring Harb Perspect Biol* **2017**, *9* (10). DOI: 10.1101/cshperspect.a022343 From NLM.
(5) D'Avino, P. P.; Savoian, M. S.; Glover, D. M. Cleavage furrow formation and ingression during animal cytokinesis: a microtubule legacy. *Journal of Cell Science* **2005**, *118* (8), 1549-1558.
(6) McCollum, D. Cytokinesis: the central spindle takes center stage. *Current biology* **2004**, *14* (22), R953-R955.
(7) Jiang, W.; Jimenez, G.; Wells, N. J.; Hope, T. J.; Wahl, G. M.; Hunter, T.; Fukunaga, R. PRC1: a human mitotic spindle–associated CDK substrate protein required for cytokinesis. *Molecular cell* **1998**, *2* (6), 877-885.
(8) Mollinari, C.; Kleman, J.-P.; Jiang, W.; Schoehn, G.; Hunter, T.; Margolis, R. L. PRC1 is a microtubule binding and bundling protein essential to maintain the mitotic spindle midzone. *The Journal of cell biology* **2002**, *157* (7), 1175-1186.
(9) Verbrugghe, K. J.; White, J. G. SPD-1 is required for the formation of the spindle midzone but is not essential for the completion of cytokinesis in C. elegans embryos. *Current Biology* **2004**, *14* (19), 1755-1760.
(10) Zhu, C.; Lau, E.; Schwarzenbacher, R.; Bossy-Wetzel, E.; Jiang, W. Spatiotemporal control of spindle midzone formation by PRC1 in human cells. *Proceedings of the National Academy of Sciences* **2006**, *103* (16), 6196-6201.
(11) Glotzer, M. The 3Ms of central spindle assembly: microtubules, motors and MAPs. *Nature reviews Molecular cell biology* **2009**, *10* (1), 9-20.
(12) Douglas, M. E.; Davies, T.; Joseph, N.; Mishima, M. Aurora B and 14-3-3 coordinately regulate clustering of centralspindlin during cytokinesis. *Current biology* **2010**, *20* (10), 927-933.

(13) Burkard, M. E.; Maciejowski, J.; Rodriguez-Bravo, V.; Repka, M.; Lowery, D. M.; Clauser, K. R.; Zhang, C.; Shokat, K. M.; Carr, S. A.; Yaffe, M. B. Plk1 self-organization and priming phosphorylation of HsCYK-4 at the spindle midzone regulate the onset of division in human cells. *PLoS biology* **2009**, *7* (5), e1000111.
(14) Wolfe, B. A.; Takaki, T.; Petronczki, M.; Glotzer, M. Polo-like kinase 1 directs assembly of the HsCyk-4 RhoGAP/Ect2 RhoGEF complex to initiate cleavage furrow formation. *PLoS biology* **2009**, *7* (5), e1000110.
(15) Fang, X.; Luo, J.; Nishihama, R.; Wloka, C.; Dravis, C.; Travaglia, M.; Iwase, M.; Vallen, E. A.; Bi, E. Biphasic targeting and cleavage furrow ingression directed by the tail of a myosin II. *Journal of Cell Biology* **2010**, *191* (7), 1333-1350.
(16) Yoshida, S.; Kono, K.; Lowery, D. M.; Bartolini, S.; Yaffe, M. B.; Ohya, Y.; Pellman, D. Polo-like kinase Cdc5 controls the local activation of Rho1 to promote cytokinesis. *Science* **2006**, *313* (5783), 108-111.
(17) Kovar, D. R. Molecular details of formin-mediated actin assembly. *Current opinion in cell biology* **2006**, *18* (1), 11-17.
(18) Bi, E.; Park, H.-O. Cell polarization and cytokinesis in budding yeast. *Genetics* **2012**, *191* (2), 347-387.
(19) Pellman, D.; Bagget, M.; Tu, Y.; Fink, G. R.; Tu, H. Two microtubule-associated proteins required for anaphase spindle movement in Saccharomyces cerevisiae. *The Journal of cell biology* **1995**, *130* (6), 1373-1385.
(20) Mishima, M.; Kaitna, S.; Glotzer, M. Central spindle assembly and cytokinesis require a kinesin-like protein/RhoGAP complex with microtubule bundling activity. *Developmental cell* **2002**, *2* (1), 41-54.
(21) Subramanian, R.; Ti, S.-C.; Tan, L.; Darst, S. A.; Kapoor, T. M. Marking and measuring single microtubules by PRC1 and kinesin-4. *Cell* **2013**, *154* (2), 377-390.
(22) Goodson, H. V.; Jonasson, E. M. Microtubules and Microtubule-Associated Proteins. *Cold Spring Harb Perspect Biol* **2018**, *10* (6). DOI: 10.1101/cshperspect.a022608 From NLM.
(23) Tilney, L. G.; Bryan, J.; Bush, D. J.; Fujiwara, K.; Mooseker, M. S.; Murphy, D. B.; Snyder, D. H. Microtubules: evidence for 13 protofilaments. *J Cell Biol* **1973**, *59* (2 Pt 1), 267-275. DOI: 10.1083/jcb.59.2.267 From NLM.
(24) Wade, R. H.; Chrétien, D.; Job, D. Characterization of microtubule protofilament numbers. How does the surface lattice accommodate? *J Mol Biol* **1990**, *212* (4), 775-786. DOI: 10.1016/0022-2836(90)90236-f From NLM.

(25) Chrétien, D.; Metoz, F.; Verde, F.; Karsenti, E.; Wade, R. H. Lattice defects in microtubules: protofilament numbers vary within individual microtubules. *J Cell Biol* **1992**, *117* (5), 1031-1040. DOI: 10.1083/jcb.117.5.1031 From NLM.
(26) Sui, H.; Downing, K. H. Structural basis of interprotofilament interaction and lateral deformation of microtubules. *Structure* **2010**, *18* (8), 1022-1031. DOI: 10.1016/j.str.2010.05.010 From NLM.
(27) Sept, D.; Baker, N. A.; McCammon, J. A. The physical basis of microtubule structure and stability. *Protein Sci* **2003**, *12* (10), 2257-2261. DOI: 10.1110/ps.03187503 From NLM.
(28) Roll-Mecak, A. Intrinsically disordered tubulin tails: complex tuners of microtubule functions? *Semin Cell Dev Biol* **2015**, *37*, 11-19. DOI: 10.1016/j.semcdb.2014.09.026 From NLM.
(29) Li, H.; DeRosier, D. J.; Nicholson, W. V.; Nogales, E.; Downing, K. H. Microtubule structure at 8 A resolution. *Structure* **2002**, *10* (10), 1317-1328. DOI: 10.1016/s0969-2126(02)00827-4 From NLM.
(30) Soppina, V.; Herbstman, J. F.; Skiniotis, G.; Verhey, K. J. Luminal localization of α-tubulin K40 acetylation by cryo-EM analysis of fab-labeled microtubules. *PLoS One* **2012**, *7* (10), e48204. DOI: 10.1371/journal.pone.0048204 From NLM.
(31) Garvalov, B. K.; Zuber, B.; Bouchet-Marquis, C.; Kudryashev, M.; Gruska, M.; Beck, M.; Leis, A.; Frischknecht, F.; Bradke, F.; Baumeister, W.; et al. Luminal particles within cellular microtubules. *J Cell Biol* **2006**, *174* (6), 759-765. DOI: 10.1083/jcb.200606074 From NLM.
(32) van den Berg, C. M.; Volkov, V. A.; Schnorrenberg, S.; Huang, Z.; Stecker, K. E.; Grigoriev, I.; Gilani, S.; Frikstad, K. M.; Patzke, S.; Zimmermann, T.; et al. CSPP1 stabilizes growing microtubule ends and damaged lattices from the luminal side. *J Cell Biol* **2023**, *222* (4). DOI: 10.1083/jcb.202208062 From NLM.
(33) Hawkins, T.; Mirigian, M.; Selcuk Yasar, M.; Ross, J. L. Mechanics of microtubules. *J Biomech* **2010**, *43* (1), 23-30. DOI: 10.1016/j.jbiomech.2009.09.005 From NLM.
(34) Weisenberg, R. C.; Broisy, G. G.; Taylor, E. W. Colchicine-binding protein of mammalian brain and its relation to microtubules. *Biochemistry* **1968**, *7* (12), 4466-4479.
(35) Menéndez, M.; Rivas, G.; Dıaz, J. F.; Andreu, J. M. Control of the structural stability of the tubulin dimer by one high affinity bound magnesium ion at nucleotide N-site. *Journal of Biological Chemistry* **1998**, *273* (1), 167-176.
(36) Löwe, J.; Li, H.; Downing, K.; Nogales, E. Refined structure of αβ-tubulin at 3.5 Å resolution. *Journal of molecular biology* **2001**, *313* (5), 1045-1057.

(37) Vulevic, B.; Correia, J. J. Thermodynamic and structural analysis of microtubule assembly: the role of GTP hydrolysis. *Biophysical Journal* **1997**, *72* (3), 1357-1375.
(38) Cassimeris, L. Regulation of microtubule dynamic instability. *Cell Motil Cytoskeleton* **1993**, *26* (4), 275-281. DOI: 10.1002/cm.970260402 From NLM.
(39) Dehmelt, L.; Halpain, S. The MAP2/Tau family of microtubule-associated proteins. *Genome Biol* **2005**, *6* (1), 204. DOI: 10.1186/gb-2004-6-1-204 From NLM.
(40) Al-Bassam, J.; van Breugel, M.; Harrison, S. C.; Hyman, A. Stu2p binds tubulin and undergoes an open-to-closed conformational change. *J Cell Biol* **2006**, *172* (7), 1009-1022. DOI: 10.1083/jcb.200511010 From NLM.
(41) Brouhard, G. J.; Stear, J. H.; Noetzel, T. L.; Al-Bassam, J.; Kinoshita, K.; Harrison, S. C.; Howard, J.; Hyman, A. A. XMAP215 is a processive microtubule polymerase. *Cell* **2008**, *132* (1), 79-88. DOI: 10.1016/j.cell.2007.11.043 From NLM.
(42) Al-Bassam, J.; Kim, H.; Brouhard, G.; van Oijen, A.; Harrison, S. C.; Chang, F. CLASP promotes microtubule rescue by recruiting tubulin dimers to the microtubule. *Dev Cell* **2010**, *19* (2), 245-258. DOI: 10.1016/j.devcel.2010.07.016 From NLM.
(43) Al-Bassam, J.; Chang, F. Regulation of microtubule dynamics by TOG-domain proteins XMAP215/Dis1 and CLASP. *Trends Cell Biol* **2011**, *21* (10), 604-614. DOI: 10.1016/j.tcb.2011.06.007 From NLM.
(44) Brouhard, G. J.; Rice, L. M. The contribution of αβ-tubulin curvature to microtubule dynamics. *J Cell Biol* **2014**, *207* (3), 323-334. DOI: 10.1083/jcb.201407095 From NLM.
(45) Ayaz, P.; Ye, X.; Huddleston, P.; Brautigam, C. A.; Rice, L. M. A TOG:αβ-tubulin complex structure reveals conformation-based mechanisms for a microtubule polymerase. *Science* **2012**, *337* (6096), 857-860. DOI: 10.1126/science.1221698 From NLM.
(46) Farmer, V.; Arpağ, G.; Hall, S. L.; Zanic, M. XMAP215 promotes microtubule catastrophe by disrupting the growing microtubule end. *J Cell Biol* **2021**, *220* (10). DOI: 10.1083/jcb.202012144 From NLM.
(47) Cassimeris, L. The oncoprotein 18/stathmin family of microtubule destabilizers. *Curr Opin Cell Biol* **2002**, *14* (1), 18-24. DOI: 10.1016/s0955-0674(01)00289-7 From NLM.
(48) Roll-Mecak, A.; McNally, F. J. Microtubule-severing enzymes. *Curr Opin Cell Biol* **2010**, *22* (1), 96-103. DOI: 10.1016/j.ceb.2009.11.001 From NLM.
(49) Walczak, C. E.; Gayek, S.; Ohi, R. Microtubule-depolymerizing kinesins. *Annu Rev Cell Dev Biol* **2013**, *29*, 417-441. DOI: 10.1146/annurev-cellbio-101512-122345 From NLM.
(50) Knop, M.; Pereira, G.; Geissler, S.; Grein, K.; Schiebel, E. The spindle pole body component Spc97p interacts with the γ-tubulin of Saccharomyces cerevisiae and

functions in microtubule organization and spindle pole body duplication. *The EMBO journal* **1997**, *16* (7), 1550-1564.
(51) Geissler, S.; Pereira, G.; Spang, A.; Knop, M.; Souès, S.; Kilmartin, J.; Schiebel, E. The spindle pole body component Spc98p interacts with the gamma-tubulin-like Tub4p of Saccharomyces cerevisiae at the sites of microtubule attachment. *The EMBO journal* **1996**, *15* (15), 3899-3911.
(52) Zheng, Y.; Wong, M. L.; Alberts, B.; Mitchison, T. Nucleation of microtubule assembly by a γ-tubulin-containing ring complex. *Nature* **1995**, *378* (6557), 578-583.
(53) Meng, W.; Mushika, Y.; Ichii, T.; Takeichi, M. Anchorage of microtubule minus ends to adherens junctions regulates epithelial cell-cell contacts. *Cell* **2008**, *135* (5), 948-959.
(54) Baines, A. J.; Bignone, P. A.; King, M. D.; Maggs, A. M.; Bennett, P. M.; Pinder, J. C.; Phillips, G. W. The CKK domain (DUF1781) binds microtubules and defines the CAMSAP/ssp4 family of animal proteins. *Molecular biology and evolution* **2009**, *26* (9), 2005-2014.
(55) Goodwin, S. S.; Vale, R. D. Patronin regulates the microtubule network by protecting microtubule minus ends. *Cell* **2010**, *143* (2), 263-274.
(56) Jiang, K.; Hua, S.; Mohan, R.; Grigoriev, I.; Yau, K. W.; Liu, Q.; Katrukha, E. A.; Altelaar, A. M.; Heck, A. J.; Hoogenraad, C. C. Microtubule minus-end stabilization by polymerization-driven CAMSAP deposition. *Developmental cell* **2014**, *28* (3), 295-309.
(57) Hendershott, M. C.; Vale, R. D. Regulation of microtubule minus-end dynamics by CAMSAPs and Patronin. *Proceedings of the National Academy of Sciences* **2014**, *111* (16), 5860-5865.
(58) Sanchez, A. D.; Feldman, J. L. Microtubule-organizing centers: from the centrosome to non-centrosomal sites. *Curr Opin Cell Biol* **2017**, *44*, 93-101. DOI: 10.1016/j.ceb.2016.09.003 From NLM.
(59) Abal, M.; Piel, M.; Bouckson-Castaing, V.; Mogensen, M.; Sibarita, J.-B.; Bornens, M. Microtubule release from the centrosome in migrating cells. *The Journal of cell biology* **2002**, *159* (5), 731-737.
(60) Vinogradova, T.; Paul, R.; Grimaldi, A. D.; Loncarek, J.; Miller, P. M.; Yampolsky, D.; Magidson, V.; Khodjakov, A.; Mogilner, A.; Kaverina, I. Concerted effort of centrosomal and Golgi-derived microtubules is required for proper Golgi complex assembly but not for maintenance. *Molecular biology of the cell* **2012**, *23* (5), 820-833.
(61) Huxley, J. S. The Cell in Development and Heredity. *Nature* **1925**, *115* (2897), 669-671. DOI: 10.1038/115669a0.
(62) Stearns, T.; Winey, M. The cell center at 100. *Cell* **1997**, *91* (3), 303-309. DOI: 10.1016/s0092-8674(00)80414-6 From NLM.

(63) Meunier, S.; Vernos, I. Acentrosomal microtubule assembly in mitosis: the where, when, and how. *Trends in cell biology* **2016**, *26* (2), 80-87.
(64) Fry, A. M.; Sampson, J.; Shak, C.; Shackleton, S. Recent advances in pericentriolar material organization: ordered layers and scaffolding gels. *F1000Res* **2017**, *6*, 1622. DOI: 10.12688/f1000research.11652.1 From NLM.
(65) Walczak, C. E.; Heald, R. Mechanisms of mitotic spindle assembly and function. *Int Rev Cytol* **2008**, *265*, 111-158. DOI: 10.1016/s0074-7696(07)65003-7 From NLM.
(66) Magescas, J.; Zonka, J. C.; Feldman, J. L. A two-step mechanism for the inactivation of microtubule organizing center function at the centrosome. *Elife* **2019**, *8*. DOI: 10.7554/eLife.47867 From NLM.
(67) Arquint, C.; Gabryjonczyk, A.-M.; Nigg, E. A. Centrosomes as signalling centres. *Philosophical Transactions of the Royal Society B: Biological Sciences* **2014**, *369* (1650), 20130464.
(68) OToole, E.; Winey, M. Centriole structure. *Philosophical Transactions of the Royal Society B: Biological Sciences* **2014**, *369* (1650).
(69) Azimzadeh, J.; Marshall, W. F. Building the centriole. *Current Biology* **2010**, *20* (18), R816-R825.
(70) Blanco-Ameijeiras, J.; Lozano-Fernández, P.; Martí, E. Centrosome maturation–in tune with the cell cycle. *Journal of Cell Science* **2022**, *135* (2), jcs259395.
(71) Woodruff, J. B.; Wueseke, O.; Hyman, A. A. Pericentriolar material structure and dynamics. *Philosophical Transactions of the Royal Society B: Biological Sciences* **2014**, *369* (1650), 20130459.
(72) Piel, M.; Meyer, P.; Khodjakov, A.; Rieder, C. L.; Bornens, M. The respective contributions of the mother and daughter centrioles to centrosome activity and behavior in vertebrate cells. *The Journal of cell biology* **2000**, *149* (2), 317-330.
(73) Bornens, M. The centrosome in cells and organisms. *Science* **2012**, *335* (6067), 422-426. DOI: 10.1126/science.1209037 From NLM.
(74) Moritz, M.; Braunfeld, M. B.; Guénebaut, V.; Heuser, J.; Agard, D. A. Structure of the γ-tubulin ring complex: a template for microtubule nucleation. *Nature cell biology* **2000**, *2* (6), 365-370.
(75) Conduit, P. T.; Wainman, A.; Raff, J. W. Centrosome function and assembly in animal cells. *Nature reviews Molecular cell biology* **2015**, *16* (10), 611-624.
(76) Zhu, X.; Kaverina, I. Golgi as an MTOC: making microtubules for its own good. *Histochemistry and cell biology* **2013**, *140*, 361-367.
(77) Akhmanova, A.; Kapitein, L. C. Mechanisms of microtubule organization in differentiated animal cells. *Nature Reviews Molecular Cell Biology* **2022**, *23* (8), 541-558.

(78) Weiner, A. T.; Seebold, D. Y.; Torres-Gutierrez, P.; Folker, C.; Swope, R. D.; Kothe, G. O.; Stoltz, J. G.; Zalenski, M. K.; Kozlowski, C.; Barbera, D. J. Endosomal Wnt signaling proteins control microtubule nucleation in dendrites. *PLoS biology* **2020**, *18* (3), e3000647.
(79) Harris, T. J.; Peifer, M. aPKC controls microtubule organization to balance adherens junction symmetry and planar polarity during development. *Developmental cell* **2007**, *12* (5), 727-738.
(80) Feldman, J. L.; Priess, J. R. A role for the centrosome and PAR-3 in the hand-off of MTOC function during epithelial polarization. *Current Biology* **2012**, *22* (7), 575-582.
(81) Patalano, S.; Prulière, G.; Prodon, F.; Paix, A.; Dru, P.; Sardet, C.; Chenevert, J. The aPKC–PAR-6–PAR-3 cell polarity complex localizes to the centrosome attracting body, a macroscopic cortical structure responsible for asymmetric divisions in the early ascidian embryo. *Journal of cell science* **2006**, *119* (8), 1592-1603.
(82) Gimpel, P.; Lee, Y. L.; Sobota, R. M.; Calvi, A.; Koullourou, V.; Patel, R.; Mamchaoui, K.; Nédélec, F.; Shackleton, S.; Schmoranzer, J. Nesprin-1α-dependent microtubule nucleation from the nuclear envelope via Akap450 is necessary for nuclear positioning in muscle cells. *Current Biology* **2017**, *27* (19), 2999-3009. e2999.
(83) Vergarajauregui, S.; Becker, R.; Steffen, U.; Sharkova, M.; Esser, T.; Petzold, J.; Billing, F.; Kapiloff, M. S.; Schett, G.; Thievessen, I. AKAP6 orchestrates the nuclear envelope microtubule-organizing center by linking golgi and nucleus via AKAP9. *elife* **2020**, *9*, e61669.
(84) Chen, J. V.; Buchwalter, R. A.; Kao, L.-R.; Megraw, T. L. A splice variant of centrosomin converts mitochondria to microtubule-organizing centers. *Current Biology* **2017**, *27* (13), 1928-1940. e1926.
(85) Nabais, C.; Peneda, C.; Bettencourt-Dias, M. Evolution of centriole assembly. *Current Biology* **2020**, *30* (10), R494-R502.
(86) Jaspersen, S. L. Anatomy of the fungal microtubule organizing center, the spindle pole body. *Current opinion in structural biology* **2021**, *66*, 22-31.
(87) Jaspersen, S. L.; Winey, M. The budding yeast spindle pole body: structure, duplication, and function. *Annu. Rev. Cell Dev. Biol.* **2004**, *20*, 1-28.
(88) Schramm, C.; Elliott, S.; Shevchenko, A.; Shevchenko, A.; Schiebel, E. The Bbp1p–Mps2p complex connects the SPB to the nuclear envelope and is essential for SPB duplication. *The EMBO journal* **2000**.
(89) Pereira, G.; Grueneberg, U.; Knop, M.; Schiebel, E. Interaction of the yeast γ-tubulin complex-binding protein Spc72p with Kar1p is essential for microtubule function during karyogamy. *The EMBO journal* **1999**.

(90) Calarco-Gillam, P. D.; Siebert, M. C.; Hubble, R.; Mitchison, T.; Kirschner, M. Centrosome development in early mouse embryos as defined by an autoantibody against pericentriolar material. *Cell* **1983**, *35* (3 Pt 2), 621-629. DOI: 10.1016/0092-8674(83)90094-6 From NLM.
(91) Heald, R.; Tournebize, R.; Blank, T.; Sandaltzopoulos, R.; Becker, P.; Hyman, A.; Karsenti, E. Self-organization of microtubules into bipolar spindles around artificial chromosomes in Xenopus egg extracts. *Nature* **1996**, *382* (6590), 420-425. DOI: 10.1038/382420a0 From NLM.
(92) Vernos, I.; Karsenti, E. Chromosomes take the lead in spindle assembly. *Trends in Cell Biology* **1995**, *5* (8), 297-301. DOI: https://doi.org/10.1016/S0962-8924(00)89045-5.
(93) Marc, J. Microtubule-organizing centres in plants. *Trends in Plant Science* **1997**, *2* (6), 223-230. DOI: https://doi.org/10.1016/S1360-1385(97)89547-7.
(94) Khodjakov, A.; Cole, R. W.; Oakley, B. R.; Rieder, C. L. Centrosome-independent mitotic spindle formation in vertebrates. *Current Biology* **2000**, *10* (2), 59-67.
(95) Basto, R.; Lau, J.; Vinogradova, T.; Gardiol, A.; Woods, C. G.; Khodjakov, A.; Raff, J. W. Flies without Centrioles. *Cell* **2006**, *125* (7), 1375-1386. DOI: https://doi.org/10.1016/j.cell.2006.05.025.
(96) Wheatley, D. N. The centriole: a central enigma of cell biology. *(No Title)* **1982**.
(97) Yang, J.; Hu, X.; Ma, J.; Shi, S. H. Centrosome regulation and function in mammalian cortical neurogenesis. *Curr Opin Neurobiol* **2021**, *69*, 256-266. DOI: 10.1016/j.conb.2021.06.003 From NLM.
(98) Bisgrove, B. W.; Yost, H. J. The roles of cilia in developmental disorders and disease. *Development* **2006**, *133* (21), 4131-4143. DOI: 10.1242/dev.02595 From NLM.
(99) Mazia, D. Centrosomes and mitotic poles. *Experimental Cell Research* **1984**, *153* (1), 1-15. DOI: https://doi.org/10.1016/0014-4827(84)90442-7.
(100) Oakley, C. E.; Oakley, B. R. Identification of γ-tubulin, a new member of the tubulin superfamily encoded by mipA gene of Aspergillus nidulans. *Nature* **1989**, *338* (6217), 662-664.
(101) Schmit, A.-C. Acentrosomal microtubule nucleation in higher plants. In *International Review of Cytology*, Vol. 220; Academic Press, 2002; pp 257-289.
(102) Ehrhardt, D. W.; Shaw, S. L. Microtubule dynamics and organization in the plant cortical array. *Annu Rev Plant Biol* **2006**, *57*, 859-875. DOI: 10.1146/annurev.arplant.57.032905.105329 From NLM.
(103) Pastuglia, M.; Azimzadeh, J.; Goussot, M.; Camilleri, C.; Belcram, K.; Evrard, J. L.; Schmit, A. C.; Guerche, P.; Bouchez, D. γ-Tubulin Is Essential for Microtubule

Organization and Development in Arabidopsis[W]. *The Plant Cell Online* **2006**, *18*, 1412 - 1425.
(104) Hagiwara, H.; Kano, A.; Aoki, T.; Ohwada, N.; Takata, K. Localization of gamma-tubulin to the basal foot associated with the basal body extending a cilium. *Histochem J* **2000**, *32* (11), 669-671. DOI: 10.1023/a:1004163315822 From NLM.
(105) Tassin, A. M.; Maro, B.; Bornens, M. Fate of microtubule-organizing centers during myogenesis in vitro. *J Cell Biol* **1985**, *100* (1), 35-46. DOI: 10.1083/jcb.100.1.35 From NLM.
(106) Lajoie-Mazenc, I.; Tollon, Y.; Detraves, C.; Julian, M.; Moisand, A.; Gueth-Hallonet, C.; Debec, A.; Salles-Passador, I.; Puget, A.; Mazarguil, H.; et al. Recruitment of antigenic gamma-tubulin during mitosis in animal cells: presence of gamma-tubulin in the mitotic spindle. *J Cell Sci* **1994**, *107 (Pt 10)*, 2825-2837. DOI: 10.1242/jcs.107.10.2825 From NLM.
(107) Chabin-Brion, K.; Marceiller, J.; Perez, F.; Settegrana, C.; Drechou, A.; Durand, G.; Poüs, C. The Golgi complex is a microtubule-organizing organelle. *Mol Biol Cell* **2001**, *12* (7), 2047-2060. DOI: 10.1091/mbc.12.7.2047 From NLM.
(108) Bugnard, E.; Zaal, K. J.; Ralston, E. Reorganization of microtubule nucleation during muscle differentiation. *Cell Motil Cytoskeleton* **2005**, *60* (1), 1-13. DOI: 10.1002/cm.20042 From NLM.
(109) Marschall, L. G.; Jeng, R. L.; Mulholland, J.; Stearns, T. Analysis of Tub4p, a yeast gamma-tubulin-like protein: implications for microtubule-organizing center function. *J Cell Biol* **1996**, *134* (2), 443-454. DOI: 10.1083/jcb.134.2.443 From NLM.
(110) Sobel, S. G.; Snyder, M. A highly divergent gamma-tubulin gene is essential for cell growth and proper microtubule organization in Saccharomyces cerevisiae. *J Cell Biol* **1995**, *131* (6 Pt 2), 1775-1788. DOI: 10.1083/jcb.131.6.1775 From NLM.
(111) Spang, A.; Geissler, S.; Grein, K.; Schiebel, E. gamma-Tubulin-like Tub4p of Saccharomyces cerevisiae is associated with the spindle pole body substructures that organize microtubules and is required for mitotic spindle formation. *J Cell Biol* **1996**, *134* (2), 429-441. DOI: 10.1083/jcb.134.2.429 From NLM.
(112) Murphy, S. M.; Urbani, L.; Stearns, T. The mammalian γ-tubulin complex contains homologues of the yeast spindle pole body components Spc97p and Spc98p. *The Journal of cell biology* **1998**, *141* (3), 663-674.
(113) Fava, F.; Raynaud-Messina, B.; Leung-Tack, J.; Mazzolini, L.; Li, M.; Guillemot, J. C.; Cachot, D.; Tollon, Y.; Ferrara, P.; Wright, M. Human 76p: A new member of the gamma-tubulin-associated protein family. *J Cell Biol* **1999**, *147* (4), 857-868. DOI: 10.1083/jcb.147.4.857 From NLM.

(114) Murphy, S. M.; Preble, A. M.; Patel, U. K.; O'Connell, K. L.; Dias, D. P.; Moritz, M.; Agard, D.; Stults, J. T.; Stearns, T. GCP5 and GCP6: two new members of the human gamma-tubulin complex. *Mol Biol Cell* **2001**, *12* (11), 3340-3352. DOI: 10.1091/mbc.12.11.3340 From NLM.
(115) Lüders, J.; Patel, U. K.; Stearns, T. GCP-WD is a γ-tubulin targeting factor required for centrosomal and chromatin-mediated microtubule nucleation. *Nature cell biology* **2006**, *8* (2), 137-147.
(116) Ravelli, R. B.; Gigant, B.; Curmi, P. A.; Jourdain, I.; Lachkar, S.; Sobel, A.; Knossow, M. Insight into tubulin regulation from a complex with colchicine and a stathmin-like domain. *Nature* **2004**, *428* (6979), 198-202.
(117) Aldaz, H.; Rice, L. M.; Stearns, T.; Agard, D. A. Insights into microtubule nucleation from the crystal structure of human γ-tubulin. *Nature* **2005**, *435* (7041), 523-527.
(118) Gombos, L.; Neuner, A.; Berynskyy, M.; Fava, L. L.; Wade, R. C.; Sachse, C.; Schiebel, E. GTP regulates the microtubule nucleation activity of γ-tubulin. *Nat Cell Biol* **2013**, *15* (11), 1317-1327. DOI: 10.1038/ncb2863 From NLM.
(119) Wieczorek, M.; Urnavicius, L.; Ti, S.-C.; Molloy, K. R.; Chait, B. T.; Kapoor, T. M. Asymmetric molecular architecture of the human γ-tubulin ring complex. *Cell* **2020**, *180* (1), 165-175. e116.
(120) Wieczorek, M.; Huang, T.-L.; Urnavicius, L.; Hsia, K.-C.; Kapoor, T. M. MZT proteins form multi-faceted structural modules in the γ-tubulin ring complex. *Cell reports* **2020**, *31* (13).
(121) Würtz, M.; Zupa, E.; Atorino, E. S.; Neuner, A.; Böhler, A.; Rahadian, A. S.; Vermeulen, B. J.; Tonon, G.; Eustermann, S.; Schiebel, E. Modular assembly of the principal microtubule nucleator γ-TuRC. *Nature communications* **2022**, *13* (1), 473.
(122) Liu, P.; Choi, Y. K.; Qi, R. Z. NME7 is a functional component of the γ-tubulin ring complex. *Mol Biol Cell* **2014**, *25* (13), 2017-2025. DOI: 10.1091/mbc.E13-06-0339 From NLM.
(123) Hutchins, J. R.; Toyoda, Y.; Hegemann, B.; Poser, I.; Hériché, J.-K.; Sykora, M. M.; Augsburg, M.; Hudecz, O.; Buschhorn, B. A.; Bulkescher, J. Systematic analysis of human protein complexes identifies chromosome segregation proteins. *Science* **2010**, *328* (5978), 593-599.
(124) Cota, R. R.; Teixidó-Travesa, N.; Ezquerra, A.; Eibes, S.; Lacasa, C.; Roig, J.; Lüders, J. MZT1 regulates microtubule nucleation by linking γTuRC assembly to adapter-mediated targeting and activation. *J Cell Sci* **2017**, *130* (2), 406-419. DOI: 10.1242/jcs.195321 From NLM.

(125) Teixidó-Travesa, N.; Villén, J.; Lacasa, C.; Bertran, M. T.; Archinti, M.; Gygi, S. P.; Caelles, C.; Roig, J.; Lüders, J. The γTuRC revisited: a comparative analysis of interphase and mitotic human γTuRC redefines the set of core components and identifies the novel subunit GCP8. *Molecular biology of the cell* **2010**, *21* (22), 3963-3972.
(126) Moritz, M.; Braunfeld, M. B.; Sedat, J. W.; Alberts, B.; Agard, D. A. Microtubule nucleation by γ-tubulin-containing rings in the centrosome. *Nature* **1995**, *378* (6557), 638-640.
(127) Horio, T.; Uzawa, S.; Jung, M. K.; Oakley, B. R.; Tanaka, K.; Yanagida, M. The fission yeast γ-tubulin is essential for mitosis and is localized at microtubule organizing centers. *Journal of cell science* **1991**, *99* (4), 693-700.
(128) Fujita, A.; Vardy, L.; Garcia, M. A.; Toda, T. A fourth component of the fission yeast γ-tubulin complex, Alp16, is required for cytoplasmic microtubule integrity and becomes indispensable when γ-tubulin function is compromised. *Molecular biology of the cell* **2002**, *13* (7), 2360-2373.
(129) Venkatram, S.; Tasto, J. J.; Feoktistova, A.; Jennings, J. L.; Link, A. J.; Gould, K. L. Identification and characterization of two novel proteins affecting fission yeast γ-tubulin complex function. *Molecular biology of the cell* **2004**, *15* (5), 2287-2301.
(130) Anders, A.; Lourenço, P. C.; Sawin, K. E. Noncore components of the fission yeast γ-tubulin complex. *Molecular biology of the cell* **2006**, *17* (12), 5075-5093.
(131) Xiong, Y.; Oakley, B. R. In vivo analysis of the functions of γ-tubulin-complex proteins. *Journal of cell science* **2009**, *122* (22), 4218-4227.
(132) Knop, M.; Schiebel, E. Spc98p and Spc97p of the yeast γ-tubulin complex mediate binding to the spindle pole body via their interaction with Spc110p. *The EMBO journal* **1997**, *16* (23), 6985-6995.
(133) Lin, T. C.; Neuner, A.; Flemming, D.; Liu, P.; Chinen, T.; Jäkle, U.; Arkowitz, R.; Schiebel, E. MOZART1 and γ-tubulin complex receptors are both required to turn γ-TuSC into an active microtubule nucleation template. *J Cell Biol* **2016**, *215* (6), 823-840. DOI: 10.1083/jcb.201606092 From NLM.
(134) Gao, X.; Schmid, M.; Zhang, Y.; Fukuda, S.; Takeshita, N.; Fischer, R. The spindle pole body of Aspergillus nidulans is asymmetrical and contains changing numbers of γ-tubulin complexes. *Journal of Cell Science* **2019**, *132* (24), jcs234799.
(135) Masuda, H.; Mori, R.; Yukawa, M.; Toda, T. Fission yeast MOZART1/Mzt1 is an essential γ-tubulin complex component required for complex recruitment to the microtubule organizing center, but not its assembly. *Molecular biology of the cell* **2013**, *24* (18), 2894-2906.

(136) Wiese, C.; Zheng, Y. A new function for the gamma-tubulin ring complex as a microtubule minus-end cap. *Nat Cell Biol* **2000**, *2* (6), 358-364. DOI: 10.1038/35014051 From NLM.
(137) Kollman, J. M.; Greenberg, C. H.; Li, S.; Moritz, M.; Zelter, A.; Fong, K. K.; Fernandez, J. J.; Sali, A.; Kilmartin, J.; Davis, T. N.; et al. Ring closure activates yeast γTuRC for species-specific microtubule nucleation. *Nat Struct Mol Biol* **2015**, *22* (2), 132-137. DOI: 10.1038/nsmb.2953 From NLM.
(138) Vermeulen, B. J.; Böhler, A.; Gao, Q.; Neuner, A.; Župa, E.; Chu, Z.; Würtz, M.; Jäkle, U.; Gruss, O. J.; Pfeffer, S. γ-TuRC asymmetry induces local protofilament mismatch at the RanGTP-stimulated microtubule minus end. *The EMBO Journal* **2024**, *43* (10), 2062-2085.
(139) Brito, C.; Serna, M.; Guerra, P.; Llorca, O.; Surrey, T. Transition of human γ-tubulin ring complex into a closed conformation during microtubule nucleation. *Science* **2024**, *383* (6685), 870-876. DOI: 10.1126/science.adk6160 From NLM.
(140) Byers, B.; Shriver, K.; Goetsch, L. The role of spindle pole bodies and modified microtubule ends in the initiation of microtubule assembly in Saccharomyces cerevisiae. *J Cell Sci* **1978**, *30*, 331-352. DOI: 10.1242/jcs.30.1.331 From NLM.
(141) Kollman, J. M.; Polka, J. K.; Zelter, A.; Davis, T. N.; Agard, D. A. Microtubule nucleating γ-TuSC assembles structures with 13-fold microtubule-like symmetry. *Nature* **2010**, *466* (7308), 879-882.
(142) Kollman, J. M.; Zelter, A.; Muller, E. G.; Fox, B.; Rice, L. M.; Davis, T. N.; Agard, D. A. The structure of the γ-tubulin small complex: implications of its architecture and flexibility for microtubule nucleation. *Molecular biology of the cell* **2008**, *19* (1), 207-215.
(143) Knop, M.; Schiebel, E. Receptors determine the cellular localization of a γ-tubulin complex and thereby the site of microtubule formation. *The EMBO Journal* **1998**, *17* (14), 3952-3967.
(144) Souès, S.; Adams, I. R. SPC72: a spindle pole component required for spindle orientation in the yeast Saccharomyces cerevisiae. *J Cell Sci* **1998**, *111 (Pt 18)*, 2809-2818. DOI: 10.1242/jcs.111.18.2809 From NLM.
(145) Lin, T.-c.; Neuner, A.; Schiebel, E. Targeting of γ-tubulin complexes to microtubule organizing centers: conservation and divergence. *Trends in cell biology* **2015**, *25* (5), 296-307.
(146) Nguyen, T.; Vinh, D. B.; Crawford, D. K.; Davis, T. N. A genetic analysis of interactions with Spc110p reveals distinct functions of Spc97p and Spc98p, components of the yeast γ-tubulin complex. *Molecular biology of the cell* **1998**, *9* (8), 2201-2216.

(147) Zekert, N.; Veith, D.; Fischer, R. Interaction of the Aspergillus nidulans microtubule-organizing center (MTOC) component ApsB with gamma-tubulin and evidence for a role of a subclass of peroxisomes in the formation of septal MTOCs. *Eukaryotic cell* **2010**, *9* (5), 795-805.
(148) Chen, P.; Gao, R.; Chen, S.; Pu, L.; Li, P.; Huang, Y.; Lu, L. A pericentrin-related protein homolog in Aspergillus nidulans plays important roles in nucleus positioning and cell polarity by affecting microtubule organization. *Eukaryotic Cell* **2012**, *11* (12), 1520-1530.
(149) Brilot, A. F.; Lyon, A. S.; Zelter, A.; Viswanath, S.; Maxwell, A.; MacCoss, M. J.; Muller, E. G.; Sali, A.; Davis, T. N.; Agard, D. A. CM1-driven assembly and activation of yeast γ-tubulin small complex underlies microtubule nucleation. *Elife* **2021**, *10*. DOI: 10.7554/eLife.65168 From NLM.
(150) Odds, F. C. *Candida and candidosis: a review and bibliography*; Bailliere Tindall, 1988.
(151) Giusiano, G.; Mangiaterra, M.; Garcia Saito, V.; Rojas, F.; Gómez, V.; Díaz, M. C. Fluconazole and itraconazole resistance of yeasts isolated from the bloodstream and catheters of hospitalized pediatric patients. *Chemotherapy* **2006**, *52* (5), 254-259.
(152) Braun, B. R.; Johnson, A. D. Control of filament formation in Candida albicans by the transcriptional repressor TUP1. *Science* **1997**, *277* (5322), 105-109.
(153) Braun, B. R.; Kadosh, D.; Johnson, A. D. NRG1, a repressor of filamentous growth in C. albicans, is down-regulated during filament induction. *The EMBO journal* **2001**.
(154) Murad, A. M. A.; Leng, P.; Straffon, M.; Wishart, J.; Macaskill, S.; MacCallum, D.; Schnell, N.; Talibi, D.; Marechal, D.; Tekaia, F. NRG1 represses yeast–hypha morphogenesis and hypha-specific gene expression in Candida albicans. *The EMBO journal* **2001**.
(155) Cullen, C. F.; Deák, P.; Glover, D. M.; Ohkura, H. mini spindles: A gene encoding a conserved microtubule-associated protein required for the integrity of the mitotic spindle in Drosophila. *The Journal of cell biology* **1999**, *146* (5), 1005-1018.
(156) Tournebize, R.; Popov, A.; Kinoshita, K.; Ashford, A. J.; Rybina, S.; Pozniakovsky, A.; Mayer, T. U.; Walczak, C. E.; Karsenti, E.; Hyman, A. A. Control of microtubule dynamics by the antagonistic activities of XMAP215 and XKCM1 in Xenopus egg extracts. *Nature cell biology* **2000**, *2* (1), 13-19.
(157) Shirasu-Hiza, M.; Coughlin, P.; Mitchison, T. Identification of XMAP215 as a microtubule-destabilizing factor in Xenopus egg extract by biochemical purification. *The Journal of cell biology* **2003**, *161* (2), 349-358.

(158) Gergely, F.; Kidd, D.; Jeffers, K.; Wakefield, J. G.; Raff, J. W. D-TACC: a novel centrosomal protein required for normal spindle function in the early Drosophila embryo. *The EMBO journal* **2000**.
(159) Lee, M. J.; Gergely, F.; Jeffers, K.; Peak-Chew, S. Y.; Raff, J. W. Msps/XMAP215 interacts with the centrosomal protein D-TACC to regulate microtubule behaviour. *Nature cell biology* **2001**, *3* (7), 643-649.
(160) Thawani, A.; Kadzik, R. S.; Petry, S. XMAP215 is a microtubule nucleation factor that functions synergistically with the γ-tubulin ring complex. *Nat Cell Biol* **2018**, *20* (5), 575-585. DOI: 10.1038/s41556-018-0091-6 From NLM.
(161) Kosco, K. A.; Pearson, C. G.; Maddox, P. S.; Wang, P. J.; Adams, I. R.; Salmon, E. D.; Bloom, K.; Huffaker, T. C. Control of microtubule dynamics by Stu2p is essential for spindle orientation and metaphase chromosome alignment in yeast. *Molecular biology of the cell* **2001**, *12* (9), 2870-2880.
(162) Van Breugel, M.; Drechsel, D.; Hyman, A. Stu2p, the budding yeast member of the conserved Dis1/XMAP215 family of microtubule-associated proteins is a plus end–binding microtubule destabilizer. *The Journal of cell biology* **2003**, *161* (2), 359-369.
(163) Wang, P. J.; Huffaker, T. C. Stu2p: A microtubule-binding protein that is an essential component of the yeast spindle pole body. *The Journal of cell biology* **1997**, *139* (5), 1271-1280.
(164) Chen, X. P.; Yin, H.; Huffaker, T. C. The yeast spindle pole body component Spc72p interacts with Stu2p and is required for proper microtubule assembly. *The Journal of cell biology* **1998**, *141* (5), 1169-1179.
(165) He, X.; Rines, D. R.; Espelin, C. W.; Sorger, P. K. Molecular analysis of kinetochore-microtubule attachment in budding yeast. *Cell* **2001**, *106* (2), 195-206.
(166) Severin, F.; Habermann, B.; Huffaker, T.; Hyman, T. Stu2 promotes mitotic spindle elongation in anaphase. *The Journal of Cell Biology* **2001**, *153* (2), 435-442.
(167) Gunzelmann, J.; Rüthnick, D.; Lin, T. C.; Zhang, W.; Neuner, A.; Jäkle, U.; Schiebel, E. The microtubule polymerase Stu2 promotes oligomerization of the γ-TuSC for cytoplasmic microtubule nucleation. *Elife* **2018**, *7*. DOI: 10.7554/eLife.39932 From NLM.
(168) Lüdtke, S.; Neumann, P.; Erixon, K. M.; Leeper, F.; Kluger, R.; Ficner, R.; Tittmann, K. Sub-ångström-resolution crystallography reveals physical distortions that enhance reactivity of a covalent enzymatic intermediate. *Nat Chem* **2013**, *5* (9), 762-767. DOI: 10.1038/nchem.1728 From NLM.
(169) Yip, K. M.; Fischer, N.; Paknia, E.; Chari, A.; Stark, H. Atomic-resolution protein structure determination by cryo-EM. *Nature* **2020**, *587* (7832), 157-161. DOI: 10.1038/s41586-020-2833-4 From NLM.

(170) Dubochet, J.; Adrian, M.; Chang, J. J.; Homo, J. C.; Lepault, J.; McDowall, A. W.; Schultz, P. Cryo-electron microscopy of vitrified specimens. *Q Rev Biophys* **1988**, *21* (2), 129-228. DOI: 10.1017/s0033583500004297 From NLM.
(171) HANSZEN, K.-J. The optical transfer theory of the electron microscope: fundamental, principles and applications. *Advanced Optical and Electron Microscopy* **1971**, *4*, 1.
(172) Knapek, E.; Dubochet, J. Beam damage to organic material is considerably reduced in cryo-electron microscopy. *Journal of molecular biology* **1980**, *141* (2), 147-161.
(173) Orlova, E.; Saibil, H. R. Structural analysis of macromolecular assemblies by electron microscopy. *Chemical reviews* **2011**, *111* (12), 7710-7748.
(174) Harris, J. R. *Negative staining and cryoelectron microscopy: the thin film techniques*; Garland Science, 2023.
(175) Hart, R. Improved negative stain electron microscopy procedure for detecting surface detail on high density lipoproteins. *Microscopy Today* **2020**, *28* (5), 54-58.
(176) Dobro, M. J.; Melanson, L. A.; Jensen, G. J.; McDowall, A. W. Plunge freezing for electron cryomicroscopy. *Methods in enzymology* **2010**, *481*, 63-82.
(177) Saibil, H. R. Macromolecular structure determination by cryo-electron microscopy. *Acta Crystallographica Section D: Biological Crystallography* **2000**, *56* (10), 1215-1222.
(178) D'Imprima, E.; Kühlbrandt, W. Current limitations to high-resolution structure determination by single-particle cryoEM. *Quarterly reviews of biophysics* **2021**, *54*, e4.
(179) Jumper, J.; Evans, R.; Pritzel, A.; Green, T.; Figurnov, M.; Ronneberger, O.; Tunyasuvunakool, K.; Bates, R.; Žídek, A.; Potapenko, A. Highly accurate protein structure prediction with AlphaFold. *Nature* **2021**, *596* (7873), 583-589.
(180) Varadi, M.; Anyango, S.; Deshpande, M.; Nair, S.; Natassia, C.; Yordanova, G.; Yuan, D.; Stroe, O.; Wood, G.; Laydon, A. AlphaFold Protein Structure Database: massively expanding the structural coverage of protein-sequence space with high-accuracy models. *Nucleic acids research* **2022**, *50* (D1), D439-D444.
(181) Schrödinger, E. An undulatory theory of the mechanics of atoms and molecules. *Uspekhi Fizicheskikh Nauk* **1927**, *7* (3), 176-201.
(182) Yang, Z.; Zeng, X.; Zhao, Y.; Chen, R. AlphaFold2 and its applications in the fields of biology and medicine. *Signal Transduction and Targeted Therapy* **2023**, *8* (1), 115.
(183) Evans, R.; O'Neill, M.; Pritzel, A.; Antropova, N.; Senior, A.; Green, T.; Žídek, A.; Bates, R.; Blackwell, S.; Yim, J. Protein complex prediction with AlphaFold-Multimer. *biorxiv* **2021**, 2021.2010. 2004.463034.

(184) Abramson, J.; Adler, J.; Dunger, J.; Evans, R.; Green, T.; Pritzel, A.; Ronneberger, O.; Willmore, L.; Ballard, A. J.; Bambrick, J. Accurate structure prediction of biomolecular interactions with AlphaFold 3. *Nature* **2024**, 1-3.
(185) Brilot, A. F.; Agard, D. A. The atomic structure of the microtubule-nucleating γ-tubulin small complex and its implications for regulation. *bioRxiv* **2018**, 310813.
(186) Consolati, T.; Locke, J.; Roostalu, J.; Chen, Z. A.; Gannon, J.; Asthana, J.; Lim, W. M.; Martino, F.; Cvetkovic, M. A.; Rappsilber, J. Microtubule nucleation properties of single human γTuRCs explained by their cryo-EM structure. *Developmental cell* **2020**, *53* (5), 603-617. e608.
(187) Janski, N.; Masoud, K.; Batzenschlager, M.; Herzog, E.; Evrard, J.-L.; Houlne, G.; Bourge, M.; Chaboute, M.-E.; Schmit, A.-C. The GCP3-interacting proteins GIP1 and GIP2 are required for γ-tubulin complex protein localization, spindle integrity, and chromosomal stability. *The Plant Cell* **2012**, *24* (3), 1171-1187.
(188) Punjani, A.; Rubinstein, J. L.; Fleet, D. J.; Brubaker, M. A. cryoSPARC: algorithms for rapid unsupervised cryo-EM structure determination. *Nature methods* **2017**, *14* (3), 290-296.
(189) Xu, Y.; Munoz-Hernandez, H.; Krutyholowa, R.; Marxer, F.; Cetin, F.; Wieczorek, M. Closure of the gamma-tubulin ring complex by CDK5RAP2 activates microtubule nucleation. *bioRxiv* **2023**, 2023.2012. 2014.571518.
(190) Zivanov, J.; Nakane, T.; Forsberg, B. O.; Kimanius, D.; Hagen, W. J.; Lindahl, E.; Scheres, S. H. New tools for automated high-resolution cryo-EM structure determination in RELION-3. *elife* **2018**, *7*, e42166.
(191) Bepler, T.; Morin, A.; Rapp, M.; Brasch, J.; Shapiro, L.; Noble, A. J.; Berger, B. Positive-unlabeled convolutional neural networks for particle picking in cryo-electron micrographs. *Nature methods* **2019**, *16* (11), 1153-1160.
(192) Von Loeffelholz, O.; Venables, N. A.; Drummond, D. R.; Katsuki, M.; Cross, R.; Moores, C. A. Nucleotide–and Mal3-dependent changes in fission yeast microtubules suggest a structural plasticity view of dynamics. *Nature communications* **2017**, *8* (1), 2110.
(193) Alva, V. Protein Sequence Analysis Using the MPI Bioinformatics Toolkit. **2022**.
(194) Gabler, F.; Nam, S. Z.; Till, S.; Mirdita, M.; Steinegger, M.; Söding, J.; Lupas, A. N.; Alva, V. Protein sequence analysis using the MPI bioinformatics toolkit. *Current Protocols in Bioinformatics* **2020**, *72* (1), e108.
(195) Caydasi, A. K.; Pereira, G. SPOC alert—when chromosomes get the wrong direction. *Experimental cell research* **2012**, *318* (12), 1421-1427.

(196) Choy, R. M.; Kollman, J. M.; Zelter, A.; Davis, T. N.; Agard, D. A. Localization and orientation of the γ-tubulin small complex components using protein tags as labels for single particle EM. *Journal of structural biology* **2009**, *168* (3), 571-574.
(197) Fong, K. K.; Zelter, A.; Graczyk, B.; Hoyt, J. M.; Riffle, M.; Johnson, R.; MacCoss, M. J.; Davis, T. N. Novel phosphorylation states of the yeast spindle pole body. *Biology open* **2018**, *7* (10), bio033647.
(198) Jones, M. H.; Keck, J. M.; Wong, C. C.; Xu, T.; Yates, J. R.; Winey, M. Cell cycle phosphorylation of mitotic exit network (MEN) proteins. *Cell Cycle* **2011**, *10* (20), 3435-3440.
(199) Lin, T.-c.; Gombos, L.; Neuner, A.; Sebastian, D.; Olsen, J. V.; Hrle, A.; Benda, C.; Schiebel, E. Phosphorylation of the yeast γ-tubulin Tub4 regulates microtubule function. *PloS one* **2011**, *6* (5), e19700.
(200) Peng, Y.; Moritz, M.; Han, X.; Giddings, T. H.; Lyon, A.; Kollman, J.; Winey, M.; Yates III, J.; Agard, D. A.; Drubin, D. G. Interaction of CK1δ with γTuSC ensures proper microtubule assembly and spindle positioning. *Molecular biology of the cell* **2015**, *26* (13), 2505-2518.
(201) Rai, D.; Song, Y.; Hua, S.; Stecker, K.; Monster, J. L.; Yin, V.; Stucchi, R.; Xu, Y.; Zhang, Y.; Chen, F. CAMSAPs and nucleation-promoting factors control microtubule release from γ-TuRC. *Nature Cell Biology* **2024**, 1-17.
(202) Roostalu, J.; Cade, N. I.; Surrey, T. Complementary activities of TPX2 and chTOG constitute an efficient importin-regulated microtubule nucleation module. *Nature cell biology* **2015**, *17* (11), 1422-1434.
(203) Huang, T.-L.; Wang, H.-J.; Chang, Y.-C.; Wang, S.-W.; Hsia, K.-C. Promiscuous binding of microprotein Mozart1 to γ-tubulin complex mediates specific subcellular targeting to control microtubule array formation. *Cell Reports* **2020**, *31* (13).
(204) Leong, S. L.; Lynch, E. M.; Zou, J.; Tay, Y. D.; Borek, W. E.; Le Cornu, J. D.; Tuijtel, M. W.; Rappsilber, J.; Sawin, K. E. Reconstitution of microtubule nucleation in vitro reveals novel roles for Mzt1. *Current Biology* **2019**, *29* (13), 2199-2207. e2110.
(205) Chen, F.; Tillberg, P. W.; Boyden, E. S. Expansion microscopy. *Science* **2015**, *347* (6221), 543-548.
(206) Lučić, V.; Förster, F.; Baumeister, W. Structural studies by electron tomography: from cells to molecules. *Annu. Rev. Biochem.* **2005**, *74* (1), 833-865.
(207) Dendooven, T.; Yatskevich, S.; Burt, A.; Chen, Z. A.; Bellini, D.; Rappsilber, J.; Kilmartin, J. V.; Barford, D. Structure of the native γ-tubulin ring complex capping spindle microtubules. *Nat Struct Mol Biol* **2024**. DOI: 10.1038/s41594-024-01281-y From NLM.

(208) Tanaka, K.; Mukae, N.; Dewar, H.; Van Breugel, M.; James, E. K.; Prescott, A. R.; Antony, C.; Tanaka, T. U. Molecular mechanisms of kinetochore capture by spindle microtubules. *Nature* **2005**, *434* (7036), 987-994.
(209) Zahm, J. A.; Stewart, M. G.; Carrier, J. S.; Harrison, S. C.; Miller, M. P. Structural basis of Stu2 recruitment to yeast kinetochores. *Elife* **2021**, *10*, e65389.
(210) Goh, P.-Y.; Kilmartin, J. V. NDC10: a gene involved in chromosome segregation in Saccharomyces cerevisiae. *The Journal of cell biology* **1993**, *121* (3), 503-512.
(211) Nakamura, M.; Yagi, N.; Kato, T.; Fujita, S.; Kawashima, N.; Ehrhardt, D. W.; Hashimoto, T. Arabidopsis GCP3-interacting protein 1/MOZART 1 is an integral component of the γ-tubulin-containing microtubule nucleating complex. *The Plant Journal* **2012**, *71* (2), 216-225.
(212) Dhani, D. K.; Goult, B. T.; George, G. M.; Rogerson, D. T.; Bitton, D. A.; Miller, C. J.; Schwabe, J. W.; Tanaka, K. Mzt1/Tam4, a fission yeast MOZART1 homologue, is an essential component of the γ-tubulin complex and directly interacts with GCP3Alp6. *Molecular biology of the cell* **2013**, *24* (21), 3337-3349.
(213) Wurtz, M.; Bohler, A.; Neuner, A.; Zupa, E.; Rohland, L.; Liu, P.; Vermeulen, B. J. A.; Pfeffer, S.; Eustermann, S.; Schiebel, E. Reconstitution of the recombinant human gamma-tubulin ring complex. *Open Biol* **2021**, *11* (2), 200325. DOI: 10.1098/rsob.200325.
(214) Chang, A. Y.; Chau, V.; Landas, J. A.; Pang, Y. Preparation of calcium competent Escherichia coli and heat-shock transformation. *JEMI methods* **2017**, *1* (22-25).
(215) Zhang, K. Gctf: Real-time CTF determination and correction. *Journal of structural biology* **2016**, *193* (1), 1-12.
(216) Zheng, S. Q.; Palovcak, E.; Armache, J.-P.; Verba, K. A.; Cheng, Y.; Agard, D. A. MotionCor2: anisotropic correction of beam-induced motion for improved cryo-electron microscopy. *Nature methods* **2017**, *14* (4), 331-332.
(217) Asarnow, D.; Palovcak, E.; Cheng, Y. UCSF pyem v0. 5. *Zenodo https://doi. org/10.5281/zenodo* **2019**, *3576630*, 2019.
(218) Zivanov, J.; Nakane, T.; Scheres, S. H. A Bayesian approach to beam-induced motion correction in cryo-EM single-particle analysis. *IUCrJ* **2019**, *6* (1), 5-17.
(219) Zivanov, J.; Nakane, T.; Scheres, S. H. Estimation of high-order aberrations and anisotropic magnification from cryo-EM data sets in RELION-3.1. *IUCrJ* **2020**, *7* (2), 253-267.
(220) Nakane, T.; Kimanius, D.; Lindahl, E.; Scheres, S. H. Characterisation of molecular motions in cryo-EM single-particle data by multi-body refinement in RELION. *elife* **2018**, *7*, e36861.

(221) Emsley, P.; Lohkamp, B.; Scott, W. G.; Cowtan, K. Features and development of Coot. *Acta Crystallographica Section D: Biological Crystallography* **2010**, *66* (4), 486-501.
(222) Liebschner, D.; Afonine, P. V.; Baker, M. L.; Bunkóczi, G.; Chen, V. B.; Croll, T. I.; Hintze, B.; Hung, L.-W.; Jain, S.; McCoy, A. J. Macromolecular structure determination using X-rays, neutrons and electrons: recent developments in Phenix. *Acta Crystallographica Section D: Structural Biology* **2019**, *75* (10), 861-877.
(223) Croll, T. I. ISOLDE: a physically realistic environment for model building into low-resolution electron-density maps. *Acta Crystallographica Section D: Structural Biology* **2018**, *74* (6), 519-530.
(224) Jamali, K.; Käll, L.; Zhang, R.; Brown, A.; Kimanius, D.; Scheres, S. H. Automated model building and protein identification in cryo-EM maps. *Nature* **2024**, 1-2.
(225) UniProt: the universal protein knowledgebase in 2023. *Nucleic acids research* **2023**, *51* (D1), D523-D531.
(226) Pettersen, E. F.; Goddard, T. D.; Huang, C. C.; Couch, G. S.; Greenblatt, D. M.; Meng, E. C.; Ferrin, T. E. UCSF Chimera—a visualization system for exploratory research and analysis. *Journal of computational chemistry* **2004**, *25* (13), 1605-1612.
(227) Mirdita, M.; Schütze, K.; Moriwaki, Y.; Heo, L.; Ovchinnikov, S.; Steinegger, M. ColabFold: making protein folding accessible to all. *Nature methods* **2022**, *19* (6), 679-682.
(228) Abràmoff, M. D.; Magalhães, P. J.; Ram, S. J. Image processing with ImageJ. *Biophotonics international* **2004**, *11* (7), 36-42.

Publications

Zupa, E.*; Zheng, A.*; Neuner, A.; Würtz, M.; Liu, P.; Böhler, A.; Schiebel, E.; Pfeffer, S. The cryo-EM structure of a γ-TuSC elucidates architecture and regulation of minimal microtubule nucleation systems. Nature Communications 2020, 11 (1), 5705.

Gao, Q.; Vermeulen, B. J. A.; Würtz, M.; Shin, H.; Erdogdu, D.; Zheng, A.; Hofer, F. W.; Neuner, A.; Pfeffer, S.; Schiebel, E. The structure of the γ-TuRC at the microtubule minus end - not just one solution. Bioessays 2024, e2400117. DOI: 10.1002/bies.202400117

In revision

Anjun Zheng*, Bram J.A. Vermeulen*, Annett Neuner, Martin Würtz *et al*. Structural insights into the interplay between microtubule polymerases, γ-tubulin complexes and their receptors.

* Contributed equally

Acknowledgments

Dear Prof. Dr. Schiebel, thanks for the opportunity you provided with to do the PhD in the cell biology field in your lab, which is much different from the content I had been working on during my master period. During my PhD time in your lab, my knowledge of the cell biology field especially in the microtubule, cell cytoskeleton, and cell cycle has been expanded and enlarged, which I believed was your professional guide and the strictly scientific attitudes. Moreover, I would also like to thank you for your time and professional comments, for always keeping the door open to discuss, for foreseeing the potential in experimental design, and for providing support during hard times.

I would also like to sincerely thank my TAC and defense committee members Prof. Gislene Pereira and Dr. Stefan Pfeffer for their valuable and helpful advice, thus, I always feel supported during the progress of the project conduction.

I want also greatly thank the Schiebel lab members for their help with the experimental part. Thanks to Dr. Diana Rüthnick, Dr. Jlenia Vitale, and Dr. Azqa Khan for always being friendly and helpful when I inquired about the experiments. Thanks to Dr. Martin Würtz for giving helpful suggestions concerning the experiment, and always warm-hearted for helping to contact the instrument platform out of campus. I would also like to thank Dr. Stefan Pfeffer, Dr. Erik Zupa, and Bram Vermeulen for providing support in the aspect of structural analysis. I would especially like to thank Dr. Annett Neuner who has always been supportive concerning the negative stain EM and I will always remember the time we worked together. Besides, I would also like to thank our technician Ursula Jäkle, who is always full of energy and provides all kinds of support for us: the machine fixation, the material order, the experimental item arrangement, and you could always rely on her because she can manage everything in order in the lab. I would also like to thank all the rest lab members named out or not, without any of you, there would not be such a friendly, positive, and international group here.

Looking back to the last few years, I have unfortunately experienced the COVID-19 epidemics, lab transferring, and several times of infections with the COVIDs, which I have

never thought about before. Even though all different surprising situations happened to me one by one and put me in several difficult times, I always tried to be positive. Last but not least, all these experiences I have been through made wonderful memories of my life and I believe the adventure of nature and life is not always smooth, thus, learning to adapt and enjoy the journey not only for the destination will be the ongoing lesson I have learned during the course of being a ‘Dr.’.